Spin-dependent hot electron transport and nanoscale magnetic imaging of metal/Si structures

Andreas Kaidatzis

THÈSE de DOCTORAT
de l'UNIVERSITÉ PARIS SUD (PARIS XI)

Specialité :

Physique du Solide

présentée par :

Andreas Kaidatzis

pour obtenir le titre de :

DOCTEUR DE L'UNIVERSITÉ PARIS XI

Spin-dependent hot electron transport and nanoscale magnetic imaging of metal/Si structures

soutenue le 28 Octobre 2008 devant le jury composé de :

M.	**Bernard**	**Dieny**	**Président**
M.	**Ron**	**Jansen**	**Rapporteur**
M.	**Bertrand**	**Kierren**	**Rapporteur**
M.	**Yves**	**Lassailly**	**Examinateur**
M.	**Dimitrios**	**Niarchos**	**Examinateur**
M.	**Stanislas**	**Rohart**	**Invité**
M.	**André**	**Thiaville**	**Directeur de thèse**

Contents

Chapter 1

Introduction

Traditional semiconductor electronics are based on the electron or hole mass and charge. The pioneering work of Albert Fert [*Baibich et al.*, 1988] and Peter Grünberg [*Grünberg et al.*, 1986] (joint Nobel prize in Physics, 2007), resulted in the discovery of the giant magnetoresistance (GMR) effect and the introduction of the electron spin as a new degree of freedom. The spin is an intrinsic property of an electron and can be either up or down. Within only a few years, technological applications of the GMR effect were found, and commercially used in the magnetic information storage industry. The era of magnetoelectronics [*Prinz*, 1998] or spintronics [*Wolf et al.*, 2000] had emerged. In the following years, spintronic devices appeared using electrons with energies high above the Fermi level (hot electrons), like the spin-valve transistor [*Monsma et al.*, 1995] and the magnetic tunnel transistor [*Mizushima et al.*, 1998]. These devices are relying for their operation on hot electrons transmitted sometimes even ballistically (i.e. without any scattering) through magnetic multilayers. This created the need for locally probing the hot electron spin-dependent transport.

In parallel and in connection with the development of spintronics, the need for ever increasing storage capability, has lead to extended research on magnetic systems with reduced dimensions. The analysis and characterization for high-density magnetic data storage devices, implies the capability of imaging magnetic structures, or the stray field that they produce, down to the nanometer scale. Considering the fact that the bit length in actual magnetic hard-disk drives is not longer than some 10 nm, the development of high spatial resolution magnetic imaging techniques for characterization of data storage media and read heads, is necessary. Since the 90s, significant advancements occurred in the field of magnetic microscopy [*Freeman and Choi*, 2001; *Hopster and Oepen*, 2005]. Magnetic imaging techniques with a spatial resolution of some 10 nm (Magnetic Transmission X-ray Microscopy, for a review book, see [*Beaurepaire et al.*, 2006], Magnetic Force Microscopy, for a review, see (MFM) [*Thiaville et al.*, 2005]) or even down to the atomic scale (Spin-Polarized Scanning Tunneling Microscopy [*Bode*, 2003]) have appeared. Among them, Ballistic Electron Emission Microscopy (BEEM) [*Kaiser and Bell*, 1988; *Rippard and Buhrman*, 1999], relying on hot electron transport has also been developed and, although this has not been proved

yet, should allow magnetic imaging with a resolution below 10 nm.

This thesis is dealing with local hot electron spin-dependent transport studies and imaging of nanometer-scale magnetic structures in spin-valves, using BEEM. The technique did its debut at the end of the 80s as a method for local hot electron transport studies on metal/semiconductor structures [*Prietsch*, 1995]. In the following years, it developed to a versatile tool which, among others, is used for local spin-dependent transport studies [*Rippard and Buhrman*, 2000] and magnetic imaging with spatial resolution on the nm scale [*Rippard and Buhrman*, 1999]. The main objective of this thesis was to develop a BEEM experiment for high resolution magnetic imaging. Although our research group has extended experience in magnetic imaging using MFM, a higher magnetic resolution was anticipated for BEEM experiments, which lead to starting the work on this project.

The manuscript is organized in the following manner:

Chapter 2: First, the fundamentals of hot electron transport are discussed. The definition of hot electrons is given. The main methods for hot electron creation and detection and the main mechanisms of energy loss during transport in solids, are discussed. An overview of hot electron experiments is given next. The basic physical principles of BEEM experiments are presented, along with the particularities of the technique. The BEEM spectroscopy and imaging operation modes are discussed. Next, the effect of the electron spin on hot electron transport, is introduced. The initial spin-dependent hot electron transport experiments are presented and a simple model is discussed. Lastly, the ability to perform magnetic imaging by incorporating the spin degree of freedom in BEEM experiments, is presented.

Chapter 3: In this chapter, the instrumentation used during this thesis is presented. The vacuum physical vapor deposition systems are described first, followed by the STM-BEEM microscope. The standard structural, electric and magnetic characterization techniques used in this thesis are discussed next.

Chapter 4: The first half of the experimental work undertaken during this thesis concerned the development of a BEEM sample fabrication method, and it is presented in this chapter. The sample fabrication requirements and the sample design that fulfills them, are first discussed. Next, the preparation and characterization of the substrates used is presented. The fabrication and characterization of the essential Au/Si Schottky barrier used for BEEM experiments is discussed. The fabrication of the multilayer stacks is finally discussed, along with their structural and magnetic characterization.

The scientific results of this work are presented in chapters 5 and 6.

Chapter 5: Initially, BEEM studies have been performed on nonmagnetic multilayer/Si structures. As those layers are as well present in the magnetic multilayer samples, it was necessary to characterize them before advancing to magnetic sample measurements. The Au/Si and Cu/Si Schottky interfaces are studied first. Hot electron transport through Au/Cu/Au/Si structures has been studied, in order to determine the effect of the Au/Cu interface on hot electron scattering. Preliminary BEEM experiments on samples containing Co and Permalloy in submonolayer coverages, are finally discussed.

Chapter 6: The main scientific results of this thesis are presented in this chapter. In the first part, spin-dependent hot electron transport in Co and Permalloy layers is discussed. After introducing some analytical expressions describing hot electron transmission through single magnetic layers and spin-valve-type trilayers, the experimental results are analyzed. Hot electron transmission measurements have been performed on multilayer samples containing single magnetic layers or spin-valves. By using the analytical expressions introduced before, the spin-dependent hot electron attenuation lengths in Co and Permalloy are deduced as a function of electron energy in the range 1-2 eV above the Fermi level. In the second part, imaging of magnetic structures is discussed. We focus on imaging of 360° domain walls in ultra-thin Co layers. The effect of the applied field magnitude and direction on the domain wall structure is discussed. The domain wall width is found to decrease as the applied field increases. Moreover, the domain wall profile becomes asymmetric for an applied field direction non-collinear to the domain wall axis. The experimental results are compared to micromagnetic calculations, and an excellent agreement is found. This allows us to discuss the BEEM magnetic resolution, and it is shown that it is better than 50 nm.

Chapter 2

Introduction to ballistic electron microscopies

2.1 Introduction

In this chapter, the main concepts of hot electron transport and ballistic electron microscopy are presented. The research of "high energy" (hot) electron transport in solids was initiated during the 60's, both experimentally [*Mead*, 1961] and theoretically [*Quinn*, 1962]. Soon after, the first spin-dependent hot electron transport studies in ferromagnetic metals were performed [*Hofmann et al.*, 1967; *Busch et al.*, 1969]. In the following years, various studies have been performed, concerning the macroscopic measurement of hot electron transmission through solids.

Local studies became possible during the 80's, because of the technological advancement in data acquisition and processing, and mainly because of the development of a radically novel instrument, the Scanning Tunneling Microscope (STM) [*Binnig et al.*, 1982]. STM lead to the merging of hot electron transport studies and microscopy studies with the development of a new STM-based technique, Ballistic Electron Emission Microscopy (BEEM) [*Kaiser and Bell*, 1988]. In the following, magnetic imaging was achieved using BEEM, by locally mapping the spin-dependent transport in spin-valves [*Rippard and Buhrman*, 1999].

2.2 Hot and ballistic electrons

2.2.1 Definitions

The electrons participating to the electrical conductivity of solids are the *free electrons*, with energies a few k_BT ($\approx$26 meV at 300 K) above or below the Fermi level (*thermal* energies) [*Kittel*, 1976]. Electrons with energies higher than a few tenths of an eV above the Fermi level, are called *"hot" electrons*, by analogy to the effect of temperature that can excite electrons to higher energy levels. However, those energies are not accessible

to solid state matter simply by increasing the temperature, since the excitation of electrons to 1 eV above the Fermi level would necessitate a temperature rise up to ≈11000 K! In this work we focus on hot electron transport through metallic multilayers, for energies in the range 1 to 2 eV above the Fermi level.

In contrast to the thermal electrons where the inferior energy levels are filled, hot electrons lie above empty energy levels, which means that during transport they may loose energy and thermalize. Besides inelastic scattering where electrons suffer energy loss and momentum change, elastic scattering also occurs causing only momentum change. For the electron energy range of interest, electron-electron inelastic scattering is the main source of energy loss during electron transport, while the energies are too low for plasmon excitations [*Crowell and Sze*, 1967]. Electron-phonon scattering is considered a quasi-elastic process, since hot electrons can suffer only an energy loss on the order of k_BT, which is not significant compared to the initial electron energy. Electron-defect and electron-impurity scattering are always present and introduce a temperature and energy independent elastic scattering contributions [*Crowell and Sze*, 1967]. If during the transport process the hot electrons stay unscattered, they are called *ballistic electrons*.

2.2.2 Hot electron creation and detection

As it is not experimentally possible to thermally excite electrons to energies a few eV above the Fermi level, other means of hot electron creation should be found. The two main excitation methods are photoemission and tunnel emission. In the first case hot electrons are created in the volume of the solid by transfer of the photon energy to thermal electrons exciting them to higher energy levels. In the second case hot electrons are field emitted through a tunnel barrier into the solid, thus in this case we have actually hot electron *injection*. For hot electron detection a potential barrier is used as an *energy filter* ruling out thermal electrons.

The first studies of hot electron transport through thin metal films were performed using the tunnel emission technique [*Mead*, 1962]. In those experiments, electrons are caused to tunnel from a metal substrate through a thin insulating layer (beryllium oxide) into a thin metal electrode, through which a certain number pass into vacuum where they are collected (figure 2.1a). In this case, the metal/vacuum interface poses a potential barrier equal to the metal work function. Since metal work functions are in the range 4-5 eV, only hot electrons with higher energies can be collected. However, the capability of variating the tunnel bias and injecting hot electrons at various energies, allows for spectroscopic studies.

Low energy hot electron transport studies were made possible by the overlayer technique [*Crowell et al.*, 1962]. In this case, metal films evaporated on a semiconductor are used (figure 2.1b). A potential step is formed at the metal/semiconductor contact (*Schottky contact*). Photoemitted electrons in the metal film are energy filtered at the Schottky contact and collected at the semiconductor. The measurement of the photoelectric yield as a function of photon energy and metal film thickness gives the

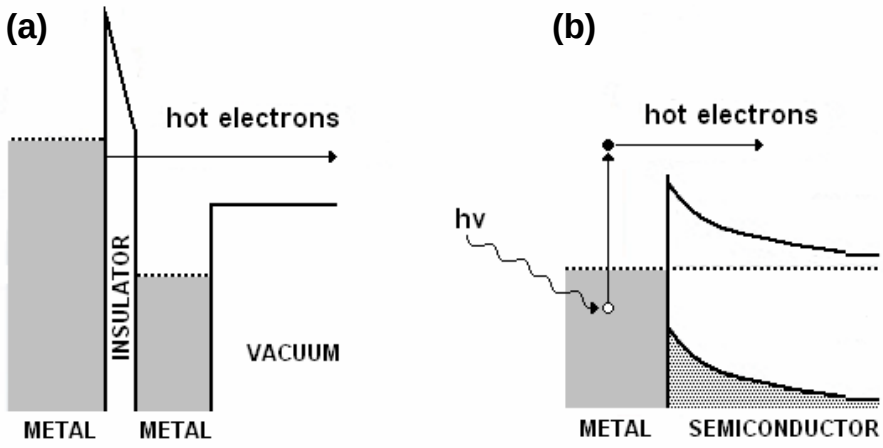

Figure 2.1: Schematic energy diagrams of the first hot electron transport experiments. Tunnel emission (a) and photoemission (b) of hot electrons.

value of the hot electron mean-free path, as well as the height of the potential barrier at the Schottky contact. The potential barrier at the Schottky contact is of the order of some tenths of an eV [*Sze*, 1981], allowing the collection of low energy hot electrons. However, spectroscopic studies in this case are less easy, since various illumination sources should be used in order to variate the hot electron energy.

2.2.3 Hot-electron devices

The ability of performing spectroscopic studies using the tunnel emission technique, and the ability of collecting low energy hot electrons using the overlayer technique, can be combined in a single experiment. An all-solid-state structure can be fabricated for ballistic electron creation and detection, by utilizing a three-terminal transistor-like sample configuration (see for example figure 2.2). In these three terminal devices, electrons are injected by an emitter electrode through a tunnel or a Schottky potential barrier into a thin base electrode. The base electrode has to be separated from the subsequent collector electrode by a similar potential barrier which acts as an energy filter. If the electron injection energy is higher than the base/collector potential barrier height and the base is thin enough so that a fraction of the injected electrons can cross it without suffering any scattering (*ballistically*), then those ballistic electrons are eligible to overcome the base/collector potential barrier. In this case they can be transported into the collector. A sample with design of this type is usually called a *hot electron device*.

A hot electron device incorporating three metal layers separated by two tunnel junctions in a triode configuration, was first demonstrated during the early 60s [*Mead*, 1961]. Here, an all-semiconductor heterostructure hot electron device developed during the early 80s, named Tunneling Hot Electron Transfer Amplifier (THETA) [*Heiblum*

et al., 1985], is discussed.

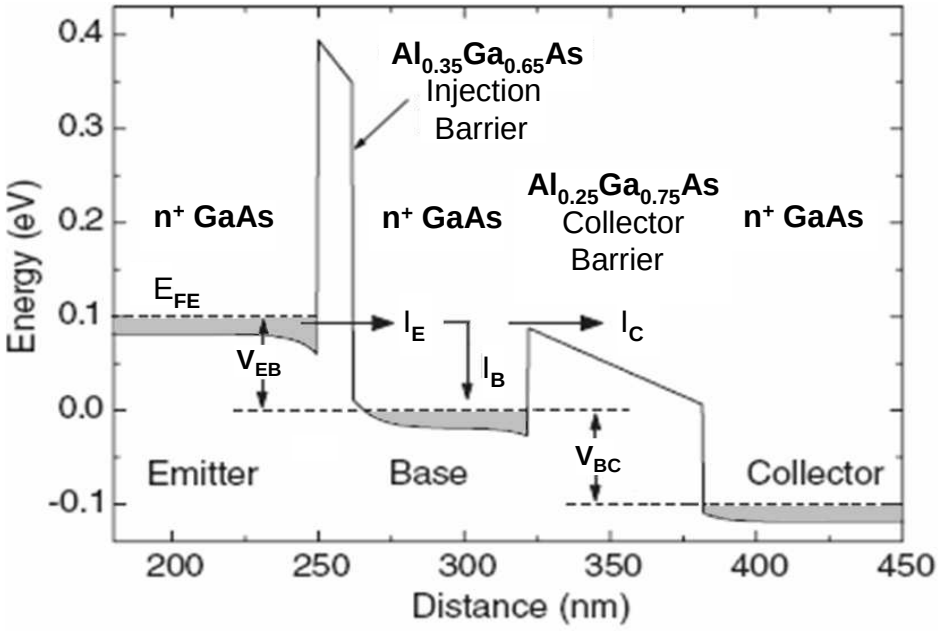

Figure 2.2: Conduction band profile of a typical THETA device under forward bias [*Heiblum et al.*, 1985]. Image adapted from [*Smoliner et al.*, 2004].

In figure 2.2 the conduction band profile of a THETA device under forward bias is shown. Between the emitter and the base, a thin layer of a wide-gap material acts as a tunneling barrier. By applying a negative emitter voltage (V_{EB}), electrons are injected into the base region of the device to form a ballistic electron beam. The composition of the base-collector potential barrier provides a lower barrier height, while it is thick enough to prevent thermal electrons from flowing into the collector. While traversing the base region the injected electrons undergo different transport mechanisms. Electrons which have been scattered elastically or have suffered minor energy losses, may contribute as quasi-ballistic electrons to the collector current, along with the purely ballistic ones. Depending on the collector-base bias V_{BC} and the emitter-base bias V_{EB}, electrons either reach the collector contact or are filtered by the collector barrier and relax down to the base contact. By analyzing the hot electron energy distribution, it is possible to study ballistic and quasi-ballistic electron transport in the base region of the device. Inelastically scattered electrons with insufficient energy to surpass the base-collector potential barrier, are collected at the base terminal. The collector current corresponds to as much as 70 % of the injected current at 4.2 K. However, when the device is operated at room temperature, thermally activated currents are dominant due to the low filtering barrier, and overwhelm the tunneling currents [*Heiblum and Fischetti*, 1990].

2.3 Ballistic Electron Emission Microscopy (BEEM)

The experiments described above concern macroscopic hot electron transport studies. Microscopic (local) hot electron transport studies can be performed using Ballistic Electron Emission Microscopy (BEEM), a technique developed by Kaiser and Bell [*Kaiser and Bell*, 1988]. BEEM is a three terminal modification of Scanning Tunneling Microscopy (STM), where the STM tunnel barrier is used as a hot electron injector and a metal/semiconductor interface is used for hot electron collection. BEEM provides the ability to investigate hot electron transport through thin films and buried interfaces in the energy range from a few tenths of an eV up to a few eV above the Fermi level. Both microscopy and spectroscopy modes are possible, with typical spatial resolution down to the nanometer scale, and energy resolution 100 meV at room temperature. Although initial studies were limited to metal/semiconductor interfaces [*Prietsch*, 1995], they were later extended to metal/insulator/semiconductor structures [*Ludeke et al.*, 1995], buried semiconductor heterostructures [*Narayanamurti and Kozhevnikov*, 2001], organic thin films [*Ozcan et al.*, 2007], individual molecules [*Bannani et al.*, 2007] and spin-valve structures [*Rippard and Buhrman*, 1999], a case that will be treated in more detail later. In this section we shall briefly discuss some basic BEEM concepts.

2.3.1 From Scanning Tunneling Microscopy to BEEM

Scanning Tunneling Microscopy

The landmark development of STM during the early 80s [*Binnig et al.*, 1982] revolutionized nanoscience research. The underlying physical basis of the STM is electron tunneling. Electron tunneling occurs between two conductors separated by a thin insulating layer, the tunneling potential barrier. Electron tunneling in STM occurs between the (usually) metallic tip and the conducting sample surface, while the tunneling barrier is provided by vacuum, gas, or liquid. A set of piezoelectric ceramic elements is used to controllably approach the STM tip some Å from the sample surface, and scan or position it at will. Basic to the operation of the STM, is the exponential dependence of the tunneling current, I_T, to the tunneling barrier width, d, ($I_T \propto \exp(-\sqrt{\phi}d)$), where ϕ is the local work function (in eV for d in Å), which is equal to the barrier height [*Binnig et al.*, 1982]. With barrier heights of a few eVs, a change of the tunneling barrier width by 1 Å, changes the tunnel current one order of magnitude. Typical values are 1 nA tunneling current for a 1 V tunneling gap voltage (V_T). Because one electrode is formed into the shape of a tip, the tunneling current is confined to a narrow path between the apex of the tip and the surface under investigation. In the case of a single atom at the apex, the effective diameter of this narrow path can decrease to a magnitude of atomic dimension, giving rise to the excellent resolution of the STM.

For STM imaging measurements, several successive line scans over the surface are synthesized to produce a topographic image. There are two operation modes for imaging: (i) The constant current mode, where the z-position of the tip is controlled by means of a feedback loop, in order to keep tunneling current constant by modulating

the width of the tunneling barrier. (ii) The constant height mode, where the STM tip is scanned in constant height over the sample with the feedback loop disabled, while measuring the variations in tunneling current. For Scanning Tunneling Spectroscopy (STS) measurements, the tip is kept stationary at a specified point over the sample surface. With the feedback loop disabled, the tunneling current is measured while sweeping the tunneling voltage. For high resolution imaging and stable spectroscopy measurements, sufficient mechanical vibration isolation should be present. In addition, thermal-drift velocities have to be as small as possible in order to allow enough time for the acquisition of a spectrum at a fixed tip position.

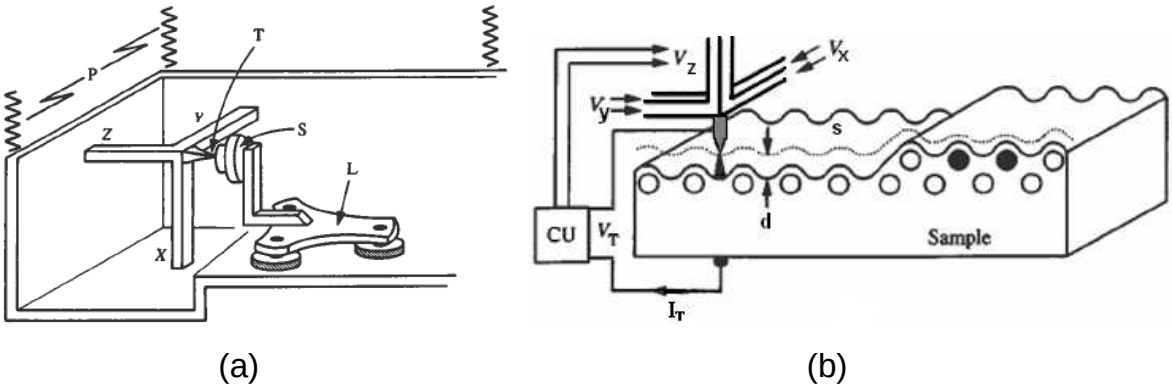

Figure 2.3: Schematic of one of the first scanning tunneling microscopes (STM) and its operation. Taken from [*Binnig and Rohrer*, 1986]

An STM which uses a piezoelectric tripod for fine-positioning of the tip is depicted in figure 2.3. The tip T of the microscope shown in figure 2.3a, is scanned over the surface of a sample S with a piezoelectric tripod (X, Y, Z). The rough positioner L brings the sample within reach of the tripod. A vibration filter system P protects the instrument from external vibrations. In the constant tunneling current mode of operation, a voltage V_z is applied to the Z piezoelectric element by means of the control unit CU shown in figure 2.3b. In order to keep the tunneling current constant while the tip is scanned across the surface, the tip-surface separation d is altered, by variating V_x and V_y. The movement of the tip generally follows the surface topography. Electronic inhomogeneities also produce structure in the tip trace, as illustrated on the right above two surface atoms having excess negative charge. It should be noted that our instrument follows the same design (see section 3.2.2).

Ballistic Electron Emission Microscopy

BEEM is the extension of STM to metal/semiconductor structures, where a three terminal setup is implemented, similar to the one of the THETA device (figure 2.2). The STM metal tip (emitter) injects electrons across the tunneling gap into a thin metal film (base) deposited on a semiconductor (collector). A Schottky contact is

formed at the metal/semiconductor interface. The metal film and the semiconductor are contacted separately. The tunnel voltage V_T is applied between the STM tip and the metal surface of the sample. A fraction of the injected electrons reach ballistically the metal/semiconductor interface. These electrons may cross the interface if their energy is higher than the potential step at the Schottky contact (*Schottky barrier height* Φ_B)[1]. In this case, they are collected by the semiconductor terminal and contribute to the collector or *BEEM current* I_B (figure 2.4). The tunnel current I_T is kept constant by the STM feedback loop while measuring I_B. For noble metal films with layer thickness ≈ 10 nm and for injected current of 1 nA and 1 eV above the Fermi level, the BEEM signal is a few 10 pA. However, it can be one order of magnitude smaller for $3d$ transition metal films.

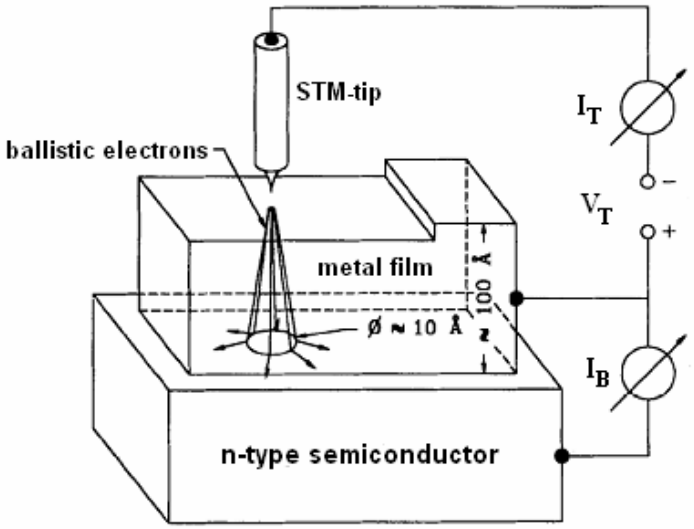

Figure 2.4: Schematic view of a Ballistic Electron Emission Microscopy (BEEM) experiment at a metal/semiconductor structure. The electron trajectories in the metal film indicate the *acceptance cone* (see section 2.3.2). Taken from [*Prietsch*, 1995].

The simplified energy band diagram of a BEEM experiment is shown in figure 2.5, together with a schematic evolution of the BEEM current. At this point we consider only energy constraints; electron refraction effects at the metal/semiconductor interface are not taken into account. Due to the applied tunnel voltage, with the tip under negative voltage with respect to the base, the potential energy for electrons lies higher in the STM tip than in the base. Thus, electrons entering the base by tunneling through the vacuum barrier, have energies high above the Fermi level in the base metal. As long as the energy provided by the tunnel voltage, eV_T, is smaller than the Schottky barrier height, no electrons will be transferred into the semiconductor, thus the BEEM current is zero. The gradual increase of V_T leads to a situation where some

[1] At this point momentum selection rules are neglected (see section 2.3.2)

of the injected electrons can overcome the Schottky barrier and progress through the conduction band of the semiconductor. This causes a measurable BEEM current at the collector electrode. The higher the tunnel voltage, the more electrons will contribute to I_B.

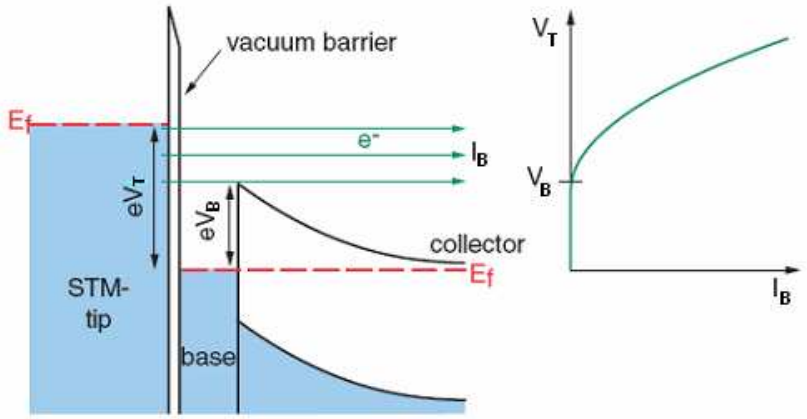

Figure 2.5: Left part: schematic energy diagram of a BEEM experiment. Right part: BEEM current spectrum $I_B(V_T)$ corresponding to the energy diagram on the left. Defining the Fermi level of the base as the zero potential level, the BEEM current onset is $V_T = V_B$. Taken from [*Smoliner et al.*, 2004].

Figure 2.6 shows the BEEM spectra measured on Au/Si structures and published in the original work of Kaiser and Bell [*Kaiser and Bell*, 1988]. The BEEM current is zero up to $V_T \approx$0.8 eV, equal to the Schotkky barrier height. However, for V_T greater than 0.8 eV, the spectra exhibit an abrupt threshold and a rapid increase in I_B, during which the BEEM current depends quasi-linearly on the injected current. Spectra for various values of injected current I_T are shown.

The case described above, corresponds to a BEEM structure fabricated by using an n-type semiconductor, and applies for the whole of this work. A BEEM structure can be fabricated as well by using a p-type semiconductor. In this case, the semiconductor band bending at the metal/semiconductor contact provides an energy filter for hot holes, that is holes with energy much lower than the Fermi level energy. Analogously to the previous case, ballistic holes are injected into the base, by lowering the tip Fermi level below the base Fermi level. A distribution of holes is created in the metal base, and the ballisticaly transported holes are energy filtered and collected by the semiconductor terminal [*Hecht et al.*, 1990].

Schottky contact

The Schottky metal/semiconductor contact is probably the most essential part of a BEEM sample, since it performs the energy filtering of the hot carriers. The scope

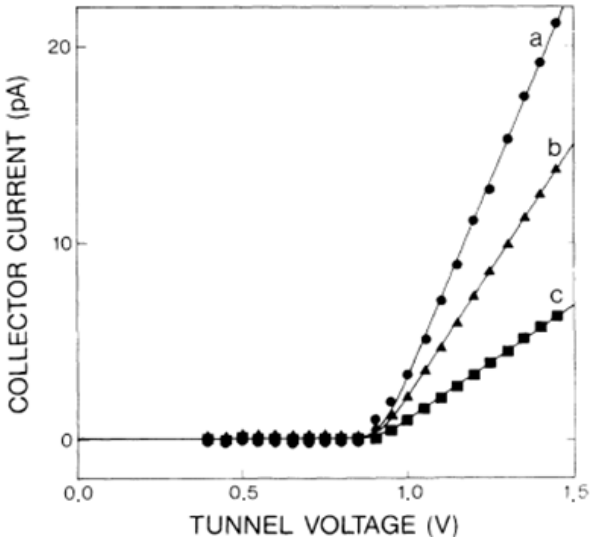

Figure 2.6: BEEM current versus tunnel voltage (I_B and V_T respectively, for this thesis) curves from the first BEEM study, taken on a Au/Si(100) junction. Curves (a), (b), and (c) were measured at tunnel currents of 0.87, 0.57, and 0.27 nA respectively. Solid lines represent the spectra calculated using the model proposed along with the demonstration of the technique. Taken from [*Kaiser and Bell*, 1988].

of this paragraph is to explain the presence of the potential barrier at the metal/-semiconductor interface; only the basic theory of the Schottky contact will thus be discussed. The simple case considered, is an ideal contact between a metal and an n-type semiconductor in the absence of surface states, with the metal having higher work function than the semiconductor [*Sze*, 1981; *Brillson*, 1982].

Figure 2.7 shows the electronic energy relations and the band bending scheme. On the left, the metal and the semiconductor are not in contact, and the system is not in thermodynamic equilibrium. The work function is the energy difference between the Fermi level and the vacuum level, and is denoted as Φ_M and Φ_{SC} for the metal and the semiconductor respectively. The electron affinity χ_{SC} is also shown, which is the energy difference between the conduction band minimum and the vacuum level in the semiconductor. When a metal is making intimate contact with a semiconductor, the Fermi levels in the two materials must be coincident at thermodynamic equilibrium. In addition, the vacuum level must be continuous. These two requirements determine a unique band diagram for the ideal metal/semiconductor contact, as shown on the right of figure 2.7.

After contact has been established, electrons flow from the semiconductor to the metal, depleting of electrons a characteristic region in the semiconductor. With the two Fermi levels aligned, a layer forms with a voltage drop equal to the contact potential $\Phi_M - \Phi_{SC}$. The layer consists of a space charge region (W), and an induced charge on the metal surface. The space charge region is calculated to be

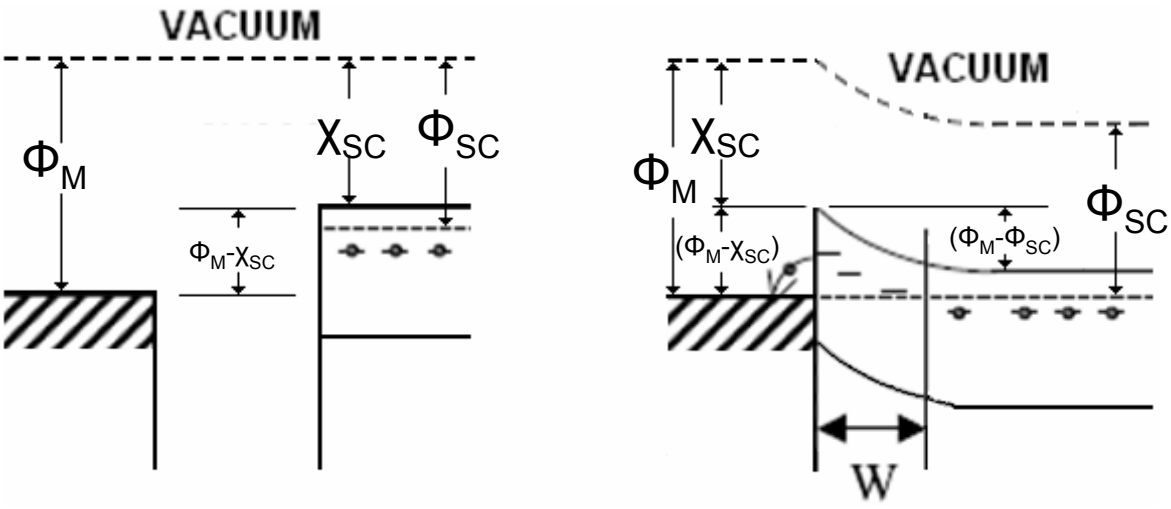

Figure 2.7: Schematic diagrams for band bending before and after metal/semiconductor contact for n-type semiconductor and a metal having higher work function than the semiconductor. The Schottky barrier height Φ_B equals $\Phi_M - \chi_{SC}$. W denotes the width of the depletion region. An analogous band bending scheme can be constructed for the case of a p-type semiconductor.

$$W = \sqrt{\frac{2\epsilon_s}{e^2 N_D}(\Phi_M - \Phi_{SC} - \frac{V}{e} - k_B T)} \tag{2.1}$$

where ϵ_s is the semiconductor permitivity and N_D is the donor concentration, while V is the applied bias and e is the absolute value of the electron charge. In the simple description discussed here, the Schottky barrier height is equal to the difference between the metal work function and the electron affinity of the semiconductor $\Phi_B = \Phi_M - \chi_{SC}$. For a more detailed description see [*Sze*, 1981].

The current flowing through the Schottky barrier is described by the thermionic emission model developed by Bethe [*Sze*, 1981]. The model is based on the assumptions that (I) the barrier height Φ_B is much larger than $k_B T$, (II) thermal equilibrium is established at the plane that determines emission, and (III) two current fluxes are superimposed-one from metal to semiconductor, the other from semiconductor to metal. Because of these assumptions, the shape of the barrier profile is irrelevant and the current flow depends solely on the barrier height. The current density is given by the formula

$$J = J_s \left(\exp\left(\frac{eV}{k_B T}\right) - 1 \right) \tag{2.2}$$

where the saturation current J_s is

$$J_s = A^* T^2 \exp\left(-\frac{\Phi_B}{k_B T}\right) \tag{2.3}$$

and A^* is the effective Richardson constant which is equal to

$$A^* = \frac{4\pi e m^* k_B^2}{h^3} \tag{2.4}$$

The value A=120 A/cm^2/K^2 for free electrons is used for Si, since at room temperature the choice of A^* does not affect substantially Φ_B.

In practice the current traversing a Schottky contact is described by the two parameter formula

$$J = J_s \left(\exp\left(\frac{eV}{nk_B T}\right) - 1\right) \tag{2.5}$$

where the fitting parameters are the saturation current J_s and the diode ideality factor n. The latter correspond to any kind of variation of the Schottky barrier, the image force lowering of the barrier height [*Sze*, 1981], for instance.

2.3.2 Hot electron transport in BEEM

In the detailed description of a BEEM experiment, four consecutive steps are usually considered [*Prietsch*, 1995]: (1) tunneling from the tip into the metal base layer, resulting in an angular and energy distribution of electrons at the surface of the metal film; (2) hot electron transport through the metal base layer, where elastic and inelastic scattering processes occur; (3) transmission across the interface from the metal into the semiconductor, which depends on energy and momentum constraints; (4) transport inside the semiconductor, where impact ionization can occur.

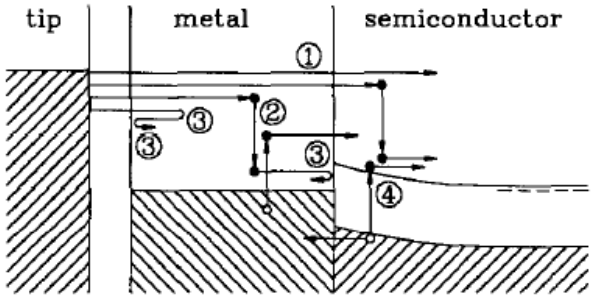

Figure 2.8: The different scattering mechanisms in a BEEM experiment:(1) pure ballistic transport, (2) inelastic scattering in the metal film, (3) elastic scattering in the metal film or (in form of reflection) at its surface or the interface, and (4) impact ionization in the semiconductor. Taken from [*Prietsch*, 1995].

The different scattering mechanisms of hot electrons during their path from the tip to the semiconductor are shown in figure 2.8. Beside the pure ballistic trajectories (1), there are several possible scattering processes: Inelastic electron-electron scattering (2) may occur in the metal film, reducing the energy of the primary electron. Such a process generates secondary hot electrons, which may also cross the interface. In addition, elastic scattering in the metal film and reflection at both the metal surface and the interface may lead to changes in momentum (3). Finally, after transmission across the interface, inelastic scattering in the semiconductor can lead to impact ionization (4), where an electron-hole pair is excited, which can contribute another electron to the BEEM signal.

In the following, the four different steps of the BEEM process will be discussed.

The tunneling current distribution

The energy distribution of the tunneling current can be described in a first step by assuming a planar tip, so that planar tunnel theory can be applied [*Simmons*, 1964]. While the spatial distribution depends critically on details of tip shape and surface morphology, usually only the approximate description of an injected electron beam laterally confined within an area of atomic dimensions is considered. The energy distribution of the injected electrons is described by an exponential decay, starting at the Fermi level of the tip, eV_T. For an energy decrease equal to

$$E_0 = \frac{\hbar}{d}\sqrt{\frac{\Phi_M - eV_T/2}{2m}} \tag{2.6}$$

where d is the width of the tunnel barrier, Φ_M is the metal work function and m the free electron mass [*Thiaville et al.*, 2007], the tunneling probability decreases to $1/e$. Using typical values d=1 nm and Φ_M=4 eV, one finds a weak dependence of E_0 on tunnel voltage: E_0 is 0.39, 0.37 and 0.34 eV, for tunnel voltages 0, 1 and 2 V, respectively [*Thiaville et al.*, 2007].

Transport through the metal film

Inelastic hot electron scattering As has been mentioned in section 2.2, electron-electron inelastic scattering is the main source of energy loss during electron transport, in the energy range studied. Two body collision **1**+**2**→**3**+**4** between an electron in the excited state **1** and an electron in the filled state **2** in the Fermi sea (figure 2.9a), is discussed in the framework of the free electron model [*Kittel*, 1976].

Because of the exclusion principle the states **3** and **4** of the electrons after collision must lie outside the Fermi sphere, since all states within the sphere are already occupied; thus $E_3 > E_F$ and $E_4 > E_F$. The conservation of energy requires that $E_2 > 2E_F - E_1$, for otherwise E_3 and E_4 cannot lie outside the Fermi sphere. This means that collisions are possible only if state **2** lies within a shell of thickness $E_1 - E_F$ within the Fermi surface. Moreover, states **3** and **4** cannot have energy higher than E_1,

so they should lie within a shell of thickness $E_1 - E_F$ above the Fermi level (figure 2.9b). Thus, the collision probability is proportional to the square of the difference between the incident electron energy and the Fermi energy, since this difference determines both the number of states with which an electron can interact and the number of states to which electrons can be excited. This is schematically shown in figure 2.9c, where the surface of the allowed "phase space" area is proportional to $(E_1 - E_F)^2$.

The mean-free path for electron-electron inelastic scattering (λ_i) is equal to the product of the relaxation time $\tau(E)$ and electron velocity $v(E)$

$$\lambda_i(E) = v(E) \times \tau(E) \tag{2.7}$$

In the free electron approximation discussed here, the electron velocity is proportional to the square root of energy. The relaxation time is inversely proportional to the collision probability. Altogether, writing $E_1 = E$, one finds

$$\lambda_i \ \propto \ \frac{E^{1/2}}{(E - E_F)^2} \tag{2.8}$$

The above relation indicates the energy dependence of the dominant electron-electron scattering mechanism [*Crowell and Sze*, 1967].

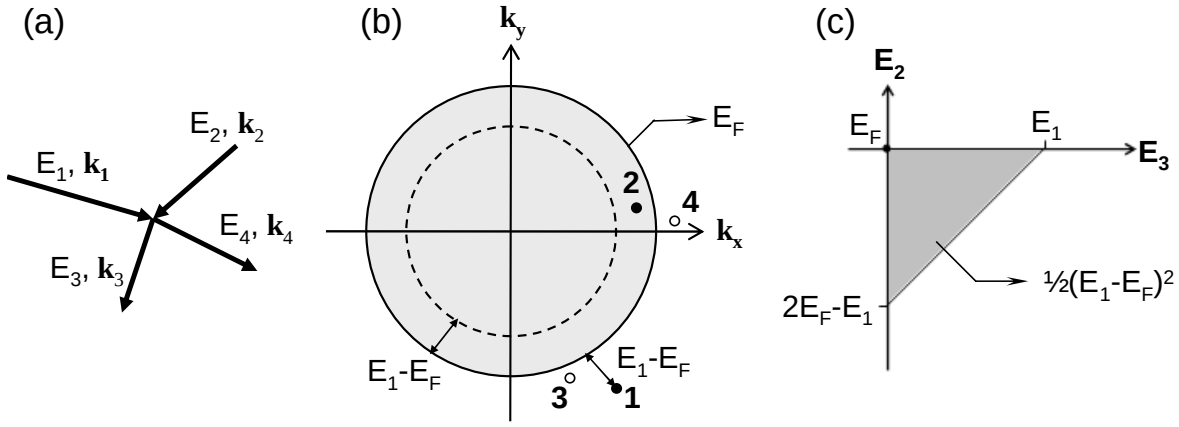

Figure 2.9: (a) A collision between two electrons of wavevectors k_1 and k_2. After the collision the particles have wavevectors k_3 and k_4. (b) The electrons in initial states **1** and **2** collide, and occupy states **3** and **4** after collision. The graph ensures the conservation of momentum. (c) "Phase space" (limited to energy) indicating the possible final states of electron **1** and the possible initial states of electron **2**.

The above simple model sufficiently describes hot electron transport in real materials. The case of Au and Pt will be discussed. Figure 2.10 shows the band structure of Pt compared to that of Au. The main difference lies in the density of states below the Fermi level. While Au has almost no possible states down to ≈1.8 eV below the Fermi level, in the case of Pt those levels are filled with electrons which can interact

with the excited electrons, contributing to electron-electron scattering. Although the hot electron inelastic mean-free path for Pt has not been measured, from the Pt band structure a value considerably smaller than that of Au (74 nm [*Crowell et al.*, 1962]) is expected. Indeed, from *ab-initio* calculations taking into account the material band structure [*Chulkov et al.*, 2006], an inelastic mean-free path ≈5 nm is found for Pt, in contrast to the several 10 nm value found for Au.

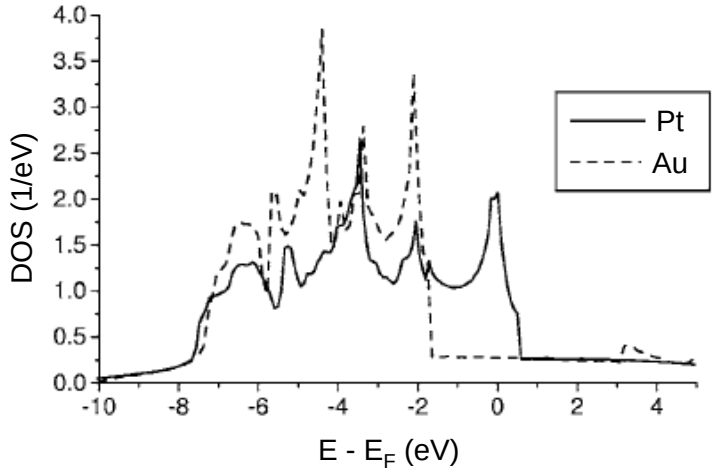

Figure 2.10: Total densities of states in Pt and Au. Taken from [*Zhukov et al.*, 2006].

Hot electron attenuation length The attenuation of the hot electron current in the metal film is described by an exponential decay [*Prietsch*, 1995], thus the BEEM current is given by the formula

$$I_B = I_T \exp\left[-\frac{t}{\lambda(E)}\right] \tag{2.9}$$

where t is the distance that the hot electrons have traveled (the film thickness in this case), and λ(E) is a quantity named *attenuation length* and it is defined by equation 2.9. I_T is the injected (tunnel) current. Experimentally, λ can be determined by performing a study of BEEM transmission versus metal base thickness.

Elastic hot electron scattering Elastic scattering is as well important in a BEEM experiment. The strongly different effective masses in the metal base and the semiconductor collector, create momentum restrictions during electron transport through the Schottky interface, disfavoring electrons with momentum highly off-normal to the metal/semiconductor interface (see next section). Elastic scattering causes momentum changes and results in the momentum randomization of the initially strongly forward-focused electron beam. As a result, the BEEM current is reduced because of momentum

filtering. In this case the exponential dependence of the BEEM current described in equation 2.9, is considered with an attenuation length equal to

$$1/\lambda(E) \;=\; 1/\lambda_i(E)+1/\lambda_e(E) \tag{2.10}$$

where λ_i and λ_e are respectively the electron inelastic and elastic attenuation lengths in the metal. As has been mentioned in section 2.2, electron-defect and electron-impurity collisions introduce elastic scattering, which is energy independent. Thus, λ_e is related to the material quality, through the defect and impurity density, by contrast to the intrinsic dependence of λ_i to electron-electron collisions.

The sensitivity of BEEM to both inelastic and elastic attenuation lengths explains the difference in the λ values obtained from photoemission (PE) and BEEM experiments. In PE, hot electrons are created in the metal with their momentum vector already random, thus elastic scattering does not contribute to the collector signal. In the case of Au, a value of λ_{PE} =74 nm is determined by PE experiments using the overlayer technique [*Crowell et al.*, 1962], and it is much higher than the value λ_{BEEM} =28 nm determined by BEEM [*Weilmeier et al.*, 1999], since in the latter case the shorter elastic attenuation length is also taken into account. Considering λ_{PE}=λ_i and λ_{BEEM}=λ, a value λ_e=45 nm is calculated from equation 2.10, which is in good agreement with the value 38 nm quoted in the literature for the elastic scattering length of Fermi level electrons[2] in Au [*Chopra*, 1969].

In addition to the attenuation effects of the ballistic electrons, inelastic scattering in the metal film via electron-electron interaction will also lead to secondary electrons. A ballistic electron with energy E can suffer an energy loss between zero and E, and the number of possible secondary electrons which can be excited increases linearly with this energy loss. Those secondary electrons may have sufficient energy to cross the interface and form an inelastic background in the BEEM spectrum. Considering only energy filtering at the Schottky barrier, secondary electrons start to become measurable for injection energies higher than twice the Schottky barrier. Moreover, because of the energy dependence of inelastic scattering which allows low-energy electrons to reach the interface more easily, this background will dominate the BEEM current at even higher tip voltages [*Prietsch*, 1995]. However, momentum selection rules at the metal/semiconductor interface reduce considerably the possibility of collecting secondary electrons (see next section).

Transmission across the metal/semiconductor interface

Up to now, only energy restrictions were considered during the transport of hot electrons through the Schottky barrier. The momentum filtering at the metal/semiconductor interface will be now discussed. Most models used to describe the hot electron transport are based on the assumption that during the transport through the interface the momentum parallel to the interface, k_{xy} (see figure 2.11), is conserved [*Bell*,

[2]Elastic scattering is considered to be energy-independent.

1996]. The "parallel momentum conservation law", as it is often called, was initially derived for an idealised quantum mechanical system, but it soon became clear that this conservation law is in fact valid for the vast majority of actually conducted BEEM experiments [*Prietsch*, 1995].

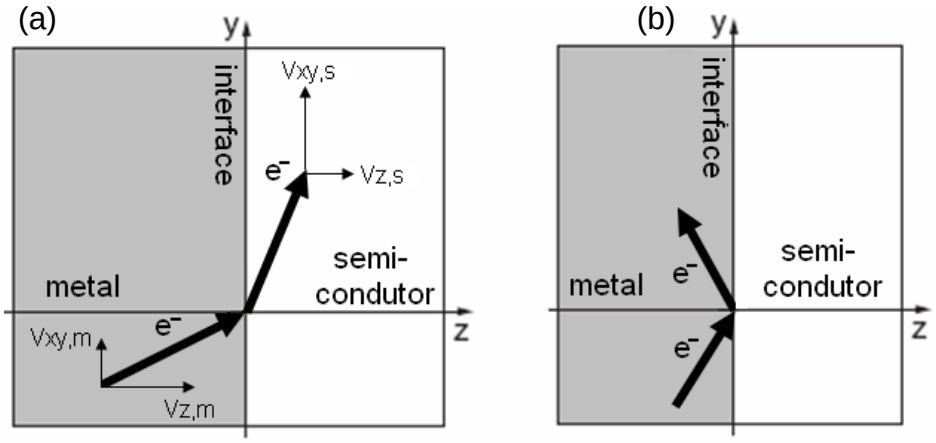

Figure 2.11: Effects observed during the electron transport through the metal/semiconductor interface. (a) Refraction effect at low incidence angle. (b) Reflection effect at high incidence angle. Adapted from [*Smoliner et al.*, 2004]

The xy-momentum conservation has as a consequence the observation of electron "refraction" effects (see figure 2.11). Typical BEEM samples exhibit a potential step between the base and the collector (caused by the Schottky barrier), as well as different effective masses in the involved areas. The effective electron mass in the metal is equal to the free electron mass, m_0, while the effective electron mass in the semiconductor, m^*, is considerably smaller (for the transverse effective mass in Si: $m^* = 0.19\ m_0$). Since the xy-momentum is conserved during transport from the metal (m) to the semiconductor (s) ($k_{xy,m} = k_{xy,s}$), then $m_0 v_{xy,m} = m^* v_{xy,s}$. Thus, by crossing the interface, the electron will gain velocity parallel to the interface, and lose velocity perpendicular to it, because of the conservation of energy.

A direct consequence is the possibility of total reflection at the metal/semiconductor interface. Considering the configuration of a BEEM experiment, it is obvious that only electrons with $k^z > 0$ can travel through the metal/semiconductor interface and finally be collected at the semiconductor. This automatically gives an upper limit for k_{xy} and, therefore, a maximum angle of incidence (with respect to the z-axis) for an electron in the base in order to be collected. This *critical angle* θ_{crit} is calculated [*Smoliner et al.*, 2004] to be

$$\sin^2(\theta_{crit}) = \frac{m^*}{m_0} \frac{eV - \Phi_B}{eV + E_f}, \tag{2.11}$$

where Φ_B, now, is the usual Schottky barrier height and E_f is the position of the Fermi level with respect to the conduction band minimum in the base layer, while m_0 and

m^* are the free electron mass and the effective electron mass in the semiconductor. $eV + E_f$ is the total energy of the incident electron, e.g. provided by a tunnel voltage. Electrons are able to cross the interface, only if their angle of incidence, θ, fulfills the requirement

$$\sin(\theta) \leq \sin(\theta_{crit}) \tag{2.12}$$

Electrons with a larger angle of incidence will be reflected at the interface, as depicted in figure 2.11. In a BEEM experiment, this condition defines the opening angle of the so-called *acceptance cone* (see figure 2.4) for electrons in the metal film. Electrons reaching the metal/semiconductor interface are reflected if lying outside the acceptance cone, even when they have energies higher than the Schottky barrier height.

In the case of the Au/Si interface, the values are $m^* = 0.19\ m$ and $\Phi_B = 0.8\ eV$. The acceptance cone at an energy 0.1 eV above threshold is calculated to be just 3.5 °. These small critical angles have a crucial effect on the lateral resolution of BEEM. Only electrons within the acceptance cone will determine the lateral resolution, because only those will be able to enter the semiconductor and therefore to contribute to the BEEM current. Assuming a point-like electron source at the top of the base layer, the minimal lateral resolution is determined by

$$\Delta x = 2d \tan(\theta_{crit}) \tag{2.13}$$

where d is the thickness of the base layer. Taking the critical angle calculated above, the lateral resolution will be 1.2 nm for a 10 nm thick base layer. Note that elastic scattering in the base layer will not deteriorate the lateral resolution. Electrons removed from the acceptance cone by changing their angle of incidence will only lead to an overall decrease of the BEEM current.

Transport in the semiconductor

Among the mechanisms of inelastic scattering in the semiconductor observed with BEEM, impact ionization is the most prominent, leading to the excitation of secondary electrons. Electrons with kinetic energies in the semiconductor above the band-gap energy E_G (1.12 eV at 300 K for Si [*Sze*, 1981]) can excite an electron-hole pair, which can be separated by the potential in the depletion layer. Impact ionization affects the BEEM signal for energies higher than $2E_G$, when an additional electron contributes to the BEEM current. At even higher energies, more than one electron-hole pair can be excited [*Prietsch*, 1995].

Attenuation length versus mean-free path

In closing, it may be useful to stress that we do not yet perfectly know and control how hot electrons are transmitted through the metal base and collected in the semiconductor.

Indeed, one the one hand, we have an idealized model of BEEM, where (i) the semiconductor has a conduction band with bottom at zero xy momentum; (ii) the metal

/ semiconductor interface is perfectly flat, hence conserves perfectly the xy momentum; (iii) the injected electrons have their momentum fully aligned along the z direction.

In such a case, any scattering event will add some xy momentum to the hot electron. For energies weakly above the threshold, where the acceptance cone width is very small, this means that such a scattered electron will not be collected (we are here in the limit where the layers are thin so that the probability of 2 scattering events is negligible). Thus, the attenuation length is given by (2.10) where the attenuation lengths λ_i and λ_e are the corresponding mean free paths.

However, there are several reasons to think that this idealized model is really too ideal.

- Experiments on Au/Si(111) give BEEM currents similar to those measured on Au/Si(100), although the latter case fulfills (i) whereas the former does not. This was seen already in the very first BEEM experiments, and has lead to a big controversy that is apparently not yet settled. An important proposed explanation for this similarity was the presence of a very strong elastic scattering.

- The few experiments having tried to measure the spatial resolution of BEEM, and its energy dependence, do not all coincide with (2.13).

Thus, on the other hand, if one assumes that elastic scattering is an essential process in BEEM, then clearly λ_i and λ_e are different from the corresponding mean-free paths. Indeed, a hot electron undergoing an elastic scattering event will not always be lost for collection. It can even be regained if this scattering realigns its momentum along the direction where it can be collected. In such a case, it is more appropriate to consider attenuation lengths, that depend on energy, substrate, etc. However, it also becomes much more difficult to try to understand these lengths in simple physical terms.

As this controversy is not fully settled, in this thesis, as a first approximation we try to understand our results in the framework of the idealized model.

2.3.3 Spectroscopy and imaging modes

Ballistic Electron Emission Spectroscopy (BEES)

BEES can provide information on transport properties of hot electrons between the tip and the semiconductor. During BEES, the STM tip is held stationary above a specified surface point. By sweeping the tunnel voltage with the STM feedback loop activated, a constant current electron beam is injected into the base, while simultaneously recording the collector signal. A BEES spectrum is a collector signal versus tunnel voltage ($I_B(V_T)$) graph, and it is a direct probe of scattering effects in the base layer, as well at potential barriers in the metal semiconductor interface or inside the collector.

The first BEES studies concerned the determination of the local Schottky-barrier height at the metal/semiconductor interface. When introducing BEEM, Bell and Kaiser presented a formula for the modeling of the BEEM current (usually called the

Bell-Kaiser (BK), or phase-space model), which has been widely utilized in BEEM/-BEES since then [*Bell and Kaiser*, 1988]. The BK model considers only the conservation of energy and transverse momentum parallel to the interface, while the calculations framework is planar tunneling. Besides, electrons are described in the free electron approximation, having the free electron mass in the metal base and an effective mass in the semiconductor. The quantum mechanical transmission coefficients of the current through the base/collector interface are not considered. Close to the voltage threshold (the Schottky barrier height) and at zero temperature, this model evaluates the BEEM current normalized to the injected tunnel current as a square law of the voltage excess.

A refinement of the BK model by the introduction of the wave transmission coefficients of the electrons at the metal/semiconductor interface [*Prietsch and Ludeke*, 1991], results into a 5/2 power law close to the threshold. Therefore BEES spectra are often fitted around the threshold region, by a simple power law

$$I_B/I_T = A\,(V - V_0)^n \tag{2.14}$$

As the measured BEEM current varies quasi-linearly with voltage from ≈ 0.2 V above threshold (see figure 2.6), it is clear that this approach is not fully satisfactory.

Recently, fully analytical expressions of the BEEM spectra based on the BK model were attained, that allow fitting the experimental data in the full range of voltages, under the assumption that λ do not depend on energy [*Thiaville et al.*, 2007]. At zero temperature, the tunneling and BEEM currents are calculated to be

$$I_T = C\,\left[1 - \exp\left(-\frac{eV}{E_0}\right) - \frac{eV}{E_0}\exp\left(-\frac{E_F}{E_0}\right)\right] \tag{2.15}$$

$$I_B = C\,\left[1 - \frac{m}{m-m^*}\,\exp\left(-\frac{m^*}{m}\,\frac{eV-\Phi_B}{E_0}\right) - \frac{m^*}{m-m^*}\,\exp\left(-\frac{eV-\Phi_B}{E_0}\right)\right] \tag{2.16}$$

The characteristic energy E_0 is given by equation 2.6. This is one of the main assumptions underlying the full analytical calculation of the BEEM spectra.

Taking into account a finite temperature, it can be seen that only a narrow voltage region of width $\approx$200 mV at 300 K is affected. In this case, the relative BEEM current takes off at a lower voltage, however, the quasi-linear slope above the threshold is not affected. Temperature effects matter for example when trying to measure the exponent of the power law quoted before, as a thermal broadening obviously decreases the threshold and increases the exponent. If the full spectrum is analyzed, however, the temperature effect is anticipated to be weak. In fact, fitting the values obtained with a non-zero temperature by expressions for zero temperature, gives only tiny differences in threshold voltage and slope.

The experimental spectra are fitted under the assumption that an overall *constant* transmission factor T exists, equal to

$$T \;=\; T_{int}\,T_{met} \tag{2.17}$$

where T_{int} is a factor describing the current transmission at the metal/semiconductor interface, and T_{met} is a factor that corresponds to the hot electron transmission across the metal base,

Two parameters are obtained from such fits, namely the Schottky barrier height Φ_B and the multiplicative factor T (equation 2.17) called transmission and satisfying

$$\left.\frac{I_B}{I_T}\right|_{exp} = T \times \left.\frac{I_B}{I_T}\right|_{model} \tag{2.18}$$

where the model terms are given by equations 2.16/2.15 for the zero temperature case. As deviations from the planar tunneling assumption are anticipated, the transmission factor deduced from equation 2.18 should be considered only as an indicative value. Moreover, as it is shown in section 6.2.4, the assumption of an energy independent λ is not always valid.

BEEM imaging

BEEM imaging is performed in a manner similar to STM imaging. The STM tip is scanned over the sample surface under constant tunnel voltage, with the feedback loop activated maintaining a constant tunnel current. The collector signal is simultaneously recorded providing the BEEM current image, in supplement to the STM surface topography image. Lateral variations of the BEEM current are frequently observed, even on an atomic scale as can be seen in figure 2.12 [*Sirringhaus et al.*, 1995]. BEEM imag-

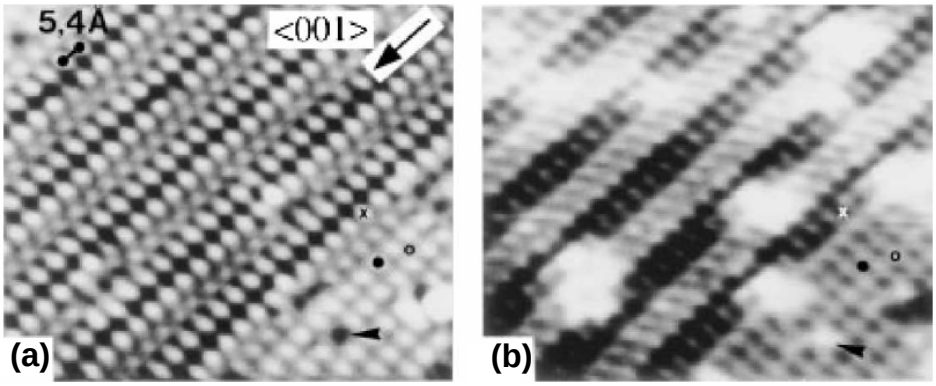

Figure 2.12: STM topographic image (a) and the BEEM image (b) simultaneously recorded at 77 K on epitaxial $CoSi_2$/n-Si(100) (V_t=1.5 V, I_B=3 nA, film thickness d=3.8 nm). Two different surface reconstructions are apparent, and the BEEM contrast reflects the atomic scale periodicity of the surface topography. Taken from [*Sirringhaus et al.*, 1995].

ing is performed to investigate inhomogeneities in hot electron transport. Comparing BEEM data to STM images allows for a direct comparison of the transport behavior

versus structural properties of the metal film. These inhomogeneities are often observed on length scales as low as 1 nm, and may even consist of patches on the surface with no measurable BEEM current at all.

Inhomogeneities in hot electron transport can be related to a variety of contributions: tunneling, transport through the film, and interface transmission. A proper separation of these contributions is the main challenge in the interpretation of BEEM images, since BEEM-current variations can have several origins. The spatial and energetical distribution of the electrons tunneling from the tip depends on the injection geometry and thus on surface corrugation. Elastic scattering can occur in the metal film, e.g. at dislocations, grain boundaries, or different chemical species. Inelastic electron-electron scattering is dependent on the local metal film thickness according to equation 2.9. Lateral variations in electronic, chemical, or spatial interface structure can result in an inhomogeneous interface transmission. Lastly, magnetic structures can be locally imaged with BEEM, since hot electron scattering in ferromagnetic metals is strongly dependent on the electron spin orientation (see sections 2.4 and 2.5).

2.3.4 Scattering BEEM

As shown earlier, BEEM structures can be fabricated by using either an n-type or a p-type semiconductor. In both cases, only majority currents from the base into the collector are detected during a BEEM experiment. The terms majority and minority carrier, as used here, are defined with reference to the substrate type. Thus, electron injection leads to ballistic electron detection by the n-type substrate, while hole injection leads to ballistic hole detection by the p-type substrate.

The cases described above correspond to a forward bias BEEM experiment, where majority carriers are injected into the metal base, and are ballisticaly transported over the Schottky barrier (figure 2.13a, case A). In reverse bias, minority carriers are injected into the base [*Bell et al.*, 1990]. In the case of n-type semiconductor collector, electrons are extracted from the metal film creating a ballistic hole distribution. The peak of the hole distribution is fixed at the sample Fermi level, in contrast to forward bias BEEM, where the peak of the electron distribution follows the tip Fermi level [*Hecht et al.*, 1990]. A hole may be filled by an electron near E_F, and through an Auger energy transfer process, another Fermi level electron can be excited (figure 2.13a, case B). If the hole is initially sufficiently far below E_F, the Auger electron may have sufficient energy to overcome the Schottky barrier and be detected in the semiconductor [*Bell et al.*, 1990; *Ludeke and Prietsch*, 1991].

Inelastic scattering in the base is the source of signal in this Scattering BEEM (SBEEM) process[3]. Figure 2.13b shows experimental spectra taken on Au/Si(n-type). The sign of the Y axis is positive, since electrons are collected at the n-type semiconductor substrate, as in the case of BEEM,. In this case however, the collector signal does not correspond to electrons transmitted ballistically through the metal base. The SBEEM yield is significantly lower, since the process involves three electrons, and is

[3] Also called Auger-BEEM [*Ludeke and Prietsch*, 1991] or Reverse-BEEM [*Niedermann et al.*, 1993].

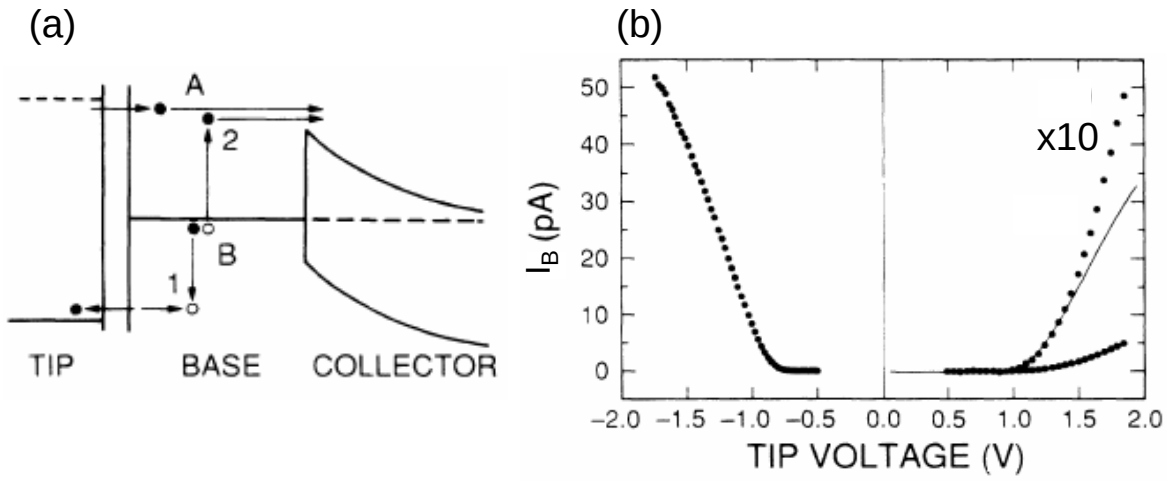

Figure 2.13: (a) Energy diagram for BEEM (case A) and for scattering BEEM (case B) with an n-type collector. (b) Experimental spectra for BEEM (left) and SBEEM (right) taken on Au/Si(n-type). A magnified plot of the SBEEM spectrum is also shown, with a fit by the theory (see text). Taken from [*Bell et al.*, 1990].

less effective. Moreover, the momentum of the excited electrons is isotropic, since their creation takes place in the metal film. Consequently, a greater fraction of the created hot electrons is momentum filtered at the metal/semiconductor interface, than in the case of BEEM. It should be noted that the momentum in this process is conserved, taking as well into account the momentum of the participating holes. After electron excitation, the discussion for the relaxation of hot electrons during transport in the solid (section 2.3.2), applies as well in this case.

It has been proposed, that this process contributes an additional $(V - V_0)^2$ factor to the BEEM current expressions discussed before (section 2.3.3) [*Bell et al.*, 1991], thus increasing the power n of equation 2.14 to 4, or to 4.5 considering the quantum mechanical transmission of electrons at the metal/semiconductor interface. An analogous SBEEM experiment can be performed using a p-type semiconductor [*Bell et al.*, 1990].

2.4 spin-dependent hot electron transport

Up to now only the electron energy and momentum were discussed as parameters affecting hot electron transport. However, the electron spin has to be also taken into account when studying hot electron transport in magnetic materials.

2.4.1 Experiments

Early studies on spin-dependent hot electron transport, were performed in the energy range a few eV above Fermi level, using photoemission (PE) experiments (see figure 2.1). Hot electron polarization was first demonstrated for photoemitted electrons from Gd [*Hofmann et al.*, 1967; *Busch et al.*, 1969]. Experiments with Ni demonstrated the spin polarization of electrons photoemitted from a 3*d* magnetic metal [*Banninger et al.*, 1970].

The spin-dependent attenuation lengths or lifetimes of excited electrons were determined in order to quantify the effect. In a variation of the PE experiments, samples consisting of ultrathin Fe layers on Cu(100) show a substantial polarization of the Cu 3*d* peaks, which was attributed to spin-dependent attenuation in the Fe overlayer. The spin-dependent attenuation length in the energy range from a few eV to a few tens of eV was obtained by varying the Fe overlayer thickness [*Pappas et al.*, 1991]. The majority λ was measured to be higher than the minority λ, and both values were on the order of a few Å.

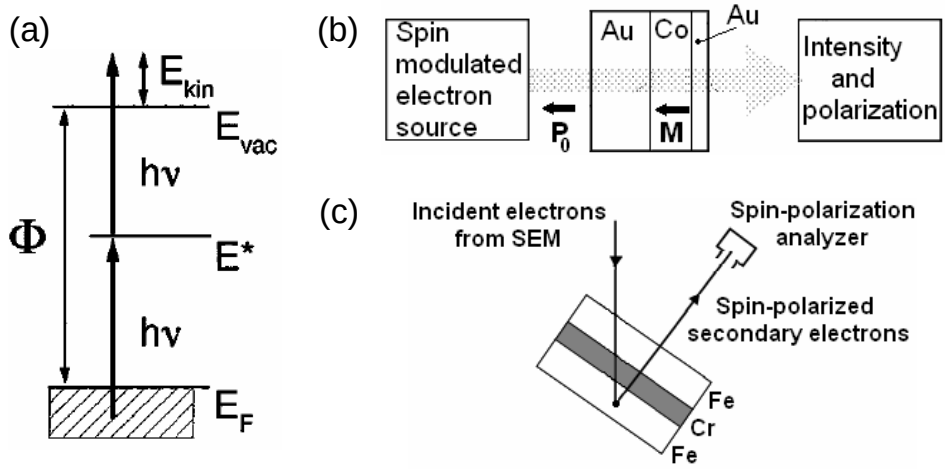

Figure 2.14: (a) Scheme of the energy levels involved in the 2PPE process. (b) Experimental setup of the spin-filter experiments on free-standing Co foils. (c) Secondary electron spin-valve effect studied using scanning electron microscopy.

Two photon photoemission (2PPE) experiments were performed to measure the spin dependence of the lifetime of excited electrons in remanently magnetized fcc Co films. 2PPE involves the excitation of electrons to an intermediate energy level (E^*) by a first ultrashort pump laser pulse, followed by a second, suitably delayed, probe laser pulse which leads to photoemission of the electrons (figure 2.14a). This two pulse correlation experiment allows one to determine lifetimes in the fs range, considerably shorter than the duration of the laser pulse. At 1 eV above the Fermi level, the lifetime of majority-spin electrons was measured to be twice as long as that of minority-spin electrons, and both are in the fs range [*Aeschlimann et al.*, 1997].

The spin-filter effect was demonstrated by measuring the preferential transmission of majority electrons in magnetic metals. The transmission of a spin-polarized, free-electron beam through a remanently magnetized, free-standing magnetic metal layer, was measured in the energy range 4-50 eV (figure 2.14b). The samples used were Au sandwiched, ultrathin cobalt foils, exhibiting perpendicular magnetization. The transmission of majority-spin electrons is favored, and the largest effect is observed at energies a few eV above the Fermi level [*Lassailly et al.*, 1994].

The hot electron spin valve effect was observed for secondary electrons emitted from Fe/Cr/Fe trilayers. Experiments were performed using scanning electron microscopy with polarization analysis (SEMPA). The secondary electrons produced by the incident beam of a scanning electron microscope are polarized while traversing the spin-valve (figure 2.14c), and their polarization is directly measured by the polarization analyzer [*Unguris et al.*, 1991]. A secondary spin-polarized electron created in the lower layer, is spin-filtered while traversing the upper layer. This way, the exchange coupling between the two Fe layers by varying the Cr layer thickness was studied.

2.4.2 Theoretical framework

The asymmetry in the scattering of hot majority-spin and minority-spin electrons, was initially explained in the basis of the imbalance between unfilled majority- and minority-spin electronic states [*Penn et al.*, 1985; *Gröbli et al.*, 1995]. Because of the exchange splitting in ferromagnetic materials, there is an excess of unfilled minority-spin d states over unfilled majority-spin d states, so excited minority-spin electrons have more empty states to scatter into. Minority-spin electrons are therefore scattered out of a given energy at a faster rate than majority-spin electrons. This results in a shorter inelastic lifetime of excited electrons, for minority as compared to majority electrons, thus leading to a shorter attenuation length.

Compiling the data of many attenuation experiments on a number of materials, an empirical rule was derived for inelastic scattering of excited electrons: the dominant electron-electron scattering rate is proportional to the number of unoccupied electronic states above the Fermi level, into which excited electrons can scatter [*Schonhense and Siegmann*, 1993]. This model is rather simple, since the contribution of the filled states below E_F to the scattering rate, is not considered (see equation 2.8). Moreover, only the lifetime asymmetry is discussed, and the electron velocity is neglected (see equation 2.7). Finally, the metal band structure is totally omitted.

Recent *ab-initio* calculations have demonstrated the importance of the metal band structure in explaining spin-dependent hot electron scattering in ferromagnets [*Zhukov et al.*, 2004; *Zhukov et al.*, 2006]. The strong d character (see for example figure 2.15) of the electrons in the energy range a few eV above and below E_F (the energy range of interest in BEEM experiments), precludes the use of the free-electron approximation. Both the spin-dependent lifetimes and velocities are found to be related with the specific band structure of each metal. The spin asymmetry of the attenuation lengths can be explained either by a spin asymmetry of the lifetimes (like in the case of Ni), or by

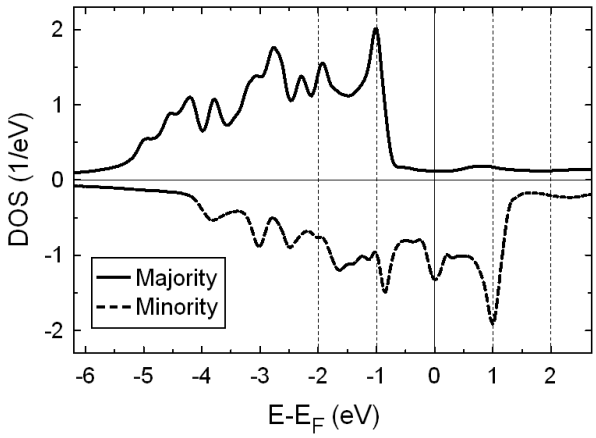

Figure 2.15: Density of states of Co (*Ab-initio* band structure calculation using CASTEP, performed by Alexandre Gloter, LPS, Orsay).

a spin asymmetry of the electron velocity (like in the case of Fe) [*Zhukov et al.*, 2006]. Results above are in agreement with a recent BEEM study on Fe layers [*Banerjee et al.*, 2007]. It should be noted that the first suggestion of spin-dependent velocities, concerned transport of hot holes [*Banerjee et al.*, 2005b]. For holes of different spin in Co, there is no significant difference in the number of states below E_F into which to decay (figure 2.15). However, a clearly spin-dependent hot hole transmission through Co layers, was demonstrated in BEEM experiments using a p-type semiconductor [*Banerjee et al.*, 2005b].

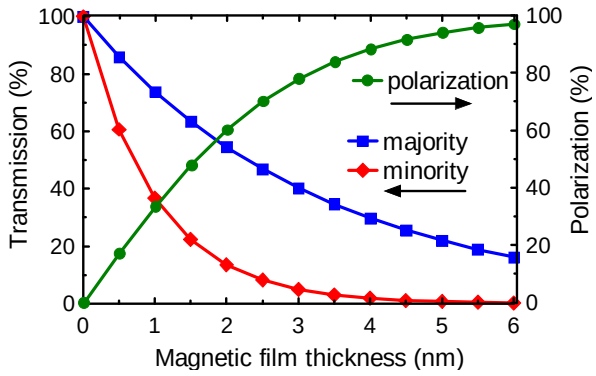

Figure 2.16: Graphic representation of the spin-dependent hot electron transport and spin-filtering effect in a ferromagnetic thin film. The polarization is equal to $(T_{maj} - T_{min})/(T_{maj} + T_{min})$.

As the hot electron attenuation lengths in ferromagnets are spin-dependent, hot electron transport in ferromagnets should be described by two conduction channels. The hot electron transmission through a ferromagnetic layer, is given by a formula

akin equation 2.9. However, in this case two exponential decays have to be considered, one for majority electrons (attenuation length λ_{maj}) and one for minority electrons (attenuation length λ_{min}). Thus, for two initially equal spin populations, the transmission through a magnetic layer is [*Pappas et al.*, 1991; *Gröbli et al.*, 1995]

$$T(E) \propto \left[\frac{1}{2}\exp\left(-\frac{t}{\lambda_{maj}(E)}\right) + \frac{1}{2}\exp\left(-\frac{t}{\lambda_{min}(E)}\right)\right] \tag{2.19}$$

As a consequence of the difference between λ_{maj} and λ_{min}, minority-spin electrons are preferentially filtered out if an electron beam passes through a ferromagnet. This is demonstrated schematically in figure 2.16. A non spin-polarized hot electron current is considered to be injected into a magnetic layer (in this case Co). As the minority-spin electrons are scattered in a faster rate, after transport through a distance equal to a few λ_{min} the electron current is strongly majority-spin polarized. The values used, are the ones determined in this thesis for the majority and minority hot electron attenuation length in Co (λ_{min}=1.0 nm and λ_{maj}=3.3 nm at 1.5 eV).

2.4.3 The spin-valve transistor

The first hot electron device relying on spin-dependent hot electron transport phenomena, was demonstrated with the development of the spin-valve transistor (SVT) in the mid-90s [*Monsma et al.*, 1995]. Beside its technological interest as sensor or in data processing and storage, this type of component allows for the study of spin-dependent electron transport in energies as low as 0.5 to 1.0 eV above the Fermi level, with easy access to low temperature conditions [*Jansen*, 2003].

The SVT is a three terminal hot electron device with the typical emitter/base/collector structure, where the base region is a metallic multilayer containing two magnetic layers separated by a normal metal spacer (see figure 2.17a). A magnetic multilayer structure consisting of two non-coupled magnetic layers separated by a non-magnetic layer is called a *"spin valve"*. Both the emitter/base and base/collector potential barriers are metal semiconductor contacts forming a device with a semiconductor/metal/semiconductor structure. Those Schottky barriers prevent Fermi level electrons from traveling through the structure. Suitable material selection should be taken into account in order to obtain the desired high quality barrier with good rectifying behavior and thermionic emission dominating. Moreover, the injection Schottky barrier should have a higher barrier height than the collection Schottky barrier. In the case of figure 2.17a, the Si/Pt ($\Phi_B \approx$0.9 eV) and Si/Au ($\Phi_B \approx$0.8 eV) Schottky barriers are used as hot electron emitter and collector respectively, while V_{BE} is the base-emitter bias and V_{BC} is the base-collector bias.

The operation of the SVT is almost identical to the hot electron setups described before (see sections 2.2 and 2.3). Hot electrons are injected into the base over the first Schottky barrier, and their energy is determined by the barrier height (typically between 0.5 and 1 eV, depending on the metal/semiconductor combination). As the hot electrons move across the base, they are subjected to all the types of inelastic and

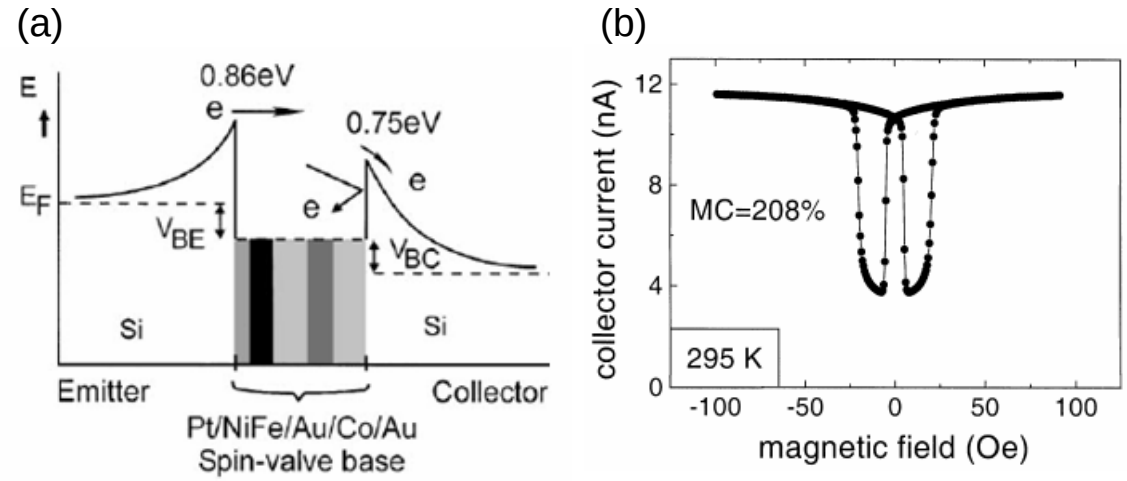

Figure 2.17: (a) Schematic energy band diagram of a Spin Valve Transistor (SVT), showing the semiconductor emitter (left) and collector (right), and the metallic base containing a spin-valve (middle). Also depicted is the flow of the injected electrons toward the collector (ballistic) and toward the base terminal (thermalized). (b) The magnetic field dependence of collector current of the SVT at room temperature and at low field showing a magnetic contrast of 208 %. I_E=2 mA and V_{BC}=0. Taken from [*Anil-Kumar et al.*, 2000].

elastic scattering discussed before (see subsection 2.3.2), which change their energy as well as their momentum distribution, affecting the fraction of electrons that are filtered at the second Schottky barrier.

The essential characteristic of the SVT operation, is the spin-dependent scattering effect while hot electrons cross the spin valve structure. As discussed before in this section, hot electron attenuation is spin-dependent in magnetic materials. A polarized electron beam is spin filtered when passing through a remanently magnetized metal film. In the SVT case, the first magnetic layer of the spin valve acts as the spin *"polarizer"*, while the second magnetic layer acts as the spin filter, or *"analyzer"*. In the case of parallel polarizer-analyzer alignment, there is low spin-dependent hot electron attenuation, whilst in the case of anti-parallel alignment the attenuation is considerably higher. The total spin-dependent scattering rate is controlled with an external applied magnetic field, which changes the relative magnetic alignment of the two ferromagnetic layers in the base. This "polarizer-analyzer" effect gives rise to an extra source of hot electron attenuation, that even when superimposed onto the spin independent attenuation mechanisms, leads to a detectable magnetic contrast in the collector signal.

In fig 2.17b, the magnetic field dependence of the SVT collector current at room temperature (295 K) is given. It is clearly seen that there is an hysteretic behavior, and that a large change in the collector current is obtained by a small change in the

magnetic field. The magnetic contrast (MC) is defined as

$$MC = \frac{I_C^P - I_C^{AP}}{I_C^{AP}} \tag{2.20}$$

where I_C^P and I_C^{AP} are the collector current in the parallel and anti-parallel magnetization alignment of the two magnetic layers, respectively. Thus, a MC in excess of 200 % is determined at room temperature. Although the transmission of the base layer is very low (usually $\leq$0.1%), the ability of injecting a current on the order of mA allows the detection of a ballistic signal on the μA range, much higher than the pA level signals involved in BEEM experiments. The huge MC at low field along with the easily detectable signal, make spin-dependent hot electron devices promising as commercial field sensors.

2.4.4 Spin hot-electron devices

The impact of the demonstration of the SVT was significant, and soon variations of the device where developed, namely the Magnetic Tunnel Transistor (MTT) [*Mizushima et al.*, 1998] and the Double Magnetic Tunnel Junctions (DMTJs) [*Colis et al.*, 2003]. In the latter, a structure with two stacked magnetic tunnel junctions is fabricated. In this way, the two Schottky potential barriers are substituted by two tunnel barriers, so that the first acts as the injector, and the second as the hot electron filter. The MTT is also making use of a tunnel barrier as an injector, but a Schottky barrier acts as a filter. Two slightly different versions of MTTs have been demonstrated, which will be now presented, since this tunnel-barrier-injector/Schottky-barrier-filter structure proves closest to a BEEM experiment.

The two MTT variations are depicted in figure 2.18. The design on the left, comprises a spin valve metal base deposited on a semiconductor, and separated from a non-magnetic metal emitter electrode by a thin insulating layer. When a voltage V_{EB} is applied across the tunnel barrier between emitter and base, unpolarized electrons are injected by tunneling into the metal base, arriving at an energy eV_{EB} above the Fermi level in the metal base. As in the SVT, the main operation features are spin-dependent transmission of the hot electrons through the two ferromagnetic thin films in the metal base, and collection across a Schottky barrier.

The design on the right of figure 2.18, has also a tunnel barrier, but uses a ferromagnetic emitter electrode. The structure is actually a Magnetic Tunnel Junction (MTJ) [*Moodera et al.*, 1995], elaborated on a semiconductor in such a way, that one of the electrodes is the MTT metal base layer. Because the tunnel probability is spin-dependent in a MTJ structure, the injected hot electrons are already spin polarized as they enter the transistor base. The spin polarized injected electrons are spin filtered in the base magnetic layer, and finally are collected across a Schottky barrier with energy and momentum selection.

A notable difference between the SVT and the MTT, is that when a tunnel barrier injector is used, the energy of the injected electrons is determined by the emitter-base

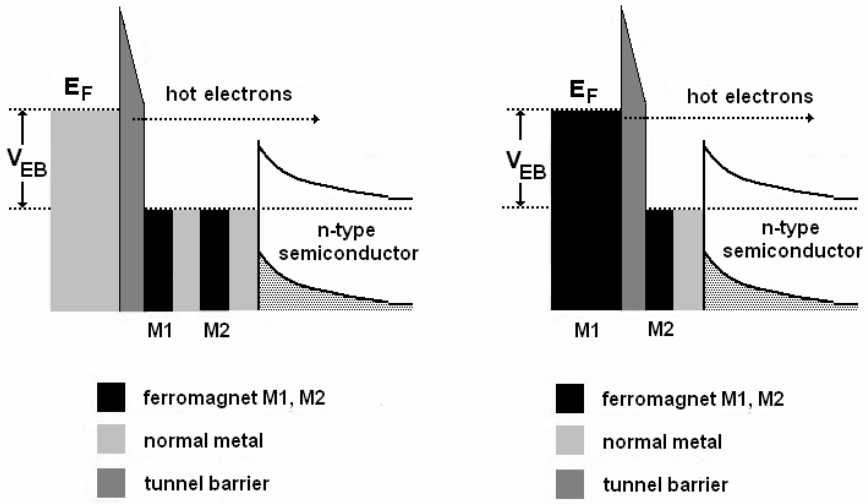

Figure 2.18: Schematic energy diagrams of the Magnetic Tunnel Transistor (MTT) with a non-magnetic tunnel injector (left) or a ferromagnetic tunnel injector (right) to generate the hot-electron current. Adapted from [*Jansen*, 2003].

voltage, V_{EB}, applied across the tunnel barrier. On the contrary, in the case of the SVT, the injection energy is fixed, and it is determined by the injector Schottky barrier height. As noticed before in the case of a BEEM experiment, the hot electron energy can be tuned in an energy range up to some eVs above the Fermi level, allowing spectroscopic studies. Raising the hot electron energy is also beneficial for the transmission of the device, since more electrons with energy higher than the Schottky barrier height are injected into the base [*Jansen*, 2003].

2.5 Ballistic electron magnetic imaging

High resolution magnetic imaging can be achieved by performing BEEM measurements in spin-valves. The concept of the MTT is transfered in a BEEM experiment, but the tunnel injector in this case is realized by the STM vacuum tunnel barrier. This way, the spin-dependent hot electron transport can be studied locally, with the lateral resolution of BEEM.

2.5.1 Principle of operation

The schematic of a BEEM experiment on a spin-valve, is shown in figure 2.19. As in any BEEM experiment, a beam of unpolarized electrons is injected into the metal base layer by the STM tip. Because of the polarizer-analyzer effect described before for the SVT and MTT cases, the collector signal is dependent on the magnetic configuration of the spin valve. By making use of the scanning capabilities of BEEM it is possible to

perform a "mapping" of the relative magnetization orientation of the two layers and create a magnetic image.

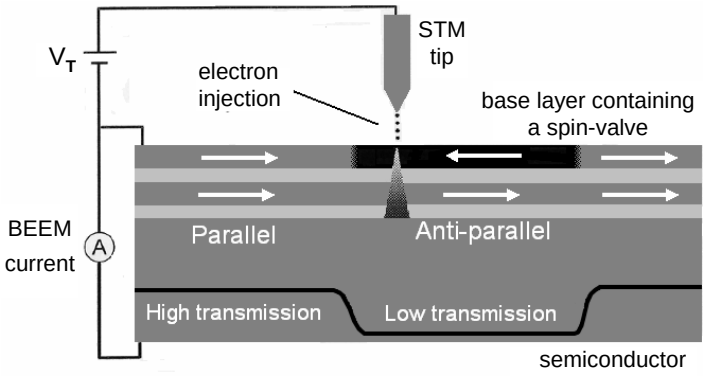

Figure 2.19: Schematic view of a BEEM experiment on a spin-valve. Taken from [*Haq*, 2005].

2.5.2 Experimental studies

The first BEEM study of a spin valve sample, consisted of BEEM spectroscopy measurements on Fe/Au/Fe multilayer [*Kinno et al.*, 1997], and was actually presented along with the first experiments on an MTT structure (see also [*Mizushima et al.*, 1998]). The clear dependence of the collector signal on the relative magnetization orientation of the two Fe layers was demonstrated by a collector signal-applied field hysteresis cycle (*BEEM hysteresis cycle*). However, imaging of magnetic structures was not achieved.

Imaging magnetic domains in spin valve structures using BEEM microscopy, was first achieved by Rippard and Buhrman [*Rippard and Buhrman*, 1999]. The term *"Ballistic Electron Magnetic Microscopy"* was then introduced. Performing magnetic imaging using BEEM, was a major advancement in the course of the technique. The original work did concern a study on Co/Cu/Co spin valves, elaborated on H-Si(111) substrates. Magnetic domains were imaged in a varying magnetic field, with a resolution of a few tens of nm. In another study, the magnetization reversal process of thin film NiFe nanostructures was imaged, by elaborating the nanostructures on a continuous Cu/Co bilayer, realizing this way "local" spin-valves [*Rippard et al.*, 2000]. The hot electron transport in Co/Cu/Co trilayer films was studied in the energy range from 1.0 to 2.0 eV, and the spin-dependent hot electron attenuation lengths in Co have been determined [*Rippard and Buhrman*, 2000].

BEEM magnetic imaging and hysteresis cycles were also performed on Co/Cu/NiFe spin valves grown on n-type GaAs substrates [*Heer et al.*, 2004]. A magnetic contrast on the order of 600 % at room temperature was achieved because of the use of thicker magnetic films (4.5 nm of Co and 3.5 nm of NiFe) that result in higher spin polarization

of the BEEM current (see section 6.2.1). The detection of the ultrasmall signal was made possible by using a highly sensitive electrometer capable of resolving currents down to the 20 fA level [*Heer et al.*, 1997]. In figure 2.20a BEEM spectra are shown in zero applied field (after saturation of the magnetic state) and in a field of 26 Oe applied along the opposite direction. In the first case the spin valve is in the parallel configuration, while in the second case the transmission is quenched, since the spin valve is in the anti-parallel configuration. Figure 2.20b shows a typical BEEM hysterisis cycle, where the spin valve is observed to be in the anti-parallel configuration in the field range between 20 and 40 Oe. The magnetic contrast amounts to 600%.

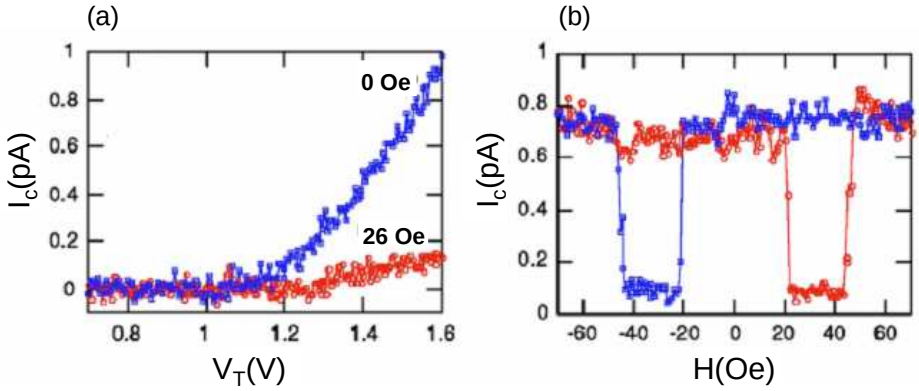

Figure 2.20: (a) BEEM spectra taken on a Co/Cu/NiFe spin valve in zero applied field (after saturation of the magnetization) and in a field of 26 Oe toward the opposite direction. I_T=20 nA (b) A BEEM hysteresis cycle. I_T=20 nA and V_T=1.5 V. Both measurements were in 300 K. Taken from [*Heer et al.*, 2004].

BEEM measurements have been performed on spin valve structures elaborated on a p-type semiconductor (*"Ballistic Hole Magnetic Microscopy"*) [*Banerjee et al.*, 2005b], as well . Figure 2.21, shows a series of magnetic images taken on a Co/Au/NiFe spin valve [*Haq et al.*, 2005]. The gray scale corresponds to the parallel (bright) and anti-parallel (dark) configurations of the spin valve. For 100 Oe applied field both magnetic layers are saturated and the signal is almost homogeneously bright, while by gradually increasing the field along the opposite direction anti-parallel aligned zones appear. The spin-dependent transport of hot holes in Co and NiFe thin films and Co/Au/NiFe spin valves was investigated in the energy range from 0.8 to 2.0 eV, and the spin-dependent hot hole attenuation lengths in Co were determined [*Banerjee et al.*, 2005b].

Recently, a BEEM study on $Fe_{34}Co_{66}$/Au/$Fe_{34}Co_{66}$ spin-valves epitaxially grown on a n-type $GaAs_{67}P_{33}$ substrate was presented [*Heindl et al.*, 2007a]. The lower defect density of the multilayer results in relatively higher BEEM current with respect to non-epitaxial samples. Moreover, the epitaxial $Fe_{34}Co_{66}$ layers exhibit in-plane anisotropy. BEEM hysteresis cycles were obtained as a function of the in-plane magnetic field angle, and they are compared to simulated BEEM cycles. Different magnetization configurations of the spin valve are available, due to the existence of equivalent easy axis

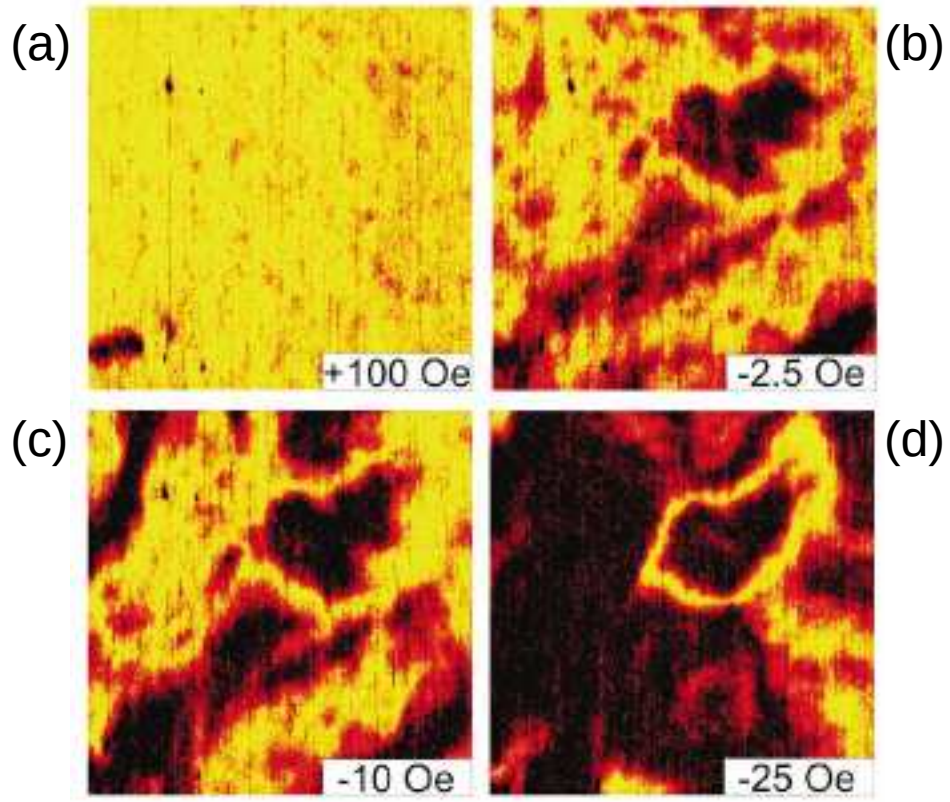

Figure 2.21: Ballistic Hole Magnetic Microscopy images taken on a Co/Au/NiFe spin valve in subsequent magnetic fields of (a) +100 Oe, (b) -2.5 Oe, (c) -10 Oe, and (d) -25 Oe. Scanning area 2×2 μm^2. Hole current ranges from 0.5 pA to 1.1 pA. V_T=1.6 V, I_T=3 nA, T=150 K. Taken from [*Haq et al.*, 2005].

directions, and the BEEM signal of these epitaxial spin valves depends on the applied magnetic field direction [*Heindl et al.*, 2007b]. Since different magnetization configurations of the spin valve are available, epitaxial spin valves allow multimagnetocurrent values, when the magnetic field is applied along different directions.

2.6 Conclusion

Hot electron transport studies can be categorized as macroscopic and microscopic or local. Macroscopic studies (hot electron devices), have the advantage of more flexible sample manipulation, giving easier access to experimental conditions such as low temperatures or high magnetic fields. Moreover, the ability of injecting large currents allows for the study of low transmission structures, while the resulting high signal-to-noise ratio, is an important figure of merit for technological applications. On the contrary, BEEM studies allow for nanometer scale microscopic studies of hot electron

transmission, which can lead to significant optimization of structures. In both macroscopic and local studies, an important parameter is the presence of a magnetic material. In this case, the electron spin has to be considered along with the electron energy and momentum.

In this thesis, our aim is to characterize the spin-dependent transport in ferromagnetic materials and use this effect to image the magnetic configuration of spin-valves. In the following, the development of the sample fabrication method is first presented (chapter 4). The hot electron transport in non-magnetic metal/Si structures is discussed in chapter 5. Finally, BEEM measurements of Co/Cu/Co and Co/Cu/Py spin-valves are presented in chapter 6. The energy dependence of the spin polarized attenuation length is discussed, and a quantitative study of the magnetic BEEM contrast is presented.

Chapter 3

Experimental equipment

In this chapter the main experimental infrastructure used during this thesis will be presented. First the thin film vacuum deposition systems are described. A STM-BEEM microscope housed in a separate vacuum chamber was utilized for hot electron transport and microscopy measurements. Various techniques for structural, electric and magnetic characterization of the samples were also used.

3.1 Vacuum deposition systems

Three independent vacuum chambers were used for thin film deposition. A high vacuum (HV) sputtering chamber, a HV resistive evaporation chamber, and an ultra-high vacuum (UHV) e-gun evaporation chamber [*Ohring*, 2002].

3.1.1 High vacuum sputtering system

A commercial (Plassys[1]) HV system was used for DC sputtering in the diode configuration (figure 3.1a). The chamber is pumped by a mechanical diaphragm pump and a turbomolecular pump, resulting in a base pressure $\approx 10^{-6}$ mbar. The carrier gas is Ar and the pressure during sputtering is maintained at 0.1 mbar. Two 50 mm targets are available. Both the substrate stage and target are kept at room temperature during deposition by a water-cooling system. The applied bias is ≈1-2 kV and the ion current ≈10-20 mA. The deposition rate was calibrated using stylus profilometry measurements, and may read a few tens nm/min. DC sputtering was used for Ohmic back-contact formation. The deposition area is comparable to the target size.

3.1.2 High vacuum resistive evaporation system

For resistive evaporation, another commercial (Plassys) HV system was used (figure 3.1b). This chamber is also pumped by a mechanical rotary pump and a turbo-

[1]Plassys-Bestek, http://www.plassys.com

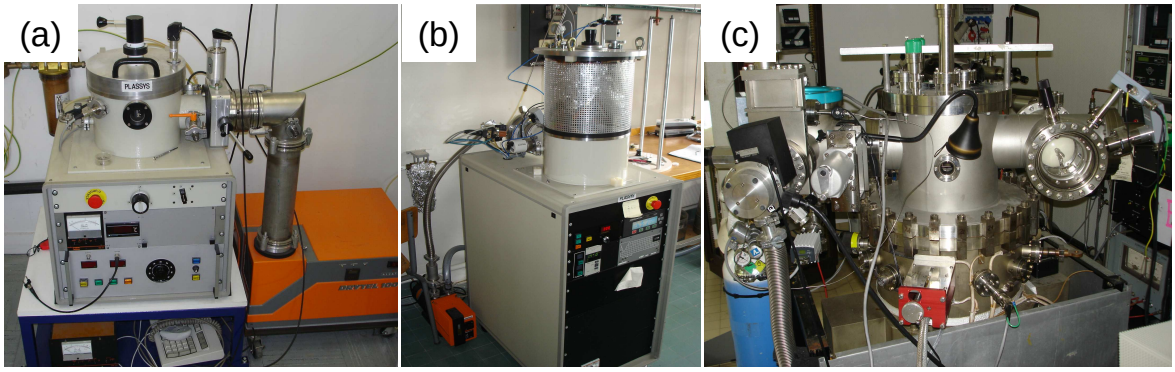

Figure 3.1: (a) DC sputtering HV system. (b) Resistive evaporation HV system. (c) E-gun evaporation UHV system.

molecular pump, resulting in a base pressure $\approx 10^{-7}$ mbar. Two positions are available for evaporation that can host tungsten wire sources, metal sheet sources, or sublimation furnaces. During this work, metal sheet tungsten boats were used. The boat is heated using currents typically 150-230 A. The deposition rate (up to a few tens nm/min) is monitored by a quartz crystal microbalance (QCM) system, calibrated against stylus profilometry measurements. Pressure during evaporation is $\approx 10^{-5}$ mbar. Resistive thermal evaporation was used to deposit the Au bonding pads. The evaporation area is limited by the chamber dimensions.

3.1.3 Ultrahigh vacuum e-gun evaporation systems

All the metallic multilayers studied in this work were deposited using e-gun evaporation. The UHV system used (figure 3.1c), comprises a load-lock chamber pumped by a mechanical rotary pump and a turbomolecular pump. The UHV evaporation chamber is pumped by an ion pump resulting in base pressure $\approx 10^{-10}$ mbar. A 5 source e-gun evaporation unit is used. At a given time a single material can be evaporated from a water-cooled Cu socket. The deposition rate is monitored using a QCM system, calibrated against X-ray reflection and atomic force microscopy measurements, and can reach a few Å/s. The pressure during evaporation is $10^{-9} - 10^{-8}$ mbar. The evaporation area is limited by the chamber dimensions.

A second UHV evaporation system was used for some preliminary depositions of multilayer samples, and for the fabrication of the Cu/Si(111) sample (see section 5.4). This is an e-beam evaporation system (Omicron triple EFM) housed in the UHV-2 chamber shown in figure 3.2. Three independent sources are available, which provide the ability of simultaneously depositing up to three different materials. The unit is water-cooled for minimum pressure rise during evaporation. Two molybdenum crucibles are used for Au and Cu evaporation. For Co deposition the material is sublimed from a rod. The deposition rate is monitored using a QCM system, calibrated against

X-ray reflection and atomic force microscopy measurements, and can reach 2 Å/min. The pressure during evaporation is below 2×10^{-10} mbar. In this case, the evaporant flux is confined by a metallic nozzle, and the evaporation area is $\approx$15 mm^2.

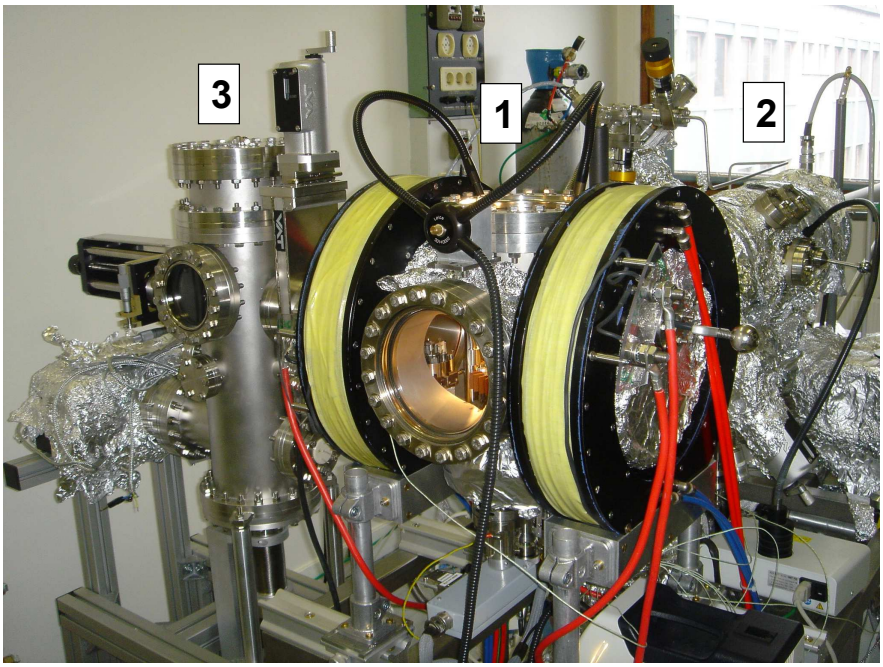

Figure 3.2: Global view of the STM experiment. The microscope is housed in chamber 1. The external coils providing the applied magnetic field are apparent. Chamber 2 houses an e-beam evaporator. A field emission setup for tip preparation is under development in chamber 3.

The advantage of the e-gun over the e-beam evaporator is the much higher deposition rate and the larger evaporation area. This allows for a quick multilayer sample batch fabrication. This way, structural, electrical and magnetic characterization can be performed on multilayers deposited simultaneously and side-by-side with BEEM samples. On the other hand, the e-beam evaporator provides much higher accuracy of the deposition rate, although it is limited to 2 Å/min. The major advantage, however, of the e-beam evaporation unit, is that it is coupled to the STM-BEEM chamber, providing the ability for *in-situ* transfer of the sample from the deposition chamber to the microscope.

3.2 STM-BEEM microscope

Transport and microscopy measurements were performed using a commercial room temperature STM (Omicron[2] STM-1), and "home-made" electrochemically etched

[2]Omicron Nanotechnology, http://www.omicron.de

tungsten STM tips.

3.2.1 Ultrahigh vacuum chambers

Figure 3.2 shows a global view of the STM experiment. All UHV chambers have base pressure $\approx 4\times10^{-11}$ mbar. A mechanical diaphragm pump and a turbomolecular pump are used for pump down. Static vacuum is preserved by an ion pump and a titanium sublimation pump, in order to avoid vibrations [*Harris*, 2005].

The microscope is housed in chamber 1. A pair of coils was attached to the chamber externally in order to provide the applied magnetic field. Roughly, a current of 1 A results in a field of 10 Oe at sample location. The maximum field value is limited by Joule heating of the coils and amounts to $\approx$ 100 Oe for continuous application and $\approx$ 200 Oe for application during a period of a few minutes. A wobble stick provides the ability of *in-situ* transferring the sample and the STM tip. Up to 13 samples and/or tips can be stored in UHV conditions.

Chamber 2 houses an e-beam evaporation system (see section 3.1.3), and an Ar ion gun. A field emission setup for tip preparation is under development in chamber 3.

3.2.2 Microscope

Figure 3.3a shows a global view of the microscope. The microscope stage and the four pillars housing the supporting springs are apparent. Magnetic damping is used as complementary anti-vibration system. In the foreground the Cu dampers are apparent, while the permanent magnets are just below, since for this photograph the microscope stage was locked in the "up" position. The flux-closure configuration of the magnets results in negligible parasitic magnetic field at sample position. In the middle of the image a sample bearing Omicron plate is shown and the top of an STM tip support is apparent in front of it. The tunnel current amplifier is also apparent.

Figure 3.3b shows a top view of the microscope. The cylindrical electronic component on the left is the tunnel current amplifier. The cubic piece on the middle is a ceramic stand, with a slot on the right side hosting the tip support. The three cylinders attached to the ceramic stand, are the piezoelectric elements comprising the tip positioning tripod. A tip is mounted on the stand, just in front of a sample. The Omicron sample holder is mounted on a carrier, resting on an inch-worm motor for rough approach of the sample. On the upper-right part of the image, the electronic component that can be only partially seen, is the BEEM current amplifier.

3.2.3 BEEM current detection

The tunnel current amplifier (Burr-Brown OPA602 operational amplifier used with a feedback resistance R=100 MΩ) is a current-to-voltage converter with a gain 10^8 V/A. It is placed *in-situ* very close to the sample ($\approx$2 cm) in order to reduce the electrical

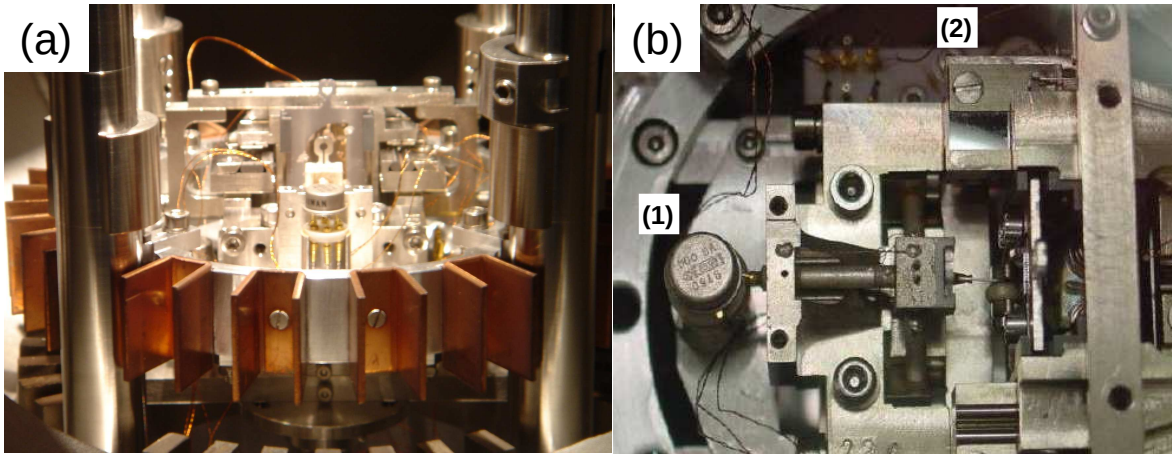

Figure 3.3: (a) Global view of the microscope showing the microscope stage and the four pillars housing the supporting springs. (b) View of the microscope "core". The STM tripod, the STM tip support and the sample plate are shown. The tunnel (1) and ballistic (2) current amplifiers are also apparent.

pick-up noise. For BEEM current measurement a supplementary amplifier is used, also placed *in-situ* very close to the sample. It is operating as an electrometer, capable of converting very low currents (a few pA) to a voltage measured. The gain of this amplifier is 9×10^7 V/A. For synthesizing a BEEM image the output voltage is digitized ($\pm$10 V). When dealing with very low currents, an additional 100 fold amplification is available. For more details about the electric scheme of the STM-BEEM microscope see [*Caud*, 2006].

Experiments are performed in the dark in order to avoid the illumination of the metal/semiconductor interface. The metal base has a typical thickness between 10 and 20 nm, comparable to the visual light penetration depth in metals. Thus, photons can excite electrons at the metal/semiconductor contact, which can contribute to the BEEM signal, with as a result a strongly perturbed signal.

3.2.4 STM tips

The STM tips were fabricated by electrochemical etching 0.38 mm diameter polycrystalline W wire. The end of the W wire along with the Pt counter electrode were immersed in a KOH solution (0.1 mol/l). The applied voltage was 18 V AC and the current of the order of a few tens of mA. Figure 3.4 shows scanning electron micrographs of the STM tips used at different scales. Using electrochemical etching, it is possible to obtain reproducibly tips with an apex curvature a few tens of nm.

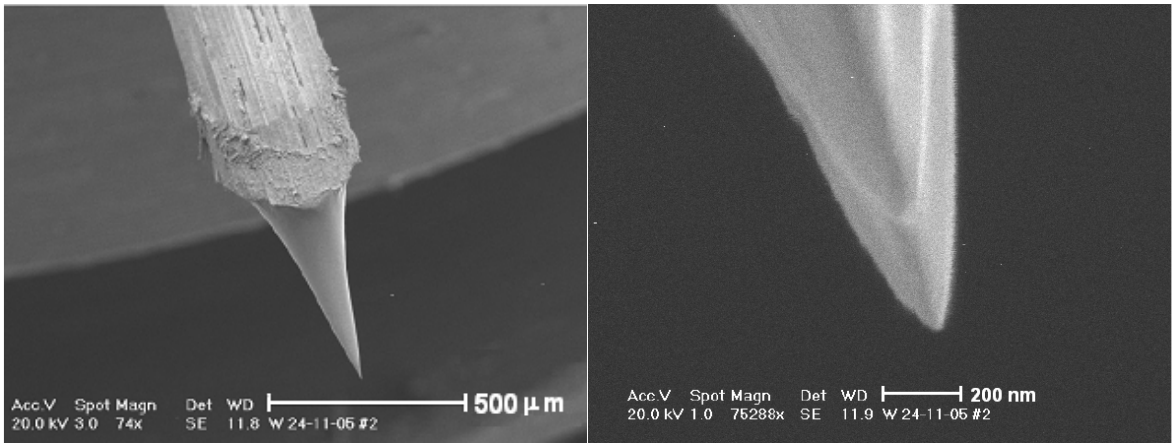

Figure 3.4: Scanning electron micrographs of the electrochemically etched STM tips used.

3.3 Characterization techniques

For structural characterization, besides STM measurements, Atomic Force Microscopy (AFM), Scanning Electron Microscopy (SEM), Transmission Electron Microscopy (TEM) and X-Ray Diffraction (XRD) measurements were performed. Scanning Electron Microscopy was used for the characterization of the surface structure and the elemental composition of the multilayers. A probe station was used for current-voltage (I-V) measurements. Magnetometry measurements were performed using the Magneto-Optical Kerr Effect (MOKE).

3.3.1 Structural characterization

Atomic Force Microscopy

Atomic Force Microscopy (AFM) is a Scanning Probe Microscopy technique in which a fine tip is brought into atomically close contact with a sample surface without actually touching the surface. This is done by sensing the repulsive force between the probe tip and the surface. The forces are extremely small (about 1 nN). The tip is then moved back and forth over the sample surface creating a topography map of the sample surface. Typical lateral resolution is a few nm, while the height resolution is a few Å. A Dimension 3100 AFM (Veeco[3]) was used during this work. The surface topography can be measured up to a lateral dimension of 110 μm.

[3]Veeco, http://www.veeco.com/

Scanning Electron Microscopy

Scanning Electron Microscopy (SEM) is a very widely used technique to study surface topography from macroscopic to nanometric scale. Typical resolution is ≈10 nm. Electrons emitted thermionically from a filament heated by a high current, are accelerated by a potential difference. Then, they form a high energy (typically 20 keV) electron beam, focalized by an electromagnetic lenses system and scanned across the sample surface. The incident electrons cause low energy secondary electrons to be generated, and some escape from the surface. The secondary electrons emitted from each point of the sample are collected, giving information about the surface structure.

The incident electrons will also cause X-rays to be generated, which is the basis of the Energy Dispersive X-ray Analysis (EDX) technique. The energy of the X-rays emitted depend on the material under examination. By moving the electron beam across the surface, information about the elemental composition of the multilayer can be acquired. The X-rays are generated in a region about 2 microns in depth, and thus EDX is not a surface sensitive technique. In our case, the main contribution to the EDX signal comes from the Si substrate. However, this does not prohibit detection of a metallic film a few nm thick.

Transmission Electron Microscopy

The transmission electron microscope (TEM) operates on the same basic principles as the light microscope but uses electrons instead of light. The spatial resolution of a light microscope is limited by the wavelength of light. TEM uses electrons as "light source" and their much lower wavelength makes it possible to get a resolution in the Å scale.

Electrons emitted from a source, are accelerated by a potential difference (typically 200 keV) and travel through vacuum in the column of the microscope. Instead of glass lenses focusing the light in the light microscope, the TEM uses electromagnetic lenses to focus the electrons into a very thin beam. The electron beam then travels through the specimen under study. Depending on the density and structure of the material present, some of the electrons are scattered and disappear from the beam. At the bottom of the microscope the unscattered electrons hit a fluorescent screen, which gives rise to a "shadow image" of the specimen with its different parts displayed in varied darkness according to their density.

X-ray diffraction and reflection

Wide angle X-ray diffraction (XRD) spectra were collected with a Phillips X'Pert diffractometer in $\theta - 2\theta$ scans, using Cu-$K\alpha$ radiation. XRD studies were performed for the determination of the crystalline structure of the films.

X-ray reflectivity measurements (XRR) were also performed using the same instrument. Film thicknesses, as well interface and surface roughnesses were determined by fitting the XRR measurements. The program used for this purpose was Parratt32.

3.3.2 Electric characterization

Macroscopic current-voltage measurements

The Schottky and ohmic metal/semiconductor junctions have been characterized by 4-point probe measurements. Micromanipulated probes (Signatone S725) are used as contacts. A precision multimeter (Agilent 3458A) and a current/voltage source (Keithley 2400) are used for measurement purposes. The setup is controlled by a Labview program. The voltage is measured while the current is sweeped, reducing the current step if the voltage across the junction is too high, in order to follow a diode-like curve. The measurement bench (figure 3.5) is installed on a marble table, isolated from external vibrations by a compressed air suspension. The Schottky diodes were measured in the dark since they are extremely photosensitive.

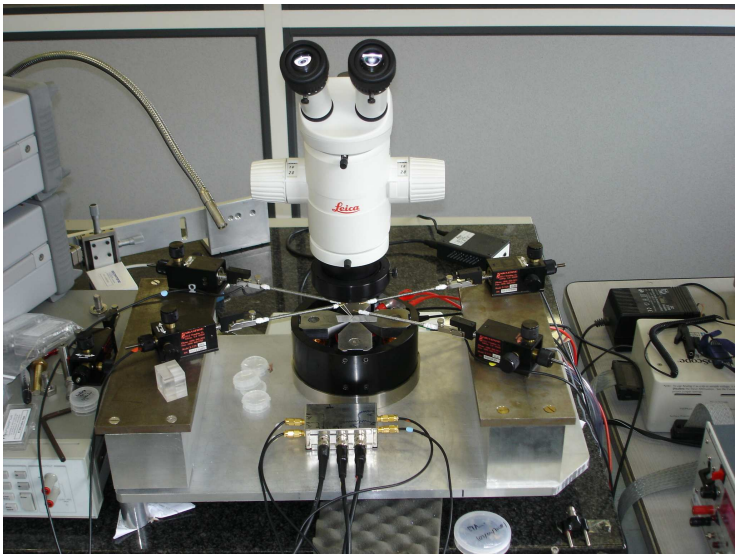

Figure 3.5: Current-voltage measurements bench. The micromanipulated probes, the coils providing the magnetic field and the binoculars for sample positioning are apparent.

Giant Magneto-Resistance measurements

Current-In-Plane (CIP) GMR measurements have been performed using the same bench as in figure 3.5. The subtle resistance differences observed (a few mΩ variation with field, for a resistance of some Ω), are measured by means of lock-in detection (lock-in amplifier model: Princeton Applied Research 5210). Moreover, the measured resistance is sensitive to the distance between the probes. Thus, thermal or mechanical drift of the micromanipulated probes can lead to resistance variations. To resolve this problem, a probe head was used for GMR measurements, were the four probes are fixed at a 1 mm separation between them. The applied field is provided by two pairs of coils

in quadrupole configuration. The maximum field that can be applied is ≈1 kOe. Any in-plane direction is accessible.

3.3.3 Magnetic characterization

Magneto-Optical Kerr Effect measurements

The Kerr effect is the rotation of the polarization axis of light, or the variation of the ellipticity of light, during the reflection of light on the surface of a magnetic material. The measurements were performed at room temperature using the longitudinal configuration. In this case, the magnetization vector is parallel to both the reflection surface and the plane of incidence, and the light is reflected at an angle from the reflection surface. A green HeNe laser was used (λ=532 nm), with a beam diameter ≈1 mm^2.

Chapter 4

Development of the sample fabrication process

4.1 Introduction

The development of a BEEM sample fabrication method, constitutes the first half of the experimental work undertaken in the framework of this thesis. The extremely low level of the BEEM signal (pA range), makes the development of a sample fabrication process highly demanding, with respect to experiment design, materials selection, techniques used and process sequences. In this chapter, BEEM sample fabrication requirements are first discussed, and the sample design that allows BEEM experiments to be performed is described. Next a method for preparing hydrogenated Si(111) substrates with ohmic back contact is presented. The fabrication of the indispensable Au/Si(111) Schottky diodes and the magnetic multilayer BEEM samples is discussed. The sample fabrication process is described in detail in the last section.

4.2 Sample considerations

BEEM experiments are performed using an STM, with the additional requirements of contacting the semiconductor and the metal film separately. The back side of the semiconductor substrate is treated in order to have an ohmic contact (*back-contact*), and the metal film is grounded by an additional wire contact, the so-called *front-contact*. Hot electrons that thermalize into the metal base, are collected by the front-contact. Ballistic electrons are energy filtered at the metal/semiconductor interface (*Schottky contact*), and after thermalizing in the semiconductor, are collected by the back-contact.

4.2.1 Schottky contact

As shown in section 2.3.1, the ability to detect pA level signals is essential for performing BEEM experiments. The noise level of the measurement, defining the minimum current that can be detected, is determined by the Schottky contact.

BEEM current noise

The main source of BEEM current noise, results from the thermal agitation of electrons in the metal/semiconductor structure, that gives rise to a random fluctuation of the voltage across the Schottky contact, known as *Johnson noise*. This thermal noise in voltage V, across a resistance R, at a temperature T, is given by

$$\Delta V = \sqrt{4k_B TBR} \tag{4.1}$$

where B is the bandwidth of the measurement and k_B is the Boltzmann constant, while ΔV is the r.m.s. value of the signal. In terms of current noise, equation 4.1 can be written as

$$\Delta I = \sqrt{\frac{4k_B TB}{R}} \tag{4.2}$$

where, in our case, R can be the sample resistance or the resistance of the operational amplifier. While the latter is considerably high ($\approx 10^8$ Ω) and the added effect negligible, this is not the case for the sample resistance. For the acquisition of a BEEM image with scanning frequency 1 Hz and 400 points in each scanning direction, the bandwidth is B=800 Hz. At room temperature and for a sample resistance R=1 MΩ, a non-negligible value on the order of 3 pA is calculated for ΔI. However, during this work BEEM samples with R from 1 to 15 MΩ where fabricated, while the scanning frequency was often as low as 0.1 Hz (B=80 Hz), resulting in lower noise. The Johnson noise can be even lower during spectroscopy measurements. In this case, the data acquisition time per measurement point can be up to 0.1 s leading to a B=10 Hz bandwidth.

Sample resistance

Since R defines the noise level of the BEEM current measurement, it is necessary to determine it before performing a BEEM experiment. The current I traversing the Schottky barrier, according to the thermionic emission model, is given by equation 2.2. In the case of a BEEM experiment, where the Schottky contact is not polarized, we are interested in the zero voltage resistance of the diode (*zero voltage sample resistance,* R_0), which is given by the derivative of equation 2.2

$$R_0 = \left(\left. \frac{dI}{dV} \right|_{V=0} \right)^{-1} = \frac{h^3}{4\pi m^* e^2 k_B} \, \frac{1}{TA} \, \exp(\Phi_B / k_B T) \tag{4.3}$$

Here, A is the area of the junction, m^* is the effective mass at the conduction band minimum of the semiconductor, Φ_B is the Schottky barrier height, V the voltage applied to the junction and T the temperature.

In our case, a Au/Si(n-type) diode, with $\Phi_B = 0.8\ eV$ [*Sze*, 1981], $T = 300$ K, $m^* = 0.19\ m$, where m is the mass of the free electron and a contact area $A \approx 0.45$ mm^2 yields a value $R_0 = 1.7$ MΩ, which is sufficiently high to perform BEEM measurements. Leakage currents at the edges of the metal film, result in a resistance in parallel ($R_\parallel$) with the Schottky contact resistance. In this case the sample resistance becomes

$$R = \frac{R_0 R_\parallel}{R_0 + R_\parallel} \tag{4.4}$$

Typically $R_\parallel$ values are of the order of several MΩ (see section 4.5). However, R can be significantly reduced by a much lower $R_\parallel$ value.

The above example shows that BEEM investigations at room temperature are limited to junctions with barrier heights exceeding 0.8 eV. A Schottky barrier height slightly reduced to 0.75 eV, would result to a 7 times smaller R_0, making impossible the detection of the pA level ballistic signal due to the elevated Johnson noise (see equation 4.2). In the case of lower barrier heights, lower temperatures and/or smaller diode areas are required. In section 5.4, a simple method is described for fabricating diodes with much smaller area by making use of mechanical shadow-masks.

4.2.2 Semiconductor substrate

The necessity of growing the metal film on a sufficiently flat semiconductor substrate will now be addressed. An important requirement for a BEEM experiment, is that the whole of the metal film should be grounded. An attempt of performing BEEM on a non-grounded zone, would lead to charging of the metal layer, since it will not be possible to evacuate the thermalized electrons. This implies the growth of a continuous film, free of patches or clusters that are not in good contact with each other.

A minimum layer thickness is required for the growth of a continuous film, depending on substrate and deposited material parameters. However, the metal layer should not be too thick, since inelastic scattering of the hot electrons reduces the current reaching the interface. While the mean-free path of electrons about 1 eV above the Fermi level is a few tens of nm for noble metals, it is one order of magnitude lower for $3d$ transition metals (see section 2.3.1). In this case, lower film thicknesses should be used. From the discussion above, it is clear that film continuity and permitted film thickness are competitive factors, implying excellent substrate flatness, and the ability of growing ultra thin metal films.

4.2.3 Ohmic back-contact

Another constraint for the sample is imposed by the back contact, which should have an ohmic behavior. In figure 4.1, the energy diagram of the sample is schematically

shown, together with a corresponding electrical circuit of the BEEM experiment. The metal/semiconductor interface to be studied is characterized by R and C, and the back contact by R_b and C_b. In the electric-circuit representation, the incoming BEEM current I_B^* feeds into the semiconductor (between the contacts), and may flow to ground either via the Schottky metal/semiconductor contact (R) or via the back contact (R_b). Since only those electrons flowing through the back contact will be detected as ballistic signal, the condition for a correct measurement of I_B is that $R_b \ll R$, otherwise the BEEM current is reduced and can even become undetectable.

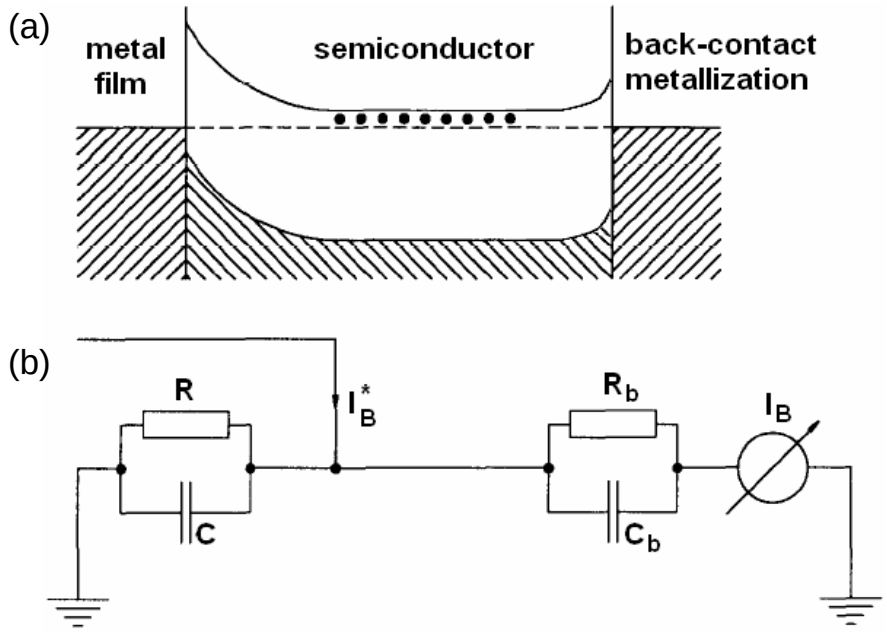

Figure 4.1: (a) Energy diagram of a sample used for BEEM experiments, and (b) corresponding electric-circuit diagram. Taken from [*Prietsch*, 1995].

A metal/semiconductor contact with ohmic behavior, is usually implemented by fabricating a Schottky contact with low barrier height, and/or narrow space charge region (for discussion on the Schottky contact see section 2.3.1). By decreasing the Schottky barrier height the thermionic emission current is increased, thus reducing the contact resistance (see equation 4.3). As the Schottky barrier height depends on the choice of materials, the appropriate metal should be deposited for back-contact formation. The thermionic emission current increase is further enhanced by fabricating a contact with large area. In the case of a narrow space charge region, electrons tunnel through the potential barrier reducing the contact resistance. However, in this case the contact resistance is not described by equation 4.3, since the thermionic emission model is no longer valid [*Sze*, 1981]. As the space charge region is inversely proportional to the square root of the semiconductor dopant concentration (see equation 2.1), a local treatment of the semiconductor to increase the doping may be performed prior to metal

deposition.

4.3 Sample design

In this section, the choices that have been made during this work concerning the materials used and sample design, are discussed. The sample holder design is also described.

4.3.1 Sample choices

The most important choices to be made when designing a BEEM sample fabrication process, is the semiconductor substrate and the Schottky contact to be used.

Semiconductor substrate

The substrate of choice throughout this work was n-type Si(111). The (111) orientation provides the ability to prepare sufficiently flat surfaces using chemical etching (see section 4.4). The n-type is chosen because Schottky contacts with higher barrier energies can be formed [*Sze*, 1981]. The dopant concentration should be low enough in order to avoid a narrow space charge region of the Schottky contact, that would cause electrons to tunnel through the barrier. On the contrary, the dopant concentration should be sufficiently high for ohmic contact formation (see section 4.2.3). A medium doping concentration of 10^{15} atoms/cm^3 was chosen to fulfill both requirements.

Schottky contact: The deposited metal

The first criterion for choosing the metal to be used for Schottky contact formation, is the contact barrier height. From this point of view, a suitable choice for Schottky contact formation with n-type Si is Au. Au forms an abrupt interface with Si(111), with no reaction between Au and Si atoms at the interface (see section 4.5). The Schottky barrier height is sufficiently high to perform BEEM measurements at room temperature (see section 4.2).

The fabrication of metal/Si(n-type) Schottky contacts with higher barrier height, is as well possible using Pt as the metal layer ($\Phi_B = 0.9\ eV$ [*Sze*, 1981]). Moreover, the formation of a Pt silicide layer, would result in a silicide/Si Schottky barrier height equal to $\Phi_B = 0.85\ eV$, which is still sufficiently high [*Niedermann et al.*, 1993]. However, electron-electron scattering in Pt is much more intense than in Au (because of band structure reasons, as discussed in section 2.3.2), resulting in a shorter hot electron attenuation length.

As discussed in section 4.2, the barrier height of the Schottky contact to be used defines the maximum contact area according to equation 4.3. For the Au/Si(n-type) Schottky barrier, a maximum contact area $\approx$0.5 mm^2 is determined. On the contrary,

the diode area should be sufficiently large in order to facilitate STM tip positioning. The choice of a 0.5 mm^2 diode is a compromise between the two competitive necessities.

Schottky contact: Fabrication method

A first choice for fabricating small area diodes would be to use standard microfabrication techniques. However, in the past this method resulted in low quality Schottky diodes [*Caud*, 2006; *Thiaville et al.*, 2007], most probably because of the improper surface preparation of the substrate. Moreover, the contact area chosen, is in a scale accessible with mechanical masks. Thus, a Cu foil shadow-mask was used for diode fabrication.

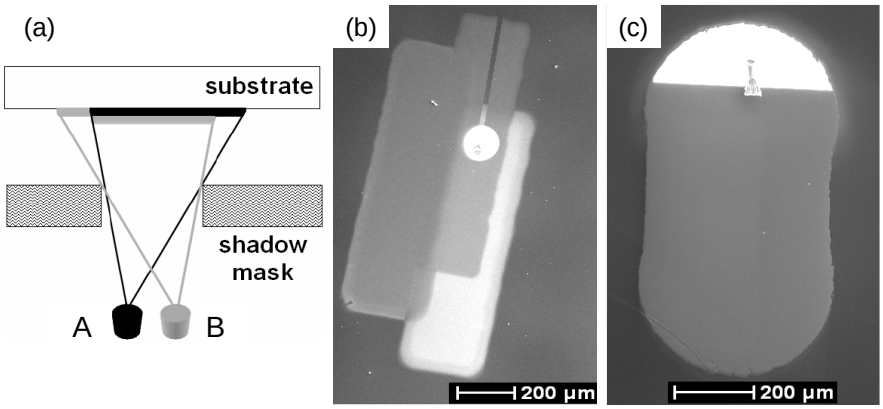

Figure 4.2: (a) Schematic drawing (not to scale) explaining the misalignment occurring when two materials are shadow-mask deposited from sources "A" and "B". (b) SEM micrograph of a metallic trilayer deposited using the *in-situ* transferable mask (the substrate-mask separation is ≈1 mm). The three bands correspond to Au, Cu and Co. (c) SEM micrograph of a metallic trilayer deposited using a mask attached on the substrate (the substrate-mask separation is 10-20 μm).

Initially, the multilayers were deposited using the UHV e-beam evaporator (see section 3.1.3) and an *in-situ* transferable shadow-mask. The separation between the substrate surface and the mask is ≈1 mm. In this evaporator the different materials are deposited from three different sources. The distance between the sources is 1 cm. This deposition geometry results in a misalignment of the deposited layers (see figure 4.2a). The extent of the misalignment depends on the substrate-mask separation and the distance between the evaporator source and the mask. Since the latter is a fixed value depending on the deposition system, only the former can be adjusted. Multilayer deposition using the transferable mask, results in enormous misalignment of the different layers, because of the extremely high substrate-mask separation. Figure 4.2b, shows a Au/Cu/Co trilayer deposited using this method. It is obvious that the three layers are displaced by such an extent, that only partial overlap is achieved.

In order to resolve this problem, the substrate-mask separation has to be dramatically reduced. For this purpose, a deposition sample holder was developed, that allows a Cu-foil shadow-mask to be mechanically attached on the substrate surface. This way, the substrate-mask separation is limited to 10-20 μm. A Au/Cu/Co trilayer deposited this way, is shown in figure 4.2c. The three layers are only slightly misaligned, and at that magnification, cannot be distinguished from each other (higher magnification imaging reveals a 1-2 μm misalignment, see section 5.4). During this work, all the multilayers studied by BEEM were fabricated using this method.

In principle, the deposited layer misalignment that occurs using mechanical masks is considered a drawback. However, in section 5.4 it is shown that it can become an asset permitting the measurement of the Cu/Si(n-type) Schottky barrier at room temperature. It should be noted that all the multilayers studied hereafter were fabricated using the e-gun evaporator (see section 3.1.3). The above discussion applies as well to this case, since due to the evaporator design considerable error in the positioning of each source may occur.

Sample configuration

A schematic drawing of the BEEM sample configuration we used may be seen in figure 4.3. A multilayer with total thickness 10-20 nm is grown on top of the Si chip through the Cu foil mask. The first deposition step is the fabrication of the Au/Si(111) diode. Then, the rest of the multilayer is deposited. Accordingly, a rounded rectangu-

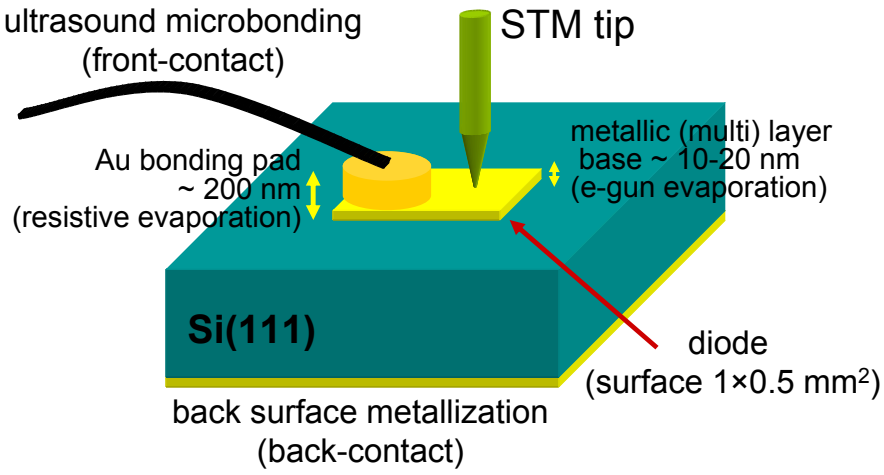

Figure 4.3: Schematic drawing of a BEEM sample. The base (multi)layer to be investigated is apparent as a rectangular region on top of the silicon chip. The STM tip along with the front- and the back-contact are the three terminals of the device.

lar $1 \times 0.5\ mm^2$ structure is formed. A second shadow-mask is added, in order to define a 200 nm thick Au bonding pad in direct electric contact with the upper part of the metal base. The front-contact is realized by means of ultrasound microbonding, thus

grounding the metal base and allowing for the evacuation of the thermalized electrons. The back side of the chip is treated to have an ohmic back-contact for collection of the BEEM current. An SEM micrograph of a multilayer stack is shown in figure 4.2c. The brighter part on top of the structure is the much thicker Au bonding pad. A remaining part of the wire used for microbonding is also apparent.

4.3.2 BEEM sample holder

For *in-situ* manipulations, an appropriate sample holder should be used, that would allow the implementation of the three terminal sample configuration. Although strictly this is an instrumentation issue, the close connection between the design of the sample and the sample holder, leads to a necessary description of the latter with this section.

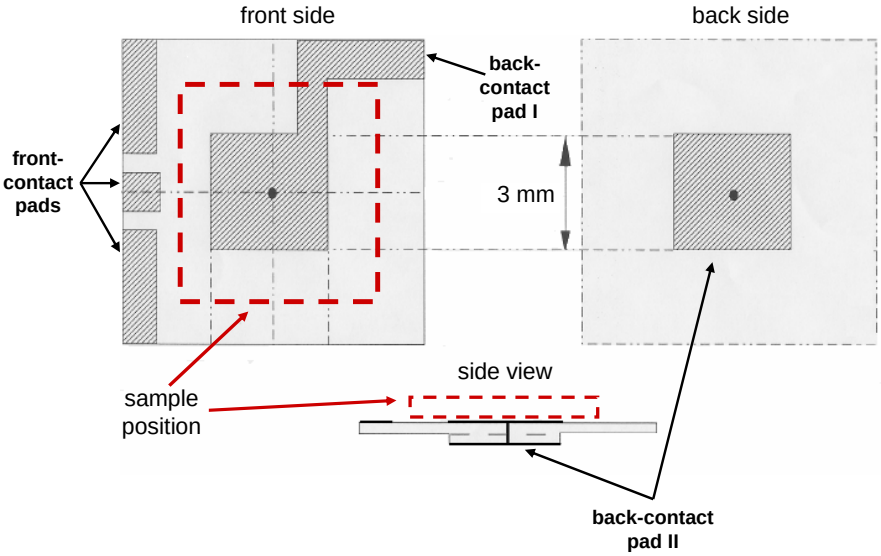

Figure 4.4: Schematic drawing of the ceramic plate serving as sample support for mounting the sample on the sample holder. The hatched areas indicate metallized zones. The black spot apparent at the center indicates the metalized hole that runs across the ceramic plate and electrically connects back-contact pads I and II.

In order to mount the sample on the sample holder, a sample support is used. This is a piece of ceramic plate, where 10 μm thick Au electric pads are deposited on the front and back sides (figure 4.4) [*Caud*, 2006]. The BEEM sample is placed on the front side of the support, so that the sample back-contact is in direct electric contact with the back-contact pad I. The back-contact pad I is electrically connected with the back-contact pad II, via a metalized hole which runs across the ceramic plate. The microscope back-contact electrode is brought into contact with the back-contact pad II for BEEM current measurements. The front-contact pads are electrically connected with the front-contact of the BEEM sample by means of ultrasound microbonding. A 25 μm thick Al/Si(1:4) wire is used for this purpose.

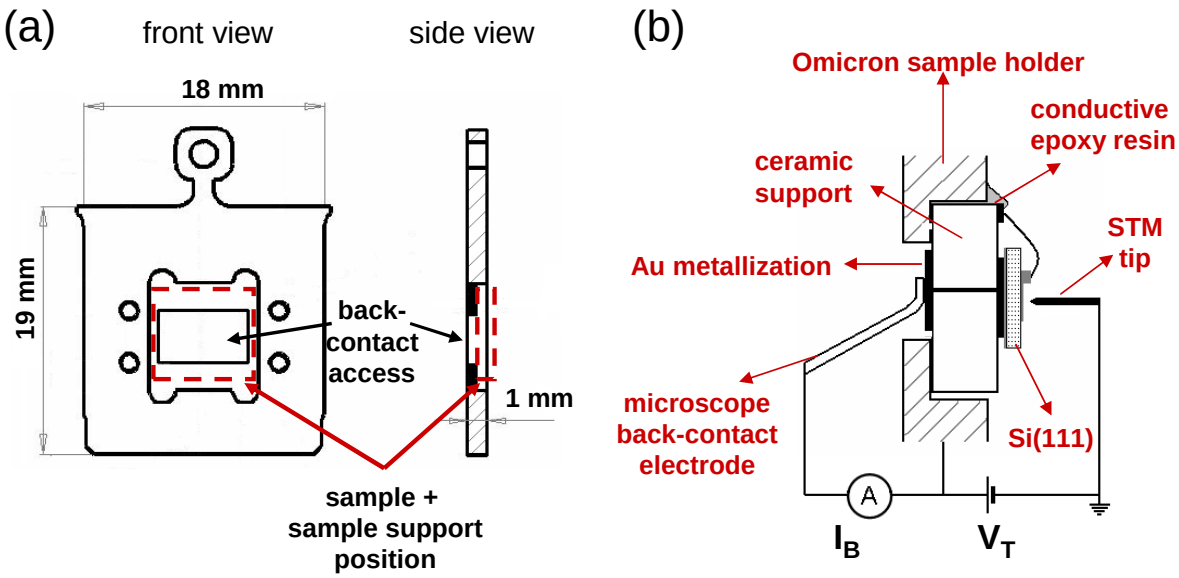

Figure 4.5: (a) Schematic drawing of the modified Omicron sample holder used. The cavity hosting the sample support is apparent. A window is opened to allow the electrical connection of the microscope's back-contact electrode to the sample back-contact. (b) Electric configuration of a BEEM sample mounted on the microscope (not to scale).

A modified Omicron sample holder is used (figure 4.5a) [*Caud*, 2006]. A cavity was created by mechanical grinding in order to host the support. Since the support is ceramic, the Au pads are electrically insulated from the steel holder. A rectangular window is opened in the middle of the holder, allowing the microscope back-contact electrode to have access to the back-contact pad II of the support. This way, the direct electric contact between the sample back-contact and the microscope back-contact electrode is realized. The sample is mechanically fixed on the holder via stainless steel clamps screwed in the tapped four holes. The clamps need to be electrically isolated from the Si chip, in order to avoid a short-circuit between the front and back contacts. A UHV compatible electrically insulating epoxy (epo-tek H74[1]) is applied for this purpose along the edges of the clamps.

Figure 4.5b schematically shows the electrical configuration of a BEEM sample mounted on the microscope. The front-contact pads of the support are electrically connected to the sample holder by means of a UHV compatible electrically conductive epoxy (epo-tek H21D), allowing the application of the tunnel gap bias to the metal base. Besides electrical connection, the epoxy is also used to mechanically fix the support on the holder.

A photograph of a Au/Si(111) BEEM sample mounted on a sample holder can be

[1]Epoxy Technology, http://www.epotek.com

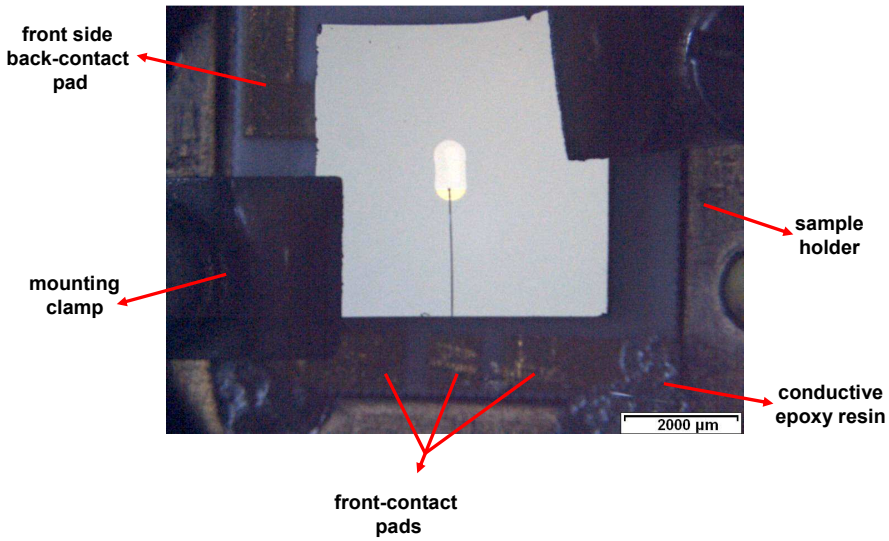

Figure 4.6: Optical photograph of a BEEM sample mounted on a sample holder. The rounded rectangular BEEM structure on the silicon chip is apparent.

seen in figure 4.6. The rounded rectangular structure at the middle corresponds to the Au thin film, while the brighter area at the bottom of the rectangular structure is the much thicker Au electric pad. The grounding wire is apparent as a dark line, connecting the Au electric pad, with one of the front-contact pads of the support.

4.4 Hydrogenated Si(111) substrates with ohmic back-contact

A method for preparing atomically flat hydrogenated Si(111) [H-Si(111)] substrates with ohmic back contact, was elaborated during this thesis. The basic principles of the method are discussed in this section, while the detailed "recipe" is described in section 4.7.

4.4.1 The hydrogenated Si(111) surface

Surface preparation

The H-Si(111) surface was prepared at room temperature by means of wet chemical etching [*Higashi et al.*, 1990; *Higashi et al.*, 1991]. First a buffered oxide etch (BOE) solution is used to remove the ≈1.5 nm thick native surface oxide. While BOE etches SiO_2 in a rate of several tens of nm per minute, bulk silicon remains practically intact and only small scale Si adstructures are removed [*Jakob and Chabal*, 1991]. Thus, BOE etching exposes the initial Si/SiO_2 interface. Although the surface Si atoms are

hydrogen passivated [*Trucks et al.*, 1990], the surface structure corresponds to the isotropically rough, mechanically polished front side of the wafer. Figure 4.7a, shows a substrate treated only with BOE solution, revealing the rough surface microstructure.

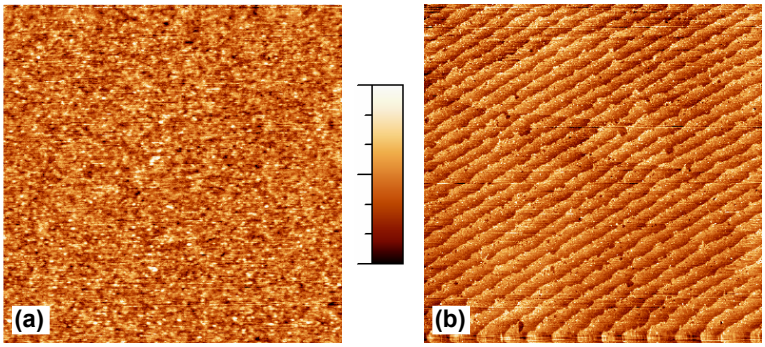

Figure 4.7: AFM imaging performed on Si(111) substrates. (a) The mechanically polished Si surface after BOE etching. Scan size 1×1 μm^2, scale bar from 0 to 1.50 nm, RMS roughness 0.25 nm. (b) The vicinal Si(111) surface after BOE and NH_4F etching. Atomically flat (111) terraces are separated by atomic bilayer steps. Scan size 4×4 μm^2, scale bar from 0 to 1.10 nm, RMS roughness 0.17 nm

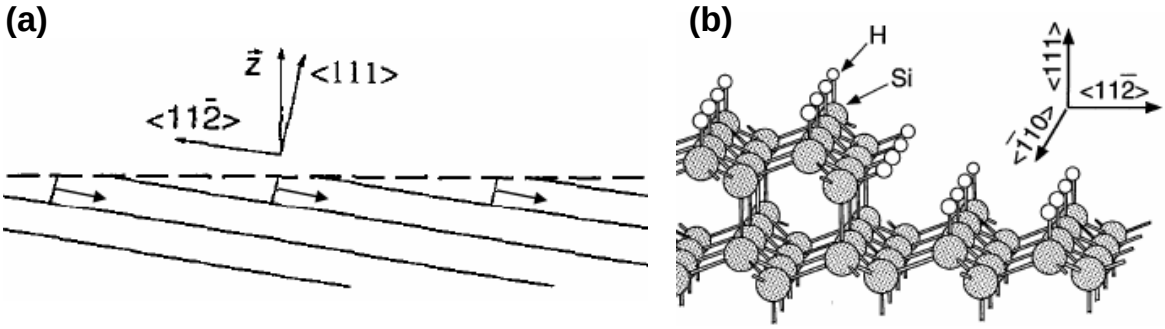

Figure 4.8: (a) Schematic representation of the "step flow" mechanism. Arrows indicate the etching direction of the (111) planes. Taken from [*Jakob and Chabal*, 1991].(b) Schematic representation of the H-Si(111) surface indicating atomic bilayer high steps separating (111) terraces. Taken from [*Dumas et al.*, 1992].

After the first etching step, the substrates are rinsed in deionized (DI) water. Since aqueous environment enhances oxidation of the surface, DI water is sparged with dry N_2 for at least 30 min before use, in order to reduce dissolved oxygen. A second etching step follows, using NH_4F solution. NH_4F etches bulk Si anisotropically, with an etching rate of the (100) planes, roughly 10 times higher than that of the (111) planes. This results in a "step flow" mechanism that "planarizes" the surface [*Jakob and Chabal*, 1991; *Dumas et al.*, 1992]. The resulting surface, is the vicinal Si(111) surface, with

atomically flat (111) terraces separated by atomic bilayer steps. The width of the terraces depends on the wafer miscut. To show the above, AFM imaging has been performed on such a surface (figure 4.7b). The terrace width in this case, is measured to be ≈90 nm, with typical values in the 50-200 nm range.

In figure 4.8, a schematic representation of the "step flow" mechanism and the strucure of the H-Si(111) surface are shown. NH_4F attacks Si at the step edges resulting in the continuous exposure of (111) planes (a). No surface reconstruction appears, since all dangling bonds of the surface Si atoms are hydrogen passivated, with monohydrides terminating the (111) planes (b). A final DI water (N_2 sparged) rinsing step is applied in order to remove any remaining chemical species from the surface.

STM characterization

STM images reveal in more detail the structure of the H-Si(111) surface (figure 4.9). Terraces with an average width ≈80 nm, are separated by ≈0.52 nm high atomic bilayer steps, with edges along the $<\bar{1}10>$ direction. Besides silicon etching at the step edges, triangular etch pits are present in the (111) planes.

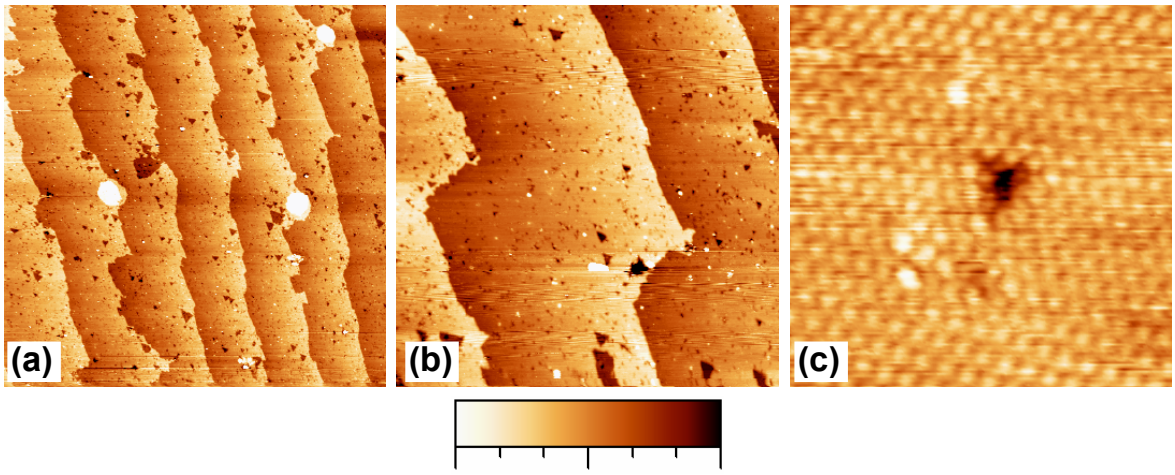

Figure 4.9: STM images of the vicinal Si(111) surface (a) Scan size 500×500 nm^2, scale bar from 0 to 1.40 nm. (b) Scan size 200×200 nm^2, scale bar from 0 to 1.00 nm. (c) Atomic resolution image on a single terrace indicating the close packed structure of the (111) planes. Scan size 6.5×6.5 nm^2, scale bar from 0 to 0.24 nm. Constant current images: I_T=1 nA and V_T=1.6 V

In figure 4.9c, an atomic resolution image on a terrace is shown, where the hexagonal array of the non-reconstructed Si(111) surface is clearly observed. The Si atom spacing is measured to be 0.38 nm, in good agreement with the expected Si lattice constant. The surface corrugation (peak to peak) is measured to be 0.07 nm. The protrusions apparent as bright spots, are most probably physisorbed species. The extent of this kind of contamination is low, as deduced from the image; however, it is inherent to the

preparation process, since the surface is prepared in ambient air before introduction in UHV conditions.

The missing atoms in the middle of the image indicate a triangular etch pit shortly after nucleation. It has been shown that the nucleation of those etch pits is initiated by the presence of dissolved oxygen in the etching solution [*Wade and Chidsey*, 1997], resulting in less regular surfaces. In order to avoid as much as possible this effect, the NH_4F solution is also sparged with dry N_2 at least for 30 min before use, reducing the oxygen content

Oxidation in ambient air

The H-Si surface exhibits a remarkably high durability against oxidation in ambient air conditions. An X-ray photoelectron spectroscopy (XPS) study of HF-treated Si(100) surfaces, reveals that the development of an oxygen coverage during subsequent storage in air occurs extremely slowly. Oxygen coverage equivalent to one monolayer, is reached after 7 days of storage in ambient air, at room temperature. After half a year, the SiO_2 thickness is about 0.8 nm [*Gräf et al.*, 1990]. In another XPS study of the hydrogen passivated Si(100) surface, the onset of oxidation (within the detection limit of XPS) is observed after 40 hrs of exposure in ambient air. Finally, STM imaging reveals that after 15 min of contact with atmospheric conditions, the Si(100)-2×1:H surface remains atomically pristine [*Hersam et al.*, 2001].

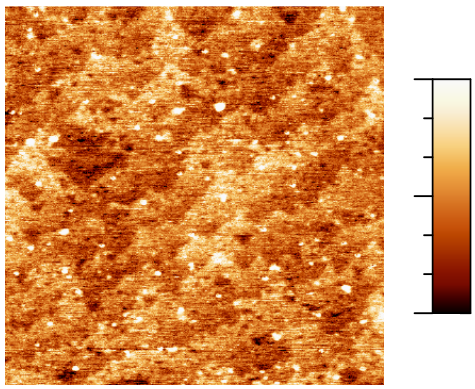

Figure 4.10: AFM image of a H-Si(111) surface after 5 days of exposure to ambient air. The initial stepped surface can still be resolved. Scan size 1×1 μm^2, scale bar from 0 to 0.92 nm, RMS roughness 0.17 nm

We have performed AFM imaging to characterize H-Si(111) surfaces after storage in ambient air, at room temperature. In figure 4.10, a substrate is shown 5 days after exposure to ambient air, where the initial stepped structure can be clearly resolved. The growth of a native oxide would have resulted in the absence of steps on the surface. Thus, the very slow oxidation rate of the H-Si(111) surface is confirmed.

Surface preparation is taking place *ex-situ* and after a few minutes the substrate is introduced in UHV conditions. We consider that in this time interval the surface is practically inert, so that the thin films are actually grown on the H-Si(111) surface and not on a native oxide layer.

4.4.2 Ohmic back-contact

A Schottky contact with low barrier height was combined with large contact area (several mm^2) in order to form an "ohmic" contact. For ohmic contact formation, the optically rough back side of the wafer was used. The native surface oxide was removed by BOE etching. As above discussed, BOE leaves the surface hydrogenated, but does not affect the initial surface structure. On top of the large contact area, the high surface roughness increases even further the effective contact area.

After BOE etching, the substrate was introduced into the HV DC sputtering chamber (see section 3.1). First a 5 nm thick Cr layer was deposited. Cr is known to form $CrSi_2$ silicides, even during room temperature deposition [*Kovsarian and Shannon*, 1998]. Moreover, the deposition directly on the H-Si surface, without any intermediate oxide layer, facilitates Cr diffusion into Si. Thus, besides the lower Cr/Si Schottky barrier height (Φ_B=0.61 eV [*Sze*, 1981]), Cr locally dopes Si, reducing the space charge region. This results in transport as well by electron tunneling through the Schottky barrier. A 200 nm thick AuSb layer was deposited immediately after, serving as electrical interconnect. Possible Sb diffusion through the Cr layer into Si, will result in an even higher local doping.

In order to characterize electrically the back-contact, 4-point probe current-voltage (I-V) measurements have been performed. Arrays of disk-shaped contacts have been fabricated on the back side of a wafer. Measurements have been performed between 4 mm diameter contacts, separated by various distances. The I-V characteristics show a clear ohmic behavior (figure 4.11a). The slope increases as the separation increases, since the resistance of the Si chip is also taken into account in the measurement. Figure 4.11b shows the resistance values as a function of the diode separation. By extrapolating the linear fit of the data to zero separation, the contact resistance of the two diodes is determined to be $\approx$80 Ω. The contact resistivity is determined to be $\approx$20 Ωcm^2, by multiplying the contact resistance with the contact area [*Berger*, 1972]. It should be noted that in the lateral current flow geometry used, the current distribution is not uniform. The current density at the two contacts is higher at the contact edges that face each other, reducing the effective contact area. This results in overestimation of the contact resistivity value, and more elaborate methods are necessary to determine it accurately [*Cohen*, 1983].

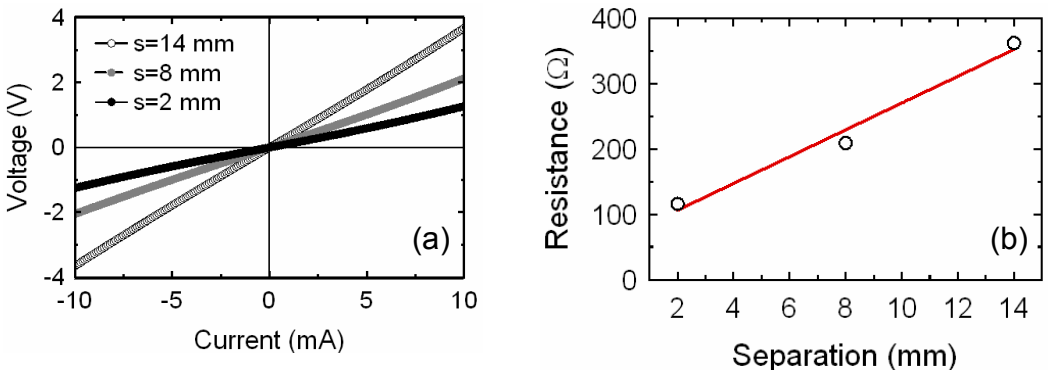

Figure 4.11: (a) I-V measurements performed between back-contacts having various edge-to-edge separations. A clear ohmic behavior is observed. (b) Resistance values as a function of contact separation. The continuous line correspond to linear fit of the data.

4.5 Au/Si(111) diodes: Au film structure and Schottky barrier height

The Au/Si(111) structure is of great importance since it provides a sufficiently high Schottky barrier and a template for the subsequent multilayer growth. The growth and structural characterization of the Au layer and the electrical characterization of the Au/Si Schottky contact will now be discussed.

4.5.1 Au layer deposition

After introduction of the H-Si(111) substrates into the UHV deposition chamber, Au films were grown at room temperature by e-gun thermal evaporation.

Room temperature deposition of Au on Si(111) was studied by synchrotron radiation photoemission spectroscopy [*Yeh et al.*, 1993]. According to these authors, during the initial stages of growth (up to 3-4 monolayers), deposited Au atoms react with the surface Si atoms forming a stable Au_3Si silicide layer. Further deposited Au atoms penetrate the silicide layer and metallic Au is nucleated at the silicide/Si interface. After the first monolayer of metallic Au has been formed, the silicide layer is detached from the substrate and further deposited Au results in the growth of the metallic Au layer. The final structure is composed of a 1-1.5 monolayer surface silicide layer and a sandwiched Au metallic layer with an atomically abrupt interface to the Si(111) substrate. No reacted Si component is found in the volume of the metallic Au layer and in the bulk Si.

4.5.2 Structural characterization

X-ray diffraction and reflection

We have performed X-ray diffraction (XRD) measurements for structural characterization of the Au films. The wide angle XRD spectrum of a Au(19 nm)/Si(111) structure collected in $\theta-2\theta$ scans is shown in figure 4.12a. The film was found to be textured and

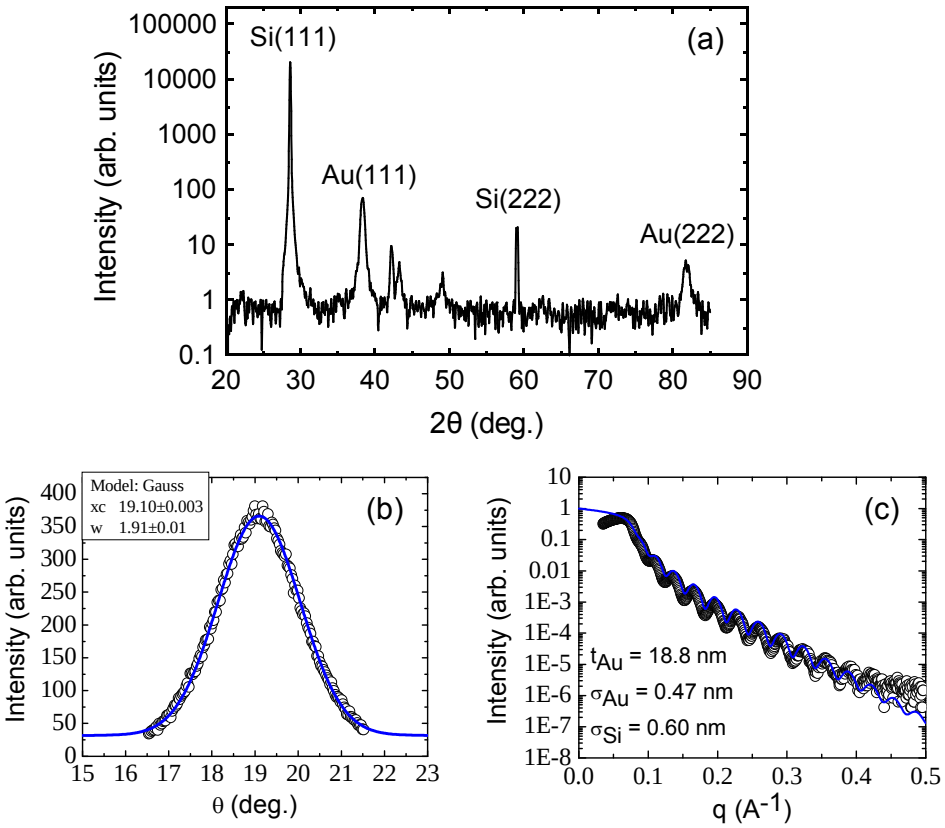

Figure 4.12: (a) Wide angle X-ray diffraction spectrum taken on a Au(19 nm)/Si(111) structure. (b) Rocking curve corresponding to the Au(111) peak. The continuous curve corresponds to a gaussian fit. (c) X-ray reflectivity measurement in the θ range 0.3° to 3.5°.

the Au crystallites are growing with the (111) alignment, in agreement with previous work [*LeLay et al.*, 1976]. Rocking curve analysis reveals a crystallite size of the order of 10 nm (FWHM≈ 2°) (figure 4.12b). The peak of the Au(111) planes is found at 2θ=38.4° determining a d spacing equal to d_{111}=0.234 nm, in good agreement with the fcc Au bulk value (0.236 nm). The peaks in the range 40° to 50° correspond to the brass (Zn and Cu) sample holder.

X-ray reflectivity measurements were performed in order to determine the thickness and roughness of the Au film (figure 4.12c). Interference fringes are observed up to

θ=3° (0.4 Å^{-1}) indicating a good uniformity of the film thickness, which is determined from the period of the fringes to be 18.80 nm, close to the nominal value (19 nm). The roughness values of the air/film and the film/substrate interfaces are determined to be 0.47 and 0.60 nm respectively from fitting analysis of the profile.

Transmission Electron Microscopy

Cross section high-resolution TEM has been performed to study the multilayer structure. The sample measured was a Au/Cu/Co/Cu/Co/Cu/Au/Si(111) spin-valve multilayer (for a detailed structure, see section 6.2). However, because of improper handling during sample preparation, the upper layers were ripped-off. The remaining structure imaged in figure 4.13 is a Co(1.8 nm)/Cu(1.5 nm)/Au(7 nm)/Si(111) multilayer (probably there is as well some remaining Cu on top of the Co layer). The dark band

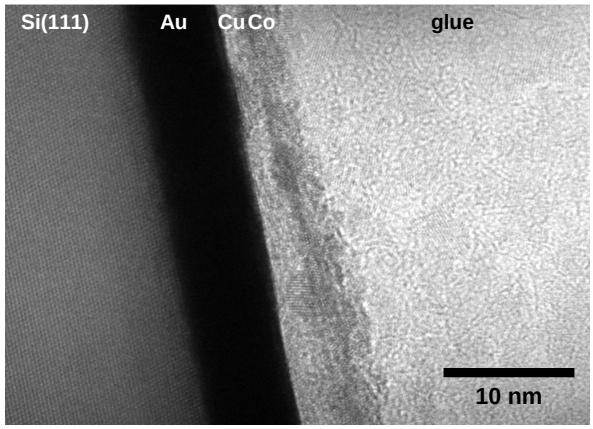

Figure 4.13: Cross-sectional high-resolution TEM image of a multilayer. The dark band corresponds to the Au layer (the high Au density results in low transmission). The Cu and Co layers can be also resolved. The polycrystalline structure of the Cu and Co layers is clearly demonstrated. (Measurements performed by Nathalie Brun, LPS, Orsay)

apparent in the image corresponds to the Au layer. The high Au thickness results in low electron transmission. The Cu and Co layers are barely resolved, since their density are comparable. On the left part the Si monocrystalline structure is shown. The mainly amorphous structure observed on the right part corresponds to the glue used for sample fabrication.

An important result deduced from figure 4.13, is the extraordinary planarity of the Au layer. It is clear that minimal roughness is observed at the Au/Cu interface, although that the scale of the image implies the presence of several Au grains. Moreover, no Au-Si interdiffusion is observed at the respective interface, within the resolution limit. Finally, several grains are observed in the Cu/Co bilayer, indicating the polycrystalline structure of the film.

4.5.3 Electrical characterization

The Au/Si contact was electrically characterized from 4-point probe I-V measurements at room temperature. The current density (J) versus voltage (V) measurement of a contact with area $\approx 13\ mm^2$ is shown in figure 4.14. A high quality rectifying behavior is observed. Thermionic emission can be assumed as the dominant transport mechanism, since the moderately doped n-type Si suppresses tunneling effects (see section 4.3.1).

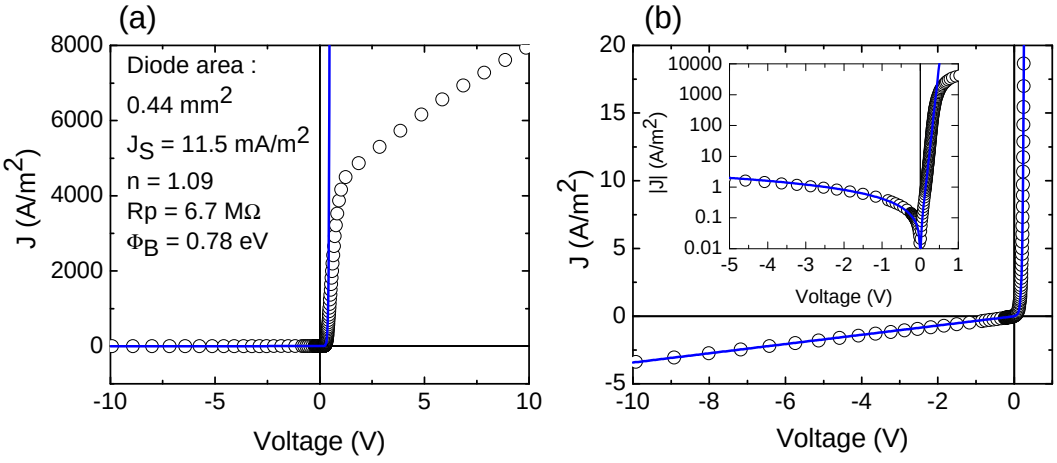

Figure 4.14: 4-point probe I-V measurements of a Au/Si (n-type) Schottky diode. The thermionic emission model was used to fit the data. Plot (b) is a zoom of plot (a), while the log scale inset demonstrates the agreement between experiment and fitting.

The thermionic emission model was used to fit the data (see section 2.3.1). The Schottky barrier height Φ_B is determined from J_s. The values determined are n=1.09 and Φ_B=0.78 eV (figure 4.14a), in good agreement with the values quoted in the literature [*Sze*, 1981]. In principle, Schottky contacts with ideality factor less than 1.1 were used for BEEM studies. The high Schottky barrier height determined for our diodes is in agreement with the abrupt Au/Si(111) interface discussed before.

While in forward bias conditions the Schottky barrier dominates transport, for practical Schottky diodes, the dominant reverse bias current is the edge-leakage current. This is caused by the sharp edge around the periphery of the metal plate, and results in a resistance parallel to the Schottky contact resistance. The effect of the parallel resistance is clearly shown in figure 4.14b. The value of the parallel resistance is 6.7 MΩ, as determined by the slope of the curve for reverse bias.

The change of slope observed for higher forward bias values is due to the back-contact. As discussed is section 4.4.2, a low barrier height and low parallel resistance Schottky contact is used as "ohmic" back-contact. In this case, when the Schottky contact is forward biased, the back-contact is reverse biased. The back-contact parallel resistance is much lower than the Schottky contact parallel resistance, and dominates transport for high forward bias values.

It should be noted that I-V measurements are not local and probe the whole contact area, giving more weight to regions with lower barrier height. Since BEEM is a local study, Schottky barriers higher than 0.8 eV are usually measured. However the presence of defective contact areas which reduce the Schottky barrier or the parallel resistance, result in higher Johnson noise in the BEEM current (see section 4.2).

A crucial step during sample preparation which can significantly deteriorate the Schottky contact quality, is the ultrasound microbonding process for the front-contact realization. An extensive study has been performed in order to determine the appropriate parameters for which microbonding does not affect the Schottky barrier height or the parallel resistance value.

4.6 Magnetic multilayers

The main aim of this work was to perform BEEM measurements on magnetic multilayers. In this section the fabrication and characterization of such type of samples is discussed.

4.6.1 Choice of materials

A spin-valve is relying for its operation on distinct and separate switching thresholds for the two magnetic layers, with one hard and one soft layer. Different coercivities in the two ferromagnetic layers may be achieved through the use of different layer thicknesses or different layer materials. Then, strictly speaking, such structures should be referred to as pseudo spin-valves [*Gadbois et al.*, 1998]. Both options were studied, with the latter being more successful.

Permalloy (Py, $Ni_{80}Fe_{20}$) was chosen as soft magnetic material because it exhibits low coercivity and almost zero magnetostriction. Low magnetostriction is critical for multilayer applications, where variable stresses in the thin film could cause a large variation in magnetic properties. Co was used as hard magnetic material since it exhibits much higher coercieve field. The spin-valves were fabricated by using as magnetic layers either two Co films, or a Co and a Py film.

A Cu film was always used as a spacer. Although the Cu hot electron attenuation length has not yet been determined, taking into account the lifetime calculation [*Zhukov et al.*, 2006] and the band structure, it can be supposed that it is high and comparable to Au (23 nm [*Weilmeier et al.*, 1999]). Moreover, the value was determined from photoemission experiments to be in the 5-20 nm range [*Crowell et al.*, 1962]. Low attenuation is desirable in order to attain higher ballistic signal.

The multilayers were always grown on a Au(7 nm)/Si(111) structure. As discussed in section 4.5, a surface silicide layer is present on top of the Au/Si(111) structure (see also [*Gheber et al.*, 1998; *Grupp and Taleb-Ibrahimi*, 1998]). The direct deposition of a magnetic layer on top of a silicide could result in a magnetically "dead" layer, and a Cu buffer layer is deposited first in order to cover the silicide layer. Since the surface

silicide layer is Au dominated and only 1-1.5 monolayer thick, we consider that it has the structure of the Au layer underneath.

Cu thin films electrodeposited on Au(111) have been shown to grow with the (111) crystallographic structure [*Viyannalage et al.*, 2007]. Moreover, Cu layers thermally evaporated on Au(111)/Si(111) substrate, have been found to be completely (111) oriented by the underlying Au, with their lattice constant being that expected for the bulk material and their in-plane alignment directly following that of the Au layer [*Weilmeier et al.*, 2000]. We consider the same orientation relations to hold true for the Cu layers used in this work, although structural characterization has not been performed. Room temperature UHV deposited Co on Cu(111) does not show any diffusion into the substrate, and grows layer by layer (in contrast to the three-dimensional growth on Au) forming an hcp lattice [*Gonzalez et al.*, 1981]. Room temperature deposition of Ni (the dominant element in Py) on Cu(111) results in smooth films, although growth is not two-dimensional [*Wulfhekel et al.*, 1999] and Py films grown on Cu(111) are found from XRD measurements to be (111) textured [*Kanak et al.*, 2002].

Besides acting as a Si diffusion barrier and the wetting effect, the Cu buffer layer is also reducing the lattice mismatch between the magnetic layer and Au. hcp Co has only 2% mismatch with fcc Cu, in contrast to 15% with fcc Au. The effect is similar for Py. By calculating an artificial lattice constant for Py using the empirical Vegard's law and the lattice constants for the bcc Fe and fcc Ni, Py is found to have 19% lattice mismatch with Au and 6% with Cu. The lattice mismatch between Au and Cu is 13%.

Important for BEEM studies on metallic multilayers is also the hot electron attenuation at the metal/metal interfaces. The transmission of the Py/Au and $Co_{70}Fe_{30}$/Au interfaces is found to be on the order of 30%, in contrast to the almost 100% transmission of the Py/Cu interface [*van Dijken et al.*, 2003] and the 50% transmission of the Co/Cu interface [*Rippard and Buhrman*, 2000].

The multilayer stack is finally covered by a capping layer. Au was chosen since it is sufficiently inert in ambient air and exhibits a considerably high hot electron attenuation length [*Weilmeier et al.*, 1999]. Moreover Au is already used to form the Schottky contact and thus it is not necessary to add one more material in the evaporator. A 3 nm thick layer is sufficient for protection during *ex-situ* transfer.

4.6.2 Magnetic characterization

Magnetometry measurements were performed using the magneto-optical Kerr effect (MOKE). An in-plane magnetic field was applied and the longitudinal Kerr rotation was measured using a green HeNe laser.

Co/Cu/Co trilayers

Figure 4.15a shows a series of MOKE hysteresis cycles of Co layers embedded in Cu with various thicknesses. The coercive field is shown to decrease with thickness from 16 Oe at 8 nm Co thickness to 1 Oe at 0.8 nm. It is interesting to notice that a

clear hysteresis is apparent even for 0.8 nm Co thickness, indicating that the film is continuous and with in-plane magnetization. The remanence magnetization is roughly equal to 70 % of the saturation magnetization. The switching occurs gradually and over a wide field range (±25 Oe for the 2.4 nm layer), indicating that the magnetization reversal occurs mainly by domain nucleation.

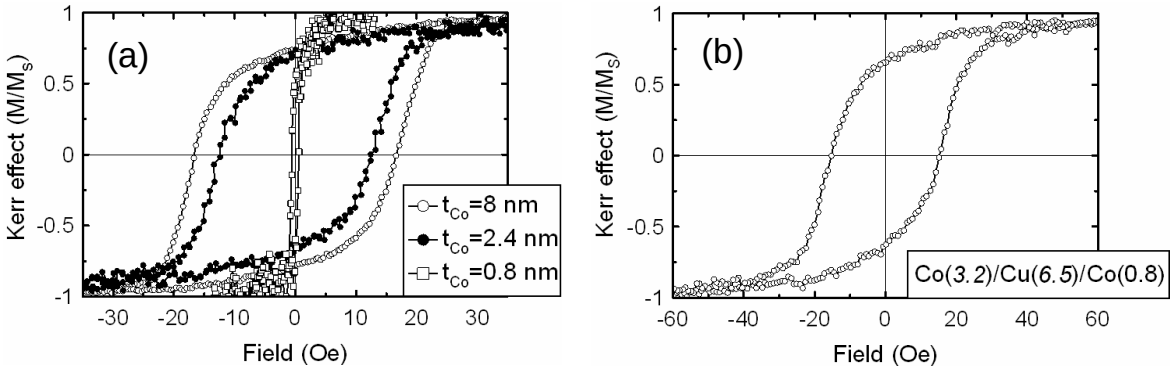

Figure 4.15: MOKE hysteresis cycles. (a) Single Co layers of various thicknesses. (b) A Co/Cu/Co spin-valve.

Hysteresis cycles were acquired for various angles of the applied field, and no in-plane easy magnetization axis was found. Since the Co layers are polycrystalline, even if an in-plane anisotropy is present in each grain, the effect is averaged over several grains and cancelled.

The significant difference between the coercive fields of the 0.8 nm and the 2.4 nm Co films, allows us to assume that a Co/Cu/Co trilayer incorporating Co layers with different thicknesses can behave as a spin-valve. Figure 4.15b shows a MOKE hysteresis cycle taken on a Co(3.2 nm)/Cu(6.5 nm)/Co(0.8 nm) trilayer. It is evident that the behaviour is not the expected one. Since the magnetization reversal process of the two Co layers is gradual, hysteresis cycles overlap and domains are presumably nucleated simultaneously in each film.

Samples with Cu spacer thickness up to 9 nm were measured, demonstrating always the same behavior. This is considered to be the result of roughness induced magnetostatic coupling between the two Co layers. Interlayer exchange coupling is not considered, since it was found to decrease rapidly for Co/Cu/Co trilayers as the Cu layer thickness increases, and vanishes for spacer thickness higher than 5 nm [*Parkin et al.*, 1991].

Co/Cu/Py trilayers

The option of using two magnetic layers of different material will be now discussed. Single Py layers embedded in Cu were fabricated and characterized by MOKE magnetometry. In figure 4.16a the hysteresis cycle of a 10 nm thick layer is shown. The

coercive field is found to be 0.8 Oe. As expected the value is much lower than the coercive field of a Co layer with comparable thickness. The remanence magnetization is almost equal to 100 % of the saturation magnetization. The abrupt magnetization reversal observed indicates a magnetization reversal dominated by domain growth. This important feature distinguishes a Py layer from a very thin Co layer with similar coercive field.

Figure 4.16b shows the hysteresis cycles of Co/Cu/Py trilayers with various thickness Cu spacers. For a 4 nm thick spacer, no distinct switching is observed, and the remanence magnetization is ≈90 % of the saturation magnetization value. The shape of the curve is vastly different for higher spacer thickensses. For 6 nm and 8 nm thick Cu spacers, the hysteresis curve is dominated by the gradual magnetization reversal of the Co layer. The independent switching of the Py layer is distinguished by the two slope changes apparent at ≈ ±5 Oe splitting each reversal curve in two segments. The magnetization reversal process of the Py film occurs in the 0-5 Oe range, and it is completely saturated for higher fields.

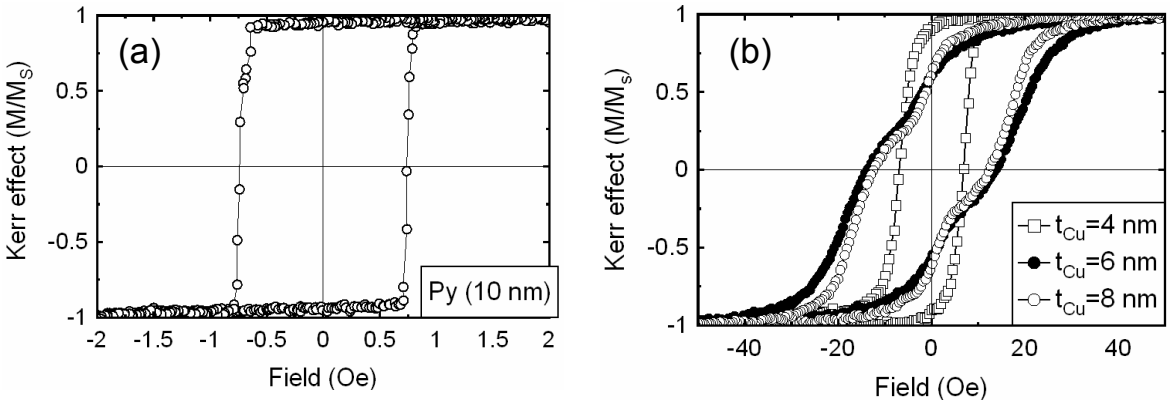

Figure 4.16: MOKE hysteresis cycles. (a) Single Py(10) layer (b) Co(1.8)/Cu(t)/Py(1.6) spin-valves with various spacer thicknesses. Numbers in brackets indicate thickness in nm.

The optimum Cu spacer thickness is determined to be 6 nm, since it sufficiently decouples the Co and Py layers, while leading to the minimum contribution to hot electron attenuation.

4.7 Sample fabrication process

The "recipe" developed for BEEM sample fabrication will be now described in detail.

4.7.1 Hydrogenated Si(111) substrates with ohmic back-contact

Commercially available[2] n-type (P doped) Si(111) wafers with resistivity 4-9 Ωcm (doping 10^{15} cm^{-3}) are used. They are single side polished, 300 μm thick, with a diameter 2 inches. The wafer miscut is less than 0.2°.

BOE (VLSI grade, HF 6%:NH_4F 36% 7:1) and NH_4F (VLSI grade, 40%) solutions[3] are used for etching. Deionized (DI) water (resistivity ≥15 MΩcm) purified by a Millipore system is used for rinsing. All the solutions used are contained in Teflon beakers. Before any treatment the DI water and NH_4F solutions are sparged with dry N_2 for at least 30 min using a Teflon tube.

First the ohmic back-contact is formed. The wafer is cleaned in acetone and alcohol in an ultrasonic bath. Droplets of BOE solution are applied *only* on the non-polished back surface by means of a Teflon pipette, until they completely cover the surface. Surface tension is enough to maintain on the surface sufficient amount of solution for native oxide removal. The front surface native oxide remains intact during this step. After ≈1 min of etching, the droplets are removed and the wafer is rinsed in DI water for 15 s and dried with pure N_2.

Immediately after, the wafer is mounted on the sputtering sample holder and a Cu plate shadow-mask is mechanically attached on it, before introduction into the HV sputtering chamber. After several hours of pump-down, Ar is introduced into the chamber and the pressure is stabilized at 0.1 mbar. An array of AuSb/Cr/Si disk shaped contacts with 4 mm diameter is fabricated using the mask. First, a 5 nm thick Cr layer is deposited at a rate 5 nm/min. A 200 nm thick AuSb layer is deposited on top, at a rate 40 nm/min. The Cr target has a 99.99 % purity and the AuSb target is an alloy of 99.9 % Au and 0.1 % Sb.

Afterwards, the wafer is diced in ≈ 5×5 mm^2 substrates each one having an ohmic back-contact. After a second acetone and alcohol ultrasonic cleaning step used to remove scribing residues, the front surface is treated. Droplets of BOE solution are applied only on the front surface for native oxide removal. Possible interference of the back-contact metalization would affect the chemistry leading to an extremely rough surface structure. After 1 min of etching the droplets are removed and the substrate is rinsed in DI water for 15 s. It is then dried with pure N_2 and NH_4F droplets are applied only on the front surface for the anisotropic etching step. After 30 s the droplets are removed and the substrate is again rinsed in DI water for 15 s and dried with pure N_2.

4.7.2 Multilayer deposition

High purity (99.999%) Au pellets were used as source material. The deposition rate was 0.15 nm/s , and pressure never exceeded 1×10^{-8} mbar during deposition.

Immediately after preparation, the substrate is mounted on the evaporation sample holder and a Cu foil shadow-mask is attached before introduction into the load-lock

[2]ACM, http://www.acm-pvd.com/

[3]BASF electronic chemicals, http://www.inorganics.basf.com/

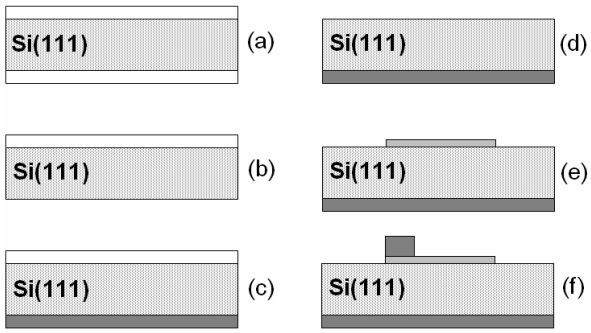

Figure 4.17: Schematic representation of the sample fabrication process (not to scale). (a) Both sides of the wafer are covered by the native oxide. (b) The non-polished back side native oxide is removed by BOE etching. (c) The AuSb/Cr/Si ohmic back-contact is formed via DC sputtering (d) Front surface treatment. The H-Si(111) surface is prepared by BOE and NH_4F etching. (e) Multilayer deposition by UHV evaporation using a Cu foil shadow-mask. (f) Au electric pad HV evaporation using a second Cu foil shadow-mask.

chamber. After 1-2 hours of pump-down, the substrate is introduced into the UHV evaporation chamber for multilayer deposition. One metal is deposited at a time, with a few minutes waiting time between two materials.

After the multilayer deposition sequence has finished, the sample is brought back to air. While it is still mounted on the evaporation sample holder, a second Cu foil shadow-mask is attached in such a way, that roughly two thirds of the multilayer surface are masked. Then the sample is introduced into the HV resistive thermal evaporation system for the Au electric pad deposition. A 200 nm thick pad is deposited at a rate 1 nm/s, with typical current value 230 A. The main source of BEEM sample heating is via radiation of the red-hot tungsten boat. In order to avoid annealing of the metal/semiconductor interface, the Au pad is deposited in four steps of 50 nm each, with at least 15 min waiting time between each step.

Finally, the sample is mounted on the BEEM sample holder for ultrasound microbonding. Extreme care must be experienced here, since mishandling can easily destroy the sample. The first bond is performed on the sample holder pad and the second on the BEEM sample pad. After microbonding, the sample is introduced into the microscope's UHV chamber for measurements.

4.8 Conclusion

In this chapter, the main issues that should be considered before designing a BEEM experiment, namely the choice of Schottky contact and substrate, were addressed. A sample fabrication process has been defined, with the use of mechanical masks as base technology. The drawbacks that emerged have been discussed. Particular fabrication

and measurement sample holders were conceived and fabricated. Before moving to the actual BEEM measurements (see chapters 5 and 6), various characterization techniques were used in order to gain insight in the structural, electric and magnetic properties of the BEEM samples. A preliminary knowledge of our samples was gained from those measurements, complementary to the one obtained from BEEM, thus contributing to the interpretation of the results discussed in the following.

Chapter 5

Ballistic electron emission microscopy of metal/silicon structures

5.1 Introduction

The first objective of this thesis was to perform BEEM measurements on metal/semiconductor structures. In this chapter, BEEM measurements on non-magnetic metal samples are presented and discussed. The choice of structures measured was made considering the main objective, which was the BEEM study of magnetic multilayer samples. The presence of non-magnetic layers is indeed necessary for the fabrication of such structures, so their contribution to the attenuation effects was studied and quantified. First, the results obtained from single Au and Cu layers on Si(111) are discussed. The Schottky barrier height was measured in both cases. BEEM imaging was performed to verify the homogeneity of the important Au/Si interface. Next, BEEM spectroscopy measurements were performed on a Au/Cu/Au/Si trilayer sample, in order to determine the attenuation effect at the Au/Cu interface. Finally, samples with sub-monolayer coverages of magnetic materials (Co or Py) were studied.

5.2 BEEM study of the Au(111)/Si(111) interface

The importance of the metal/semiconductor interface of a BEEM sample was discussed in chapter 2. The ability to fabricate a homogeneous Au(111)/Si(111) interface is crucial to perform magnetic BEEM measurements. The presence of an inhomogeneous interface, would lead to a significant non-magnetic contrast, which adds to the magnetic signal. Since a Au(111)/Si(111) structure is the base for every BEEM sample studied during this thesis, the quality of this necessary metal/semiconductor interface was studied by BEEM spectroscopy/imaging measurements.

5.2.1 Schottky barrier height: Spectroscopy measurements

The current-voltage measurements of the Au/Si junction presented in chapter 4 show a Schottky barrier height close to 0.8 eV. As those measurements are macroscopic, BEEM spectroscopy was also performed to study the interface at the nanometric scale.

Various Au(111)/Si(111) BEEM samples were fabricated and measured. Figure 5.1 shows BEEM spectra taken on a sample with a 7 nm thick Au layer. In figure 5.1a, some spectra with increased noise are apparent, especially at high tip voltages. A single threshold is observed for all spectra at ≈0.8 eV. A linear increase is observed away from the threshold. The slope of this part is equal to a constant transmission factor (the parameter T in equation 2.18), which is related to all the energy-independent scattering sources (injection geometry, defects, impurities).

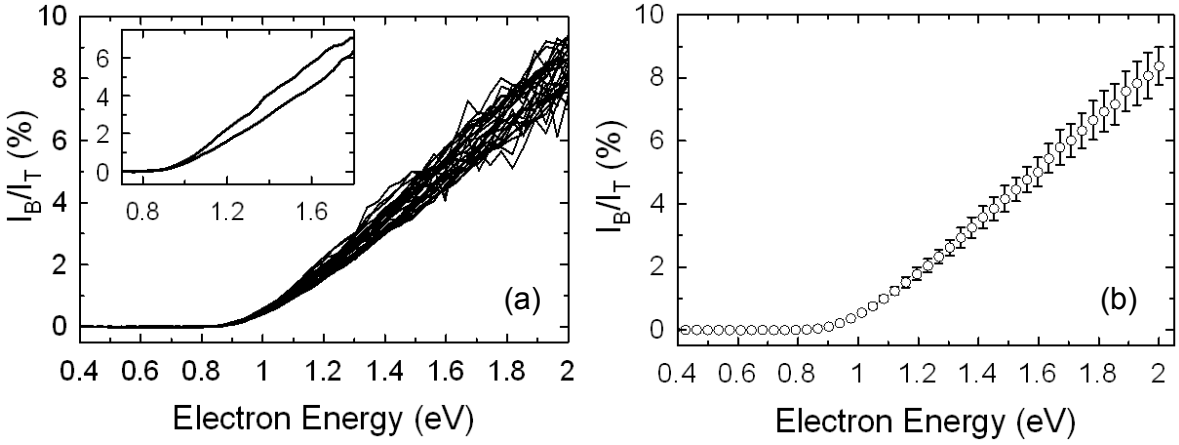

Figure 5.1: Hot electron transmission ($T = I_B/I_T$) versus injection energy of a Au(111)/Si structure. (a) 32 single spectra taken at various positions of a 100×100 nm^2 scanning area. (b) Averaged spectrum. The error bars correspond to the standard deviation of the measurement ($\pm\sigma$). The inset in (a) shows two extreme spectra. Injection current I_T=1 nA.

The inset shows two extreme cases, where although the onset is the same, the transmission is significantly different. Since the defect and impurity density is constant for the whole film, the principal source of variation between the two spectra is considered to be the injection geometry. The films studied are polycrystalline (see chapter 4). Electrons that tunnel from the tip to the edges of a grain, will be injected into the film at an angle with respect to the normal of the plane of the metal/semiconductor interface. This causes the ballistic electrons to travel a longer path until they reach the metal/semiconductor interface, and thus attenuate more. Further, their highly off-normal momentum direction, causes high reflection at the metal/semiconductor interface, additionally reducing the transmitted ballistic electrons. This is shown schematically in figure 5.2a. Higher transmission is anticipated for injection at the center of a grain, than at the edges. Spectroscopy curves acquired on polycrystalline films show

an overall transmission that scales inversely with the injection angle [*Bauer et al.*, 1993]. Those local variations of the BEEM transmission because of the surface structure are always present, and during imaging give rise to a contrast related to surface topography [*Ventrice et al.*, 1996].

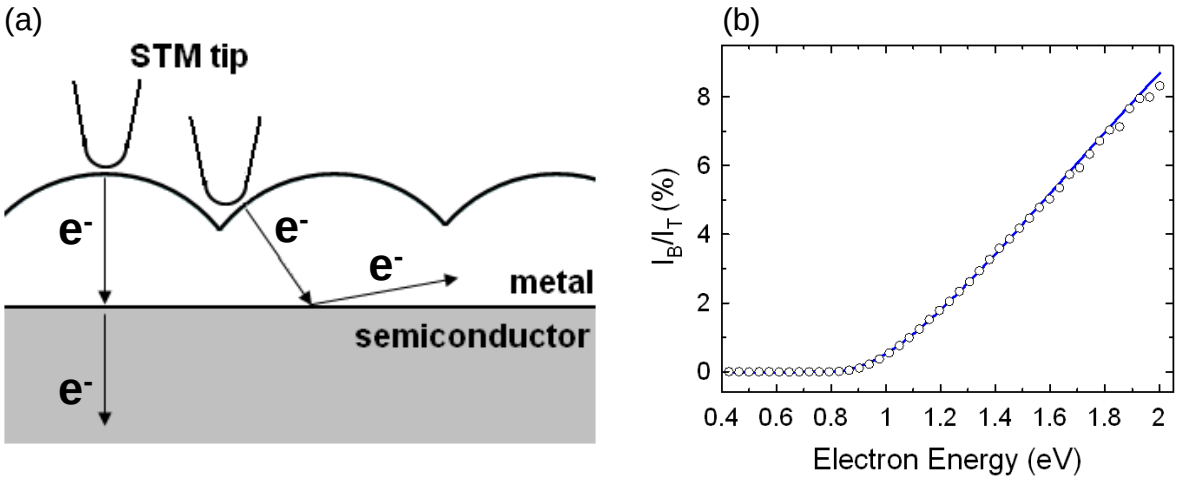

Figure 5.2: (a) The effect of surface topography on the BEEM signal (not in scale). Only purely ballistic electron trajectories are shown. (b) The averaged BEEM spectrum of figure 5.1 along with a fit to the data (solid line).

In figure 5.1b, the average of the spectra is shown. The error bars correspond to the standard deviation of the measurement. However, considering the previous discussion, they mainly indicate the local variations of transmission because of the surface structure, and to a lesser extent the actual noise of the measurement. Further measurements supporting this kind of transmission dependence on the surface gradient, are discussed in section 5.5.2.

The Schottky barrier height (Φ_B) is obtained by fitting the averaged BEEM spectra using the extended Bell-Kaiser model described in section 2.3.3. Figure 5.2b shows the average BEEM spectrum of figure 5.1b. The solid line is a least squares fit of equation 2.18 to the data. Similar fitting procedures were performed systematically. In all cases, Φ_B is found to be in excess of 0.8 eV (0.831±0.002 eV for the spectrum shown in figure 5.2b), higher than the value obtained from macroscopic measurements. The data of figure 5.2b are fitted for the whole energy range. The model reproduces the data quite well over the full energy span, including the threshold region. Those results are in agreement with previous BEEM spectroscopy studies of the Au/Si interface [*Kaiser and Bell*, 1988] (see figure 2.6).

5.2.2 Interface homogeneity: Imaging

Although BEEM spectroscopy measurements provide a local probe of the metal/semiconductor interface, a more detailed view is achieved by BEEM imaging.

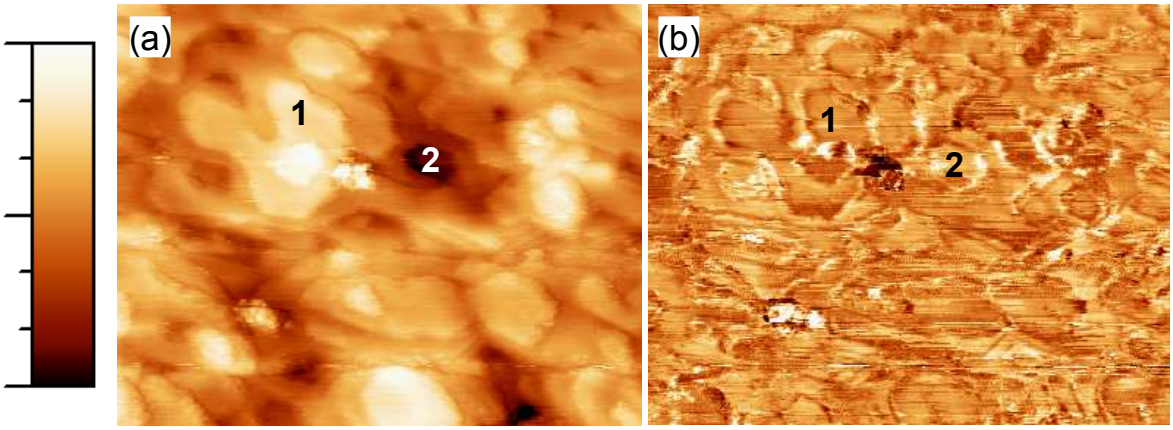

Figure 5.3: BEEM imaging of a Au/Si structure. (a) Topographic signal. The color scale corresponds to height extending from 0.00 to 1.74 nm. (b) BEEM signal. The color scale corresponds to transmission ranging from 3 % to 8 %. Scan size 100×80 nm^2, V_T=2 V, I_T=2 nA.

Figure 5.3 shows a BEEM image taken on the same Au(7 nm)/Si(111) sample, along with the corresponding topographic image. The Au film is polycrystalline, and the grain width is 10-20 nm. The BEEM contrast can be directly correlated with surface topography features. In general, ballistic transmission is homogeneous, except along grain edges where depressions of the BEEM signal are observed. Some surface contamination is apparent (center and bottom left), leading either to high, or zero transmission. The zones marked as "1" and "2" correspond to a height difference of ≈1.2 nm. However, the BEEM signal is almost identical in both cases, since the hot electron attenuation length in Au (23 nm [*Weilmeier et al.*, 1999]), is much longer than the observed height difference. The homogeneity of the Schottky interface can be deduced from the BEEM image. All sources of BEEM contrast are correlated to the surface structure (surface gradients or contamination). The total absence of an interface contrast in figure 5.3 is attributed to an homogeneous hot electron attenuation at the metal/semiconductor interface.

As the major energy and momentum hot electron filtering occurs at the metal/semiconductor interface, possible inhomogeneities of the Schottky barrier would dominate the BEEM signal. Figure 5.4 shows BEEM imaging and spectroscopy measurements taken on a different Au(7 nm)/Si(111) sample. As in figure 5.3, the BEEM contrast can be correlated with the surface structure, and BEEM signal depressions are observed at grain edges. In this case, however, large areas including several grains, are observed to exhibit extremely low transmission. Although the zones marked as "1" and "2" correspond to a height difference of ≈0.9 nm, the ballistic transmission is quenched from more than ≈6 % in "1" to ≈2 % in "2", a signal decrease that cannot be attributed to the higher local film thickness.

In order to detect the source of this strong attenuation, BEEM spectroscopy is

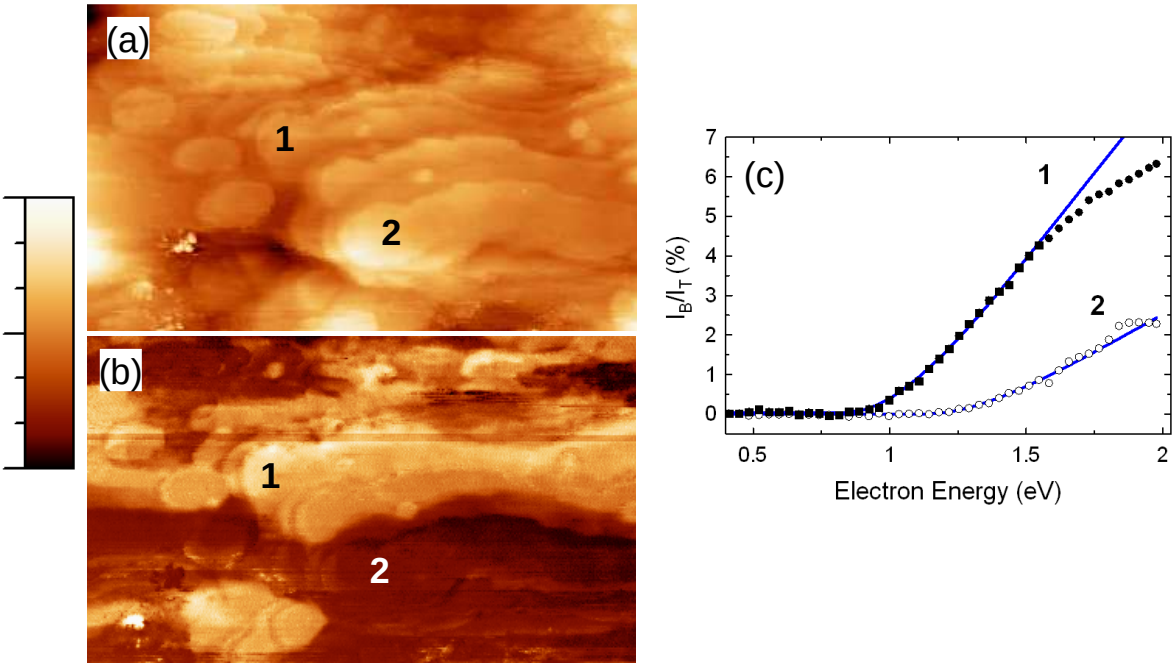

Figure 5.4: BEEM imaging of a Au/Si structure. (a) Topographic signal. The color scale corresponds to height from 0.00 to 1.97 nm). (b) BEEM signal. The color scale corresponds to transmission from 3 % to 8 %. Scan size 100×60 nm^2, V_T=2 V, I_T=3 nA. (c) BEEM spectroscopy curves taken in each zone. Solid lines represent fittings to the data. Injection current I_T=3 nA.

performed within each of the two zones. Figure 5.4c shows two single spectra taken in each case. It is evident that there is a transmission difference throughout the whole energy range. Moreover, in the case of spectrum "2", the threshold is found at a higher energy. By following a similar fitting process as in figure 5.1 (in this case only for data up to 1.6 eV), the Schottky barrier height is determined to be 0.864±0.012 in zone "1" and 1.144±0.024 in zone "2". Thus, the transmission difference is attributed to the higher local Schottky barrier, ruling out enhanced attenuation in the volume of the Au grains.

It could be assumed that the above results are due to contamination of the initial H-Si(111) surface during substrate transfer to the deposition system. Another possibility could be an incomplete etching of the Si surface native oxide, due to a failure during the chemical treatment. However, it should be noted that such a result is rather rare, and usually homogeneous Au/Si(111) interfaces were fabricated.

5.2.3 Scattering BEEM

Scattering BEEM measurements have been performed on the homogeneous Au(7 nm)/-Si(111) sample (see figure 5.3). Figure 5.5a, shows the SBEEM spectra acquired. The

sign of the X axis is negative, since in our setup the STM tip is grounded, and for reverse bias conditions, negative voltage is applied to the sample. No divergence between the

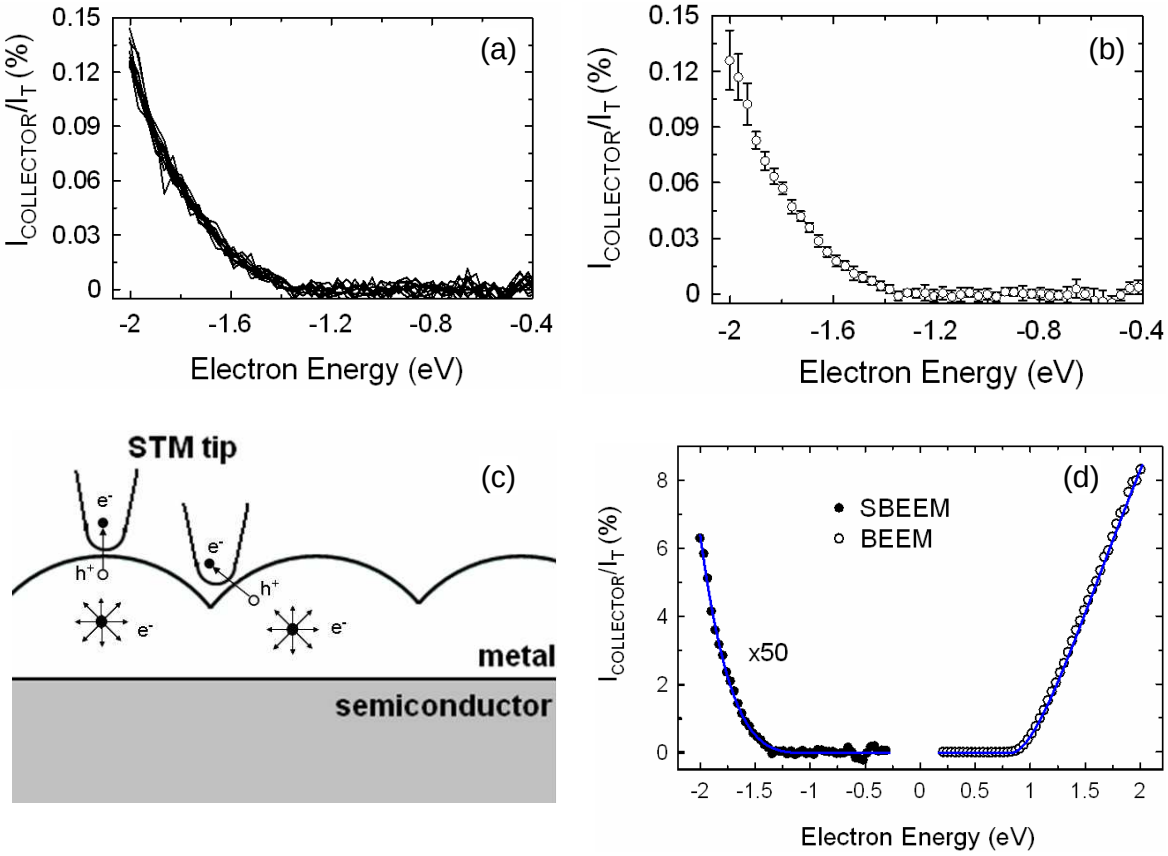

Figure 5.5: (a) 14 single SBEEM spectra taken at various positions of a 500×500 nm^2 scanning area. I_T=5 nA. (b) Averaged spectrum. The error bars correspond to the standard deviation of the measurement ($\pm\sigma$). (c) Schematic representation of the hole injection geometry effect (not to scale). Created hot electrons have been placed away from the injected holes for reasons of clarity. (d) Comparison between the BEEM and SBEEM spectra shown before. The solid lines correspond to fits according to the theory discussed in the text.

individual spectra is observed. The dependence of the spectral behavior on the surface topography observed for the BEEM spectra (figure 5.1), it is totally absent in this case. This is expected, since the hot electron creation process occurring in the volume of the film, is independent of the hot hole injection geometry. This is shown schematically in figure 5.5c. In all cases, the injected holes lead to the creation of hot electrons with isotropic momentum distribution.

In figure 5.5b, the average of the spectra is shown. The error bars in this case arise from the noise of the measurement. It can be noticed that the error bar width is constant almost throughout the whole energy range, since the measurement noise

is energy independent (see section 2.3.1). Larger error bars for the most negative tip voltages, may be attributed to STM tip instabilities under high tunnel gap bias.

It is obvious that the spectral shapes of BEEM and SBEEM spectra are quite different. This can be attributed to the momentum distribution of the hot electrons in each case. In the case of BEEM, the injected hot electrons are strongly forward focused. In the case of SBEEM however, the isotropic momentum distribution of the secondary hot electrons created into the Au layer (see figure 5.5c), causes more electrons to be momentum filtered at the metal/semiconductor interface. This affects the spectral intensity, leading to much lower SBEEM signal and different spectral behavior (see section 2.3.4). From a quick reading of the spectra, the signal threshold is expected at ≈1.3 eV, i.e. a value much higher than the Schottky barrier height. A similar behaviour has been observed previously [*Bell et al.*, 1990; *Niedermann et al.*, 1993]. Since the energy filtering is defined by the Schottky barrier height, this difference in the threshold should not exist. This could be explained if the magnitude of the SBEEM signal in the energy range close to the Schottky barrier height is below the detection limit, thus leading to the observed behavior.

The averaged SBEEM spectrum may be fitted above threshold according to the $I_B/I_T \propto (V - V_0)^{9/2}$ formula [*Bell et al.*, 1990] (see section 2.3.4). Below threshold zero transmission is considered. The Schottky barrier height is then determined to be 0.923±0.030 eV from a least squares fit to the whole data range (figure 5.5d).

In figure 5.5d the BEEM and SBEEM spectra are compared. The SBEEM spectrum needs to be magnified 50 times in order to become comparable to the BEEM spectrum. The differences mentioned before in the magnitude of the signal and the spectral shape are evident.

5.3 Au/Cu/Au/Si(111) structures

As it was the main aim of this work, BEEM measurements on magnetic samples with structure Au/Cu/(Co or Py)/Cu/Au/Si have been performed, and they are discussed in chapter 6. With this context in mind, the magnitude of hot electron scattering at the additional Au/Cu interfaces was studied by measuring the ballistic electron transmission of a Au(3 nm)/Cu(3 nm)/Au(7 nm)/Si(111) sample.

Figure 5.6 shows the average of 25 spectra taken at various positions of a 300×300 nm^2 image. As before, the signal threshold corresponding to the Au/Si Schottky barrier is observed above 0.8 eV. The spectrum of figure 5.1, taken on a Au(7 nm)/Si sample, is also shown for comparison. Obviously, the transmission is considerably reduced by adding the Cu layer.

It could be assumed, that the source of this transmission difference is the additional total layer thickness. In order to clarify this point, the Au/Cu/Au/Si sample spectrum is corrected for this thickness difference. As a first approximation, equal hot electron attenuation lengths in Au and in Cu are considered. The corrected spectrum is shown in figure 5.6, taking into account the exponential dependence of transmission versus

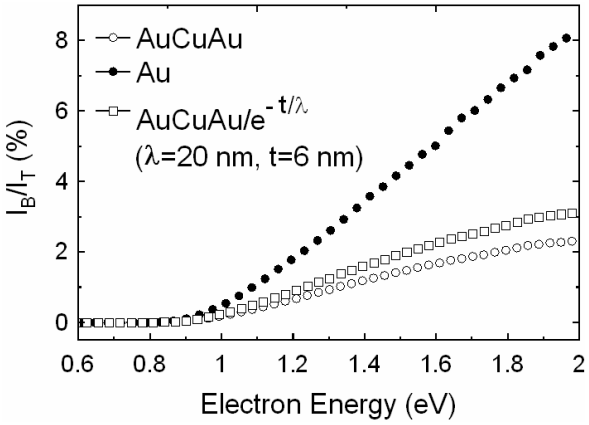

Figure 5.6: Averaged BEEM spectra taken on Au/Cu/Au/Si (open circles) and on Au/Si (filled circles) samples. The open squares correspond to the Au/Cu/Au/Si spectrum, corrected for layer thickness difference between the two samples.

layer thickness, a thickness difference of 6 nm, and an attenuation length of 20 nm. It is clear, that the transmission is still considerably lower than that of the Au/Si sample.

This transmission difference could be explained considering different attenuation lengths in Au and in Cu. The two spectra would coincide for a λ_{Cu} value of ≈2 nm. However, this value is several times smaller than the 5-20 nm range determined from photoemission experiments [*Crowell et al.*, 1962]. Moreover, from the Au and Cu band structures, similar magnitude of electron-electron scattering is expected, and consequently, similar attenuation lengths.

From the above discussion it becomes clear, that non negligible hot electron scattering occurs at the Au/Cu interfaces. Comparing the spectrum of the Au/Si sample to the corrected spectrum of the Au/Cu/Au/Si sample, the first is found to exhibit more than two times higher transmission, at 1.5 eV. Thus, the hot electron transmission of the Au/Cu interface is determined to be ≈70 %, considering equal attenuation at each of the two interfaces. The observation of such an interface scattering, could be explained by the presence of structural defects at the Au/Cu interface. A high density of such defects is anticipated, because of the 13 % lattice mismatch between fcc Au and fcc Cu (as calculated in section 4.6.1).

Although this scattering source is significant, it is not the most important hot electron attenuation source in samples containing magnetic layers. In the later case, scattering at the magnetic/nonmagnetic interfaces and in the volume of the magnetic layer is more intense. This issue will be discussed in chapter 6.

5.4 Cu/Si(111) structures

The Cu/Si(111) Schottky interface was the second metal/semiconductor structure studied by BEEM during this thesis. The low Cu/Si(n-type) Schottky barrier height (Φ_B=0.58 eV, [*Sze*, 1981]) dictates the formation of small area diodes for a room temperature study (see section 4.2.1). The room temperature zero voltage sample resistance (section 4.2.1) of a Cu/Si(n-type) diode with contact area 0.45 mm^2, is calculated from formula 4.3 to be 2.5 kΩ. This value is considerably lower than the desired value ($\geq$1 MΩ, see section 4.2.1). In this section, a simple method for the fabrication of extremely low area ($\approx 1-2\times10^{-3}$ mm^2) diodes is presented, which allows the room temperature BEEM study of the Cu/Si(n-type) interface. It should be noted that to our knowledge, this experiment has never been performed. However, the Cu/Si(p-type) interface (Φ_B=0.46 eV, [*Sze*, 1981]) has been already studied by Ballistic Hole Emission Microscopy [*Banerjee et al.*, 2005a]. In this case, the experiments were made possible by a combination of microfabricated small area ($\approx 18\times10^{-3}$ mm^2) diodes and low temperature (150 K) measurements.

5.4.1 Sample fabrication and measurement

For this study only one Cu/Si(111) sample was fabricated. Furthermore, it is the only one mentioned in this thesis fabricated with the triple e-beam evaporator described in section 3.1.3. For sample fabrication, a Cu foil shadow mask is attached on the substrate surface, as usual (see chapter 4). The typical mask-surface separation is 10-20 μm. The mask defines a rectangular 0.5×1 mm^2 diode on the substrate. First, a Au film is evaporated to form a Schottky contact with barrier height exceeding 0.8 eV. On top of it, the desired Cu film is deposited. The two films are evaporated from different sources, resulting in imperfect overlapping, as shown in figure 4.2. A misalignment of 1-2 μm occurs along each long side (because of deposition geometry), with the Cu misaligned region being the interesting one. In this way, a 1-2×1000 μm^2 Cu diode is formed. BEEM study is conducted on this part of the layer, by simply positioning the STM tip on top of it (figure 5.7), a manifestation of the local character of the technique.

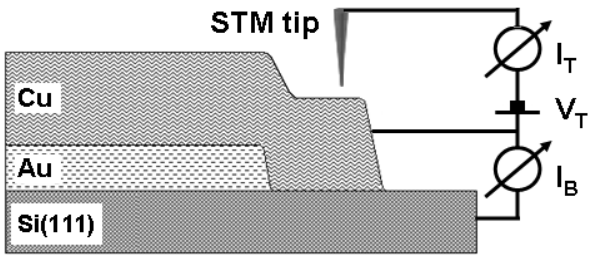

Figure 5.7: Configuration of the experiment: The STM tip is positioned on top of the Cu layer, which is in direct contact with Si (not to scale).

The sample measured, consisted of a 12 nm thick Cu layer deposited on top of a 6 nm thick Au layer. In figure 5.8 the misalignment between the the two metal layers is measured at the side where Cu exceeds. In (a), an average of AFM profiles is shown. Zone A corresponds to the Cu(12 nm)/Au(6 nm)/Si structure, since the total thickness is measured to be 18 nm. Zone B corresponds to the Cu(12 nm)/Si structure. The width of this zone is measured, quite accurately, to be ≈ 1 μm. Due to inhomogeneities on the edge of the Cu foil mask, this width is expected to vary from zone to zone. Finally, zone C corresponds to the Si(111) surface. The two transition zones (A→B and B→C), result from the mask-surface separation. In (b), an SEM micrograph is shown. Again, three distinct zones are apparent, along with the transition zones. The inhomogeneities at the edges of the metal bands resulting from the mask, are clearly imaged. The Cu/Si zone is measured to be 1-2 μm wide.

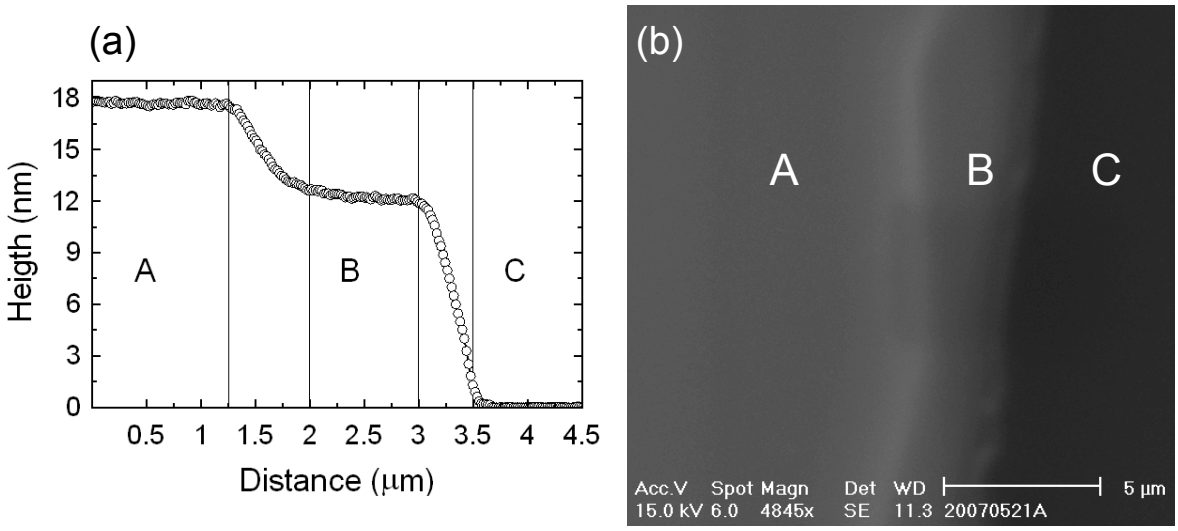

Figure 5.8: Measurement of the misalignment between the two metal layers : (a) AFM and (b) SEM. In both cases, zone A corresponds to the Cu/Au/Si structure, zone B to the Cu/Si structure, and zone C to the Si(111) surface.

5.4.2 Schottky barrier height

As in section 5.2, BEEM spectroscopy measurements were performed to determine the Cu/Si Schottky barrier height. Figure 5.9a shows BEEM spectroscopy measurements performed on the Cu/Si zone of the sample. In all cases, a single threshold is observed at ≈0.6 eV, indicating the homogeneity of the Cu/Si interface. A linear increase of the signal is observed away from the threshold, up to ≈1 eV. However, in the 1-1.5 eV range, the signal saturates, or even decreases in some spectra. Such a behavior has never been observed in the Au/Si or Au/Cu/Au/Si samples. In the latter case, the Cu layer is 4 times thiner than the one studied here. A possible explanation for this effect, would

be enhanced inelastic electron-electron scattering for elevated energies, as observed previously for Mg films on GaP [*Bauer et al.*, 1993]. However, further experiments are needed to clarify if such an effect indeed exists, or whether this behavior is simply caused by STM tip instabilities.

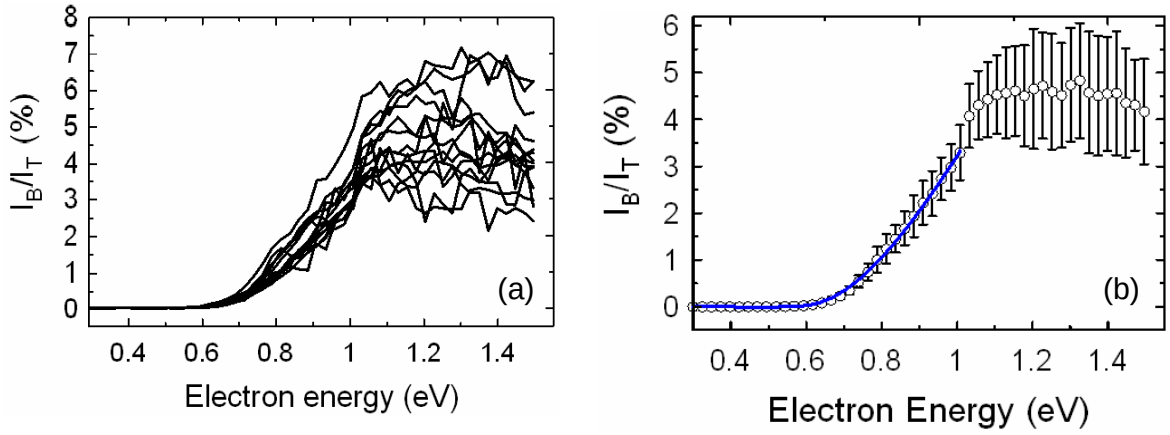

Figure 5.9: Hot electron transmission versus injection energy of a Cu/Si structure. (a) 14 single spectra taken at various positions of a 100×100 nm^2 scanning area. (b) Averaged spectrum. The error bars correspond to the standard deviation of the measurement ($\pm\sigma$). The solid line represents a fit to the data according to the model discussed in the text. Injection current I_T=3 nA.

Figure 5.9b shows the averaged spectrum. As in figure 5.1, for energies up to 1 eV, the error bars indicate mainly the roughness of the Cu layer surface, and not the measurement noise. For higher energies, large variations of the spectral shape are observed from spectrum to spectrum, which along with the enhanced measurement noise, result in much wider error bars. As mentioned earlier, the physical meaning of the spectral behavior for high energies is not yet clear.

The Schottky barrier height is determined by the same fitting process as before (figure 5.2b). The solid line shown in figure 5.9b, represents a least squares fit to the data using the extended Bell-Kaiser model (section 2.3.3). Φ_B is measured to be 0.614±0.007 eV, in reasonable agreement with the 0.58 eV value determined from macroscopic measurements [*Sze*, 1981]. The model is used to fit the data up to 1 eV, and reproduces the spectral shape accurately.

5.5 Samples containing Co and Py in sub-monolayer coverages

In this section, the study of BEEM samples containing magnetic materials in sub-monolayer coverages is discussed. The magnetic materials (Co or Py) were inserted in

the Cu layer of Au/Cu/Au trilayers. Since sub-monolayer coverages were deposited, it is expected that a part of the samples will have the Au/Cu/Au/Si structure, and the rest the Au/Cu/(Co or Py)/Cu/Au/Si structure. The initial objective was to determine the magnitude of the hot electron attenuation at the Co/Cu and Py/Cu interfaces, by comparing the transmission at the two zones mentioned before. A similar study is discussed in reference [*Rippard and Buhrman*, 2000]. This parameter is important for the magnetic BEEM studies that will be discussed in chapter 6. However, the obtained results were not the expected ones, although quite puzzling and thus interesting.

5.5.1 Sample fabrication and structure

The sample fabrication method is the same as for all samples (see section 4.7). After the deposition of a Au layer to form the Schottky barrier, a Cu layer is grown before the deposition of the magnetic material. The only difference is that less than one monolayer of magnetic material is deposited. Afterward, a Au/Cu capping layer is deposited. The deposition rate for the non-magnetic layers growth was 0.1 nm/s.

The detailed structure of the samples measured is Au(3)/Cu(1.5)/(Co or Py)/-Cu(1.5)/Au(7)/Si(111), where the numbers in brackets indicate thickness in nm. Two samples containing Co and one containing Py were fabricated. For the first Co sample (sample Co-A), Co was deposited until reaching an equivalent 0.1 nm continuous layer thickness (0.5 monolayer). The deposition rate was 0.003 nm/s. A second Co cluster sample was fabricated (sample Co-B). The quantity of Co atoms that would correspond to a continuous layer of 0.2 nm (1 monolayer) thickness was deposited, at a deposition rate 0.04 nm/s. Finally, a Py sample was fabricated (sample Py). The quantity of atoms that would correspond to a continuous layer of 0.1 nm was deposited. The deposition rate was 0.003 nm/s, as in the Co-A sample. As the source material was Py ($Ni_{80}Fe_{20}$) (see section 4.6), the same composition is assumed for sub-monolayer deposition. Considering the Ni lattice constants, the deposited material corresponds to a 0.5 monolayer coverage.

5.5.2 Sample transmission

STM and BEEM imaging of the Co-A sample is shown in figure 5.10. As was discussed in section 5.2.1, the surface structure of the film (figure 5.10a) modulates the BEEM signal (figure 5.10b). Besides the minor transmission decrease at grain edges, intense transmission depressions are observed, that can be directly correlated with certain grains apparent in the topographic image. The majority of those zones corresponds to grains higher than the average height of the image. The source of this transmission decrease can be attributed to the presence of the buried magnetic material.

As the amount of the deposited Co atoms corresponds to one half of a monolayer, it is clear that the apparent coverage (4.5 %) is much lower than expected. It is assumed that the deposited Co aggregates, and forms clusters several monolayers high. A schematic representation of the assumed sample structure is shown in figure 5.11. The

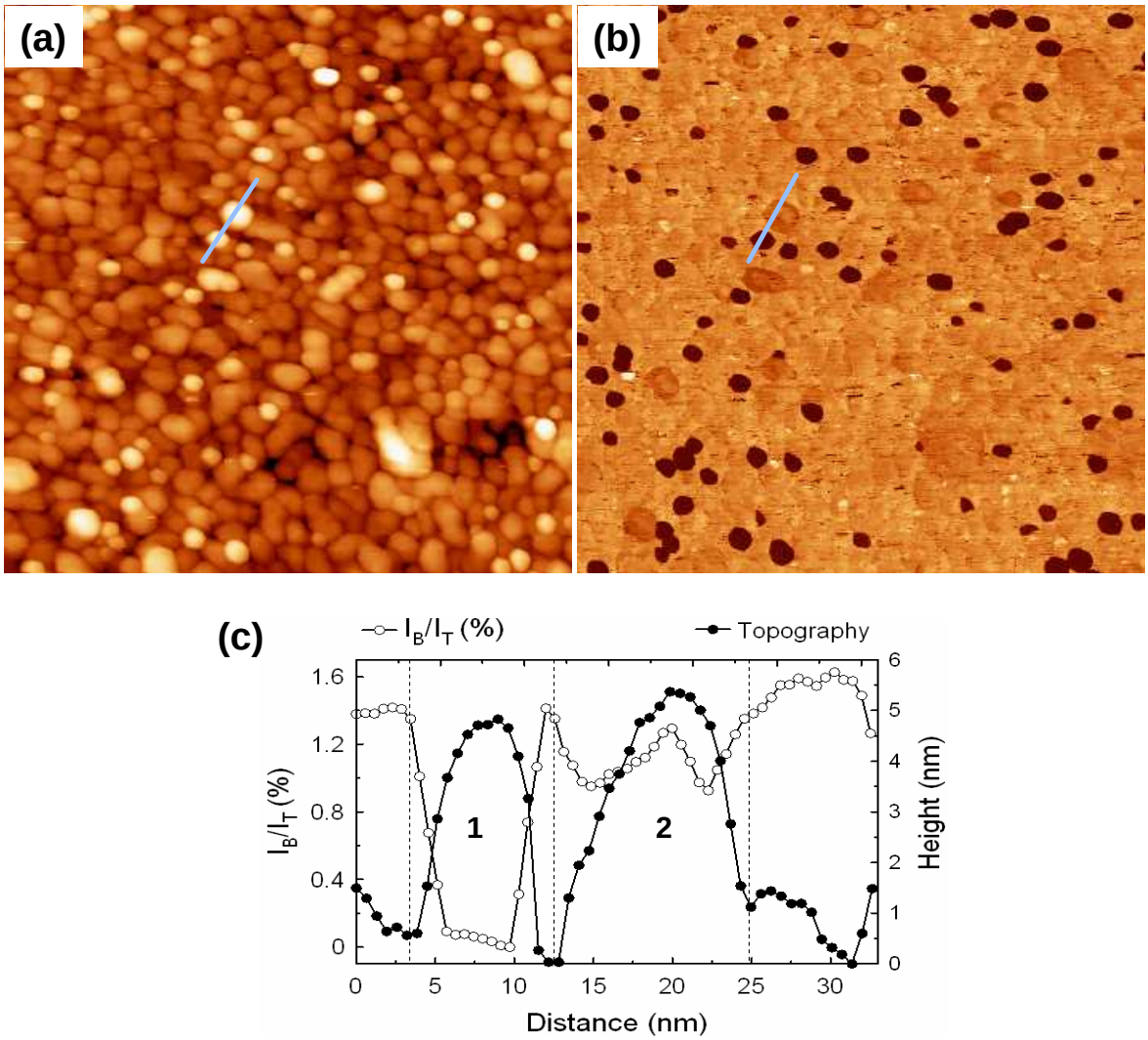

Figure 5.10: BEEM imaging of the Co-A sample. (a) Topographic signal. The color scale corresponds to height from 0.00 nm to 7.14 nm. (b) BEEM signal. The color scale corresponds to transmission from 0.01 % to 2.0 %. Scan size 200×200 nm^2, V_T=1.5 V, I_T=5 nA. (c) Line profiles taken across the line shown in the topographic and BEEM images.

presence of a cluster results in significantly lower hot electron transmission, due to volume and/or interface scattering. A total of 87 clusters is measured in the 200×200 nm^2 BEEM image with an average 6.3 nm diameter. From this difference between the nominal and measured coverage, the cluster heigth can be determined and it is found to be 2.2 nm. This way, the increased height of the grains can be explained by the additional buried material present. However, it should be noted that the mechanism that results in the aggregation and growth of 2.2 nm high Co clusters on a rough Cu surface is not

known.

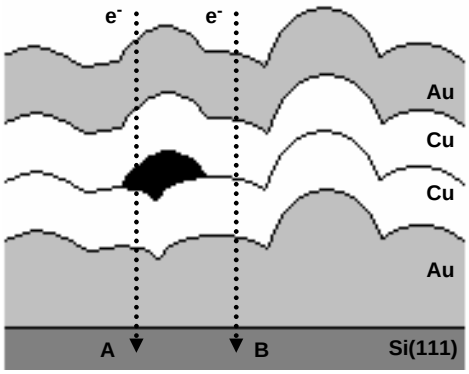

Figure 5.11: Schematic representation of the assumed sample structure (not to scale). The zone in black indicates a buried cluster. In case (A), the additional attenuation because of the presence of the cluster results in lower transmission than in case (B).

The average transmission, neglecting the zones where a cluster exists, is 1.47 % (at 1.5 eV electron energy). This value is in excellent agreement with the BEEM spectroscopy measurements of the Au(3)/Cu(3)/Au(7)/Si(111) sample shown in figure 5.6. In that case, 1.44 % transmission was measured at 1.5 eV electron energy. In the presence of a cluster, the average transmission is reduced ≈50 times to 0.03 %.

It is evident that some of the higher grains apparent in the topographic image, do not correspond to such intense signal depressions in the BEEM image. Those inhomogeneities of the film thickness are, therefore, logically not related to the presence of the buried clusters. They, as well, exhibit reduced transmission, but to a much smaller extent. The enhanced attenuation is here attributed to the additional layer thickness and to the increased surface profile gradients because of the locally increased height.

In figure 5.10c, line profiles are shown, taken across the line apparent in the topographic and BEEM images (figures 5.10a and 5.10b). The two higher grains are labeled "1" and "2". Although their height is similar, the average transmission of grain 1 (0.05 %) is ≈20 times lower than the minimum transmission of grain 2 (0.92 %).

It is interesting to discuss the transmission variation across the profile of each grain. Starting from grain "2", it can be noticed that after an initial decrease at the grain edges, the signal increases towards the grain central part (since the gradient is decreasing), to reach a local maximum value at the very center of the grain (minimum gradient). A similar transmission variation is observed as well for the rest of the high grains apparent in figure 5.10b, in the absence of a buried cluster. This observation is in excellent agreement with the discussion in section 5.2.1 concerning the transmission dependence to the surface profile gradient. The transmission in the grain center (1.30 %), is somewhat lower than the image average transmission (1.47 %), a difference

that is approximately equal to the attenuation effect of the additional local thickenss[1].

The transmission behavior is completely different in the case of grain "1". Besides the more intense transmission decrease, the transition is more steep and the signal remains minimum almost throughout the whole grain width. The above results indicate a completely different attenuation mechanism than in the case of grain "2". This behaviour could be explained by the presence of a buried magnetic material cluster. The transmission is quenched as soon as the hot electron beam reaches the edge of the buried cluster. It could be assumed at this point, that the most important contribution to hot electron attenuation in the presence of a buried cluster, is not volume scattering in the cluster, but scattering at the magnetic/nonmagnetic metal interface.

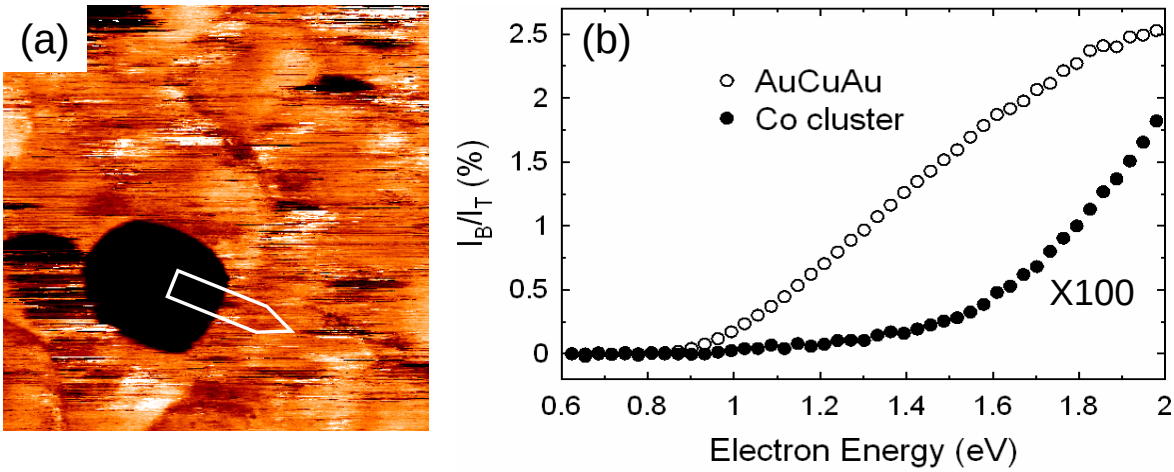

Figure 5.12: (a) Small scan size BEEM image on a buried cluster. The color scale corresponds to transmission from 0.01 % to 2.0 %. Scan size 30×30 nm^2, V_T=1.5 V, I_T=5 nA. (b) Averaged BEEM spectra taken in the absence (empty circles) and in the presence (filled circles) of the buried cluster. In the latter case, the signal is 100 times magnified.

BEEM spectroscopy has been performed to further study the transmission of the buried clusters. Figure 5.12a shows a small scan size BEEM image on a buried cluster. At an electron energy of 1.5 eV, the average transmission is 0.02 % and 1.36 % respectively in the presence and in the absence of the buried cluster. Figure 5.12b shows the averaged spectra taken in each case. The transmission of the Au/Cu/Au/-Si(111) structure is similar to that shown in figure 5.6. The spectral shape is typical for ballistic electron transmission through the metal film, as discussed in chapter 2. The threshold is observed at an energy higher than 0.8 eV, while away from the threshold the transmission variation with energy is quasi-linear.

On the contrary, the transmission variation with energy is markedly different in the

[1] $T_2/T_0 = \exp\frac{-t}{\lambda}$=0.78 where t is the additional local thickness (5 nm) and λ is the attenuation length of Cu (20 nm). The ratio of the measured transmission difference is 0.88.

presence of a buried cluster. First of all, the apparent enormous transmission depression in figure 5.10b, is now observed for the whole energy range, from the threshold up to 2 eV. Moreover, the spectral shape exhibits a higher order dependence to the electron energy, resembling the SBEEM spectra shown in figure 5.5. The latter, and the fact that the collector signal magnitude is comparable to the SBEEM signal, are strong indications that the main contribution to the collector signal is from secondary electrons created in the metal film. The presence of the buried clusters would thus result in complete attenuation of the injected hot electrons, throughout the whole energy range studied. The exact nature of this total scattering source is unknown.

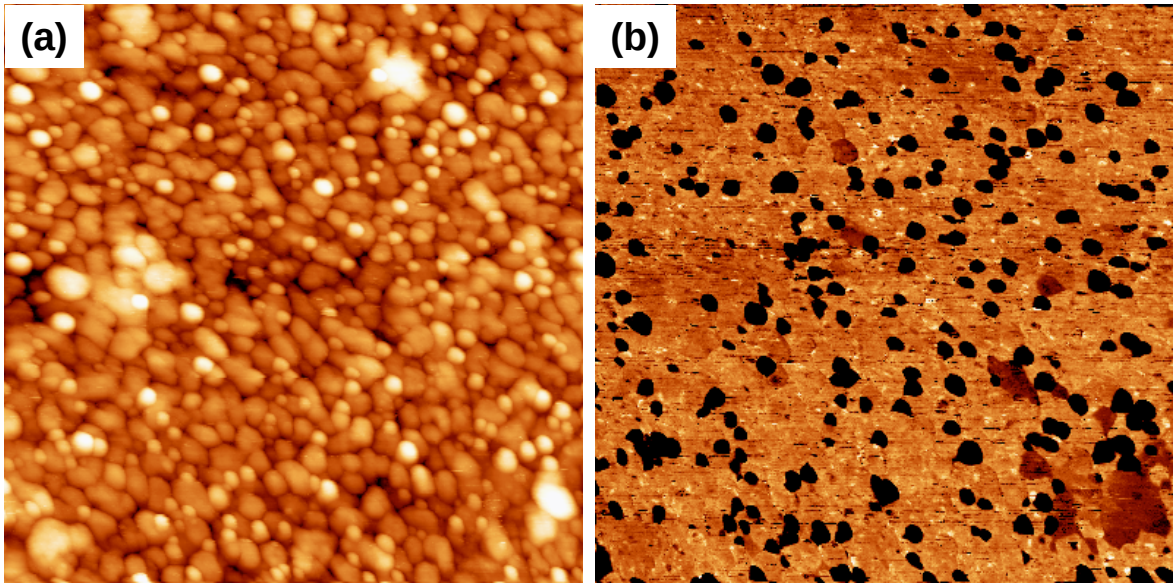

Figure 5.13: BEEM imaging of the Py sample. (a) Topographic signal. The color scale corresponds to height from 0.00 nm to 6.80 nm. (b) BEEM signal. The color scale corresponds to transmission from 0.01 % to 2.0 %. Scan size 200×200 nm^2, V_T=1.5 V, I_T=2 nA.

Similar results were obtained for buried Py clusters. Figure 5.13 shows the topographic and corresponding BEEM images taken on the Py sample. Again, the zones showing intense transmission depressions can be correlated with certain grains apparent in the topographic image. The average transmission is 0.02 % in the presence of a cluster and 1.75 % in the rest of the image. Although the deposition rate and nominal thickness are the same as in sample Co-A, the coverage in this case is higher (206 clusters in a 200×200 nm^2 area), while the average cluster diameter is smaller (5.2 nm). The coverage amounts to 11 %, and the cluster heigth is calculated to be 0.9 nm. This difference is not surprising considering the different nature of the deposited material (see next section).

In both cases discussed above, the transmission measured is extraordinary low at clusters locations. BEEM samples of similar structure containing continuous layers of

Co and Py have been measured, and the results are discussed in section 6.2. Considering the determined hot electron attenuation lengths in Co and Py (see figures 6.9 and 6.10), the transmission measured in the above cases, would correspond to continuous layers of a thickness more than 8 nm. This extremely intense attenuation did unfortunately not find a suitable answer.

5.5.3 Effect of the deposition rate

BEEM imaging of the Co-B sample is shown in figure 5.14. As in the two previous cases, the intense transmission depressions in the BEEM image are attributed to the presence of buried Co clusters. The average transmission is 0.04 % in the presence of a cluster and 1.71 % in the rest of the image. The cluster density (47 clusters in a 200×200 nm^2 area) is lower than in sample Co-A. The average cluster diameter is larger (8.0 nm), in agreement with the coverage increase (8 %). From the latter, the cluster height is calculated to be 2.5 nm. However, as in this case the deposition time was only 2 s (0.2 nm thickness at 0.04 nm/s deposition rate), an increased error on the deposited thickness can not be excluded.

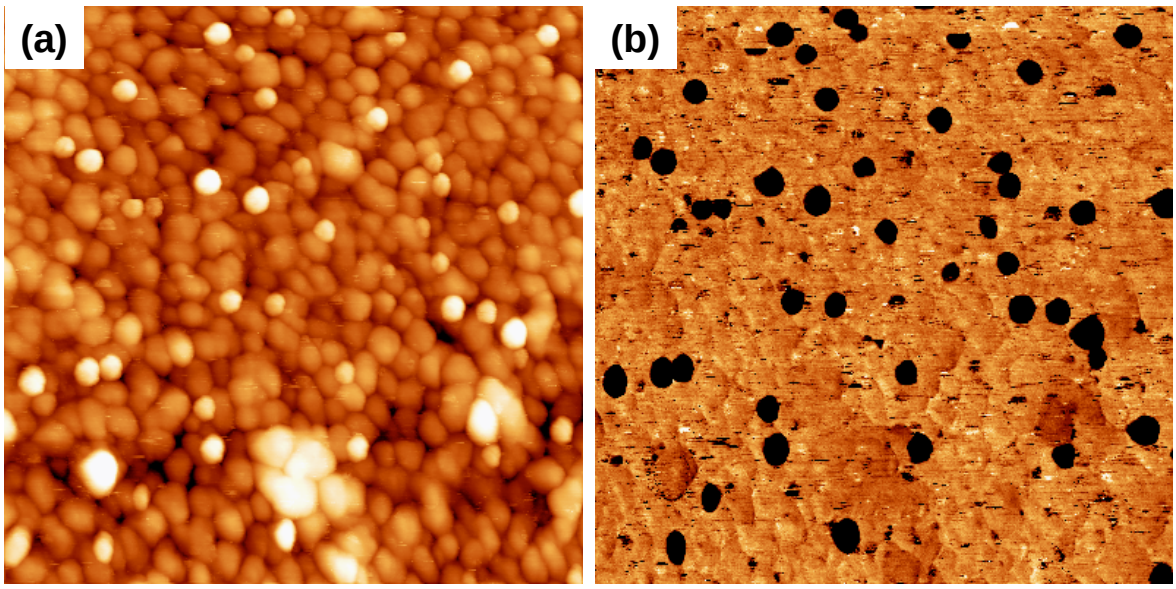

Figure 5.14: BEEM imaging of the Co-B sample. (a) Topographic signal. The color scale corresponds to height from 0.00 nm to 5.15 nm. (b) BEEM signal. The color scale corresponds to transmission from 0.3 % to 2.0 %. Scan size 200×200 nm^2, V_T=1.5 V, I_T=2 nA.

The effect of deposition rate on the cluster size will now be discussed. In the case

of growth on an homogeneous substrate, the cluster density η, is given by

$$\eta \propto \left(\frac{\theta F}{D}\right)^{1/3} \tag{5.1}$$

where θ is the coverage, F is the deposition rate and D is the surface diffusion coefficient [*Rohart*, 2005]. According to this law, the cluster density of sample Co-B should be 3 times higher than the one of sample Co-A. However, it has been shown that the cluster density is in fact lower in sample Co-B. In this case, the non-homogeneous Cu surface should be considered. The diffusion of Co atoms on the Cu surface is limited by surface defects, which is high due to the polycrystalline nature of the films. The measured coverage is roughly 1.8 times higher in the case of sample Co-B, in agreement with the 2 times higher nominal coverage. The cluster density of the Py sample is found to be 2.3 times higher than that of the Co-A sample. This might seem surprising since the deposition rate and substrate were the same. However, as a different material is deposited in each case, different surface diffusion coefficients should be considered, explaining the observed difference.

5.6 BEEM resolution

Although results discussed in section 5.5 remain rather puzzling, the structures observed in the BEEM images provide an excellent object to search for the limits of BEEM resolution. The spatial distribution of the BEEM signal can be quantified, in order to measure the width of the transition zones from high to low transmission. The intense contrast results in an abrupt profile, which is ideal for accurate measurement of the transition width.

As it has been discussed in section 2.3.2, the lateral resolution of BEEM is defined by the opening angle of the acceptance cone (equation 2.11). The resolution is determined by equation 2.13

$$\Delta x = 2d\tan(\theta) \tag{5.2}$$

where θ is the critical angle of the acceptance cone (see figure 5.15a), and d is the thickness of the film.

The configuration of a BEEM experiment in the presence of a buried cluster, is schematically illustrated in figure 5.15a. The main attenuation source is the buried cluster, causing an enormous transmission reduction. The effect begins when the acceptance cone edge reaches the cluster edge. The transmission reaches a minimum when the acceptance cone is totally "masked" by the buried cluster. As it is evident from the figure, the relevant thickness d is equal to the total layer thickness *above* the buried cluster D_1, in this case 4.5 nm (1.5 nm of Cu and 3 nm of Au).

The relation between the film thickness and the resolution Δx, was clearly demonstrated in a recent BEEM study [*Tivarus et al.*, 2005]. Au Schottky contacts on cleaved AlGaAs/GaAs/AlGaAs quantum wells were used as precise nanometer-scale objects. The BEEM resolution was found to decrease (Δx increased) as the layer thickness

increased. In this study, the objects under study were at the metal/semiconductor interface, and thus the whole film thickness was considered.

Figure 5.15b shows the average of line profiles taken in the box indicated in figure 5.12a. This stepped profile is fitted by a hyperbolic tangent function, which is the simplest mathematic form for a step function. The expression used is

$$T = C_T + \Delta T \tanh \frac{x - C_x}{W_0} \tag{5.3}$$

where C_T, ΔT, C_x, and W_0 are constants. The variable x refers to the distance along the transition, and T is the transmission (I_B/I_T) of the sample. The constants C_T and C_x determine the position of the transition zone center. The constant ΔT is equal to 1/2 of the transmission difference between the high and low transmission zones. The values inferred from the fit are: $C_T = 0.608$ %, $\Delta T = 0.594$ % and $C_x = 3.208$ nm.

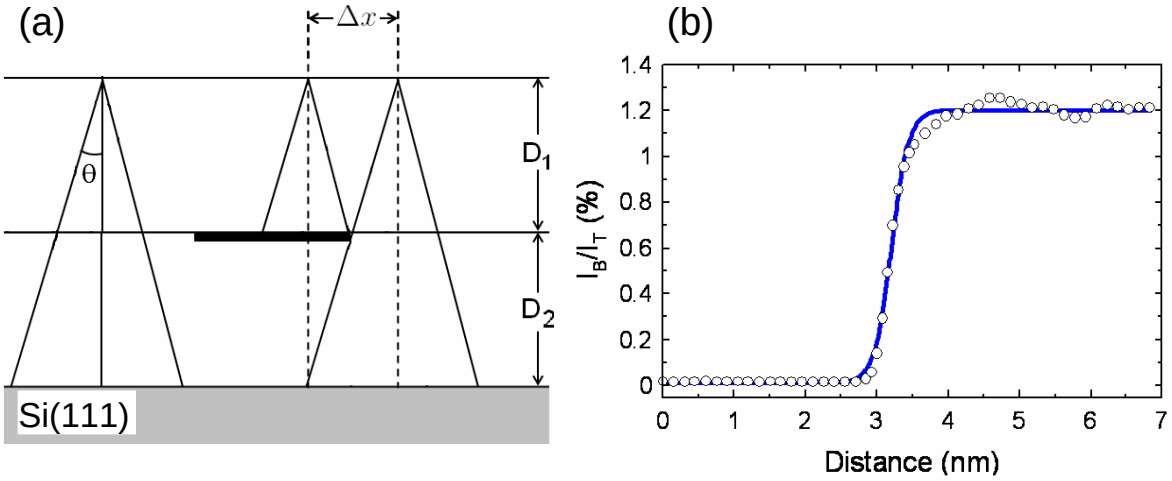

Figure 5.15: (a) Schematic representation (not in scale) of the resolution determination method (see text). The black rectangle indicates the presence of a buried cluster. (b) Average of line profiles taken in the box indicated in figure 5.12a. The solid line correspond to a hyperbolic tangent fit to the data.

The constant W_0 is proportional to the transition zone width W. Since this is the observed feature with the minimum width, it is considered to be equal to the BEEM lateral resolution, Δx. By defining Δx as the distance where the transmission is increasing from 10 % to 90 % of the maximum value, then $\Delta x = 2.24 \times W_0$. The value $W_0 = 0.238 \pm 0.022$ is inferred from the fitting process, and the resolution is determined to be $\Delta x = 0.533 \pm 0.05$ nm.

The image of figure 5.12a was taken at an electron energy of 1.5 eV. Considering the m^* and Φ_B values for the Au/Si(111) system (section 2.3.2), the critical angle θ is calculated to be 9°. As noted before, the relevant thickness D_1 is 4.5 nm. The expected resolution is calculated to be 1.4 nm, a value much higher than the observed

one. Those results are in agreement with a previous BEEM study of Au/Si(111) structures [*Milliken et al.*, 1992]. In this case, a SiO_2 layer at the Au/Si interface was patterned to form transmitting and non-transmitting regions. By analyzing the transmission profiles at the boundaries of these regions, the spatial BEEM resolution was measured. For a Au layer thickness of 15 nm, and electron energy 1.5 eV, the resolution measured was 1 nm, much lower than the calculated value (4.7 nm). It should be noted that the calculation of the acceptance cone angle, was performed in the free electron approximation. This disagreement between experiment and theory, is probably due to the effect of the electronic band structure of the metal layers, which is not negligible.

5.7 Conclusion

The measurements discussed in this chapter demonstrate the ability of our setup to perform BEEM spectroscopy and imaging. The sample fabrication method discussed in chapter 4 was shown to be adequate for such measurements, fulfilling all the necessary requirements.

Going further than the reproduction of already performed experiments, new results were obtained. Although it has been two decades since BEEM was first introduced as technique for *"...investigation and imaging of subsurface interface electronic structure..."* [*Kaiser and Bell*, 1988], the study of the Cu/Si(n-type) interface was performed for the first time during this work. For the measurement of the corresponding Schottky barrier height, a simple method for fabricating extremely low area metal/semiconductor contacts was developed.

In a different kind of experiments, samples containing Co and Py in sub-monolayer coverages were studied. Their presence is revealed by BEEM imaging due to the enhanced hot electrons attenuation in the presence of magnetic material. Although this work is not completely original [*Rippard and Buhrman*, 2000], the present results are quite different than those reported earlier. In fact, an adequate explanation is still lacking, and further investigation is necessary in order to clarify all the discussed issues. By using these buried structures as objects resulting in high transmission differences (high contrast), the BEEM resolution of our microscope was determined, and it was found to be less than 1 nm.

Finally, non-magnetic metallic (multi)layer structures on Si(111) were studied. The hot electron transmission through Au layers and Au/Cu/Au trilayers and the Au/Cu interface was measured, a necessary information since such layers are present as well in the magnetic multilayer samples (chapter 6). Several Au/Si samples were measured, and the Schottky barrier height was found to be in excess of 0.8 eV in all cases. This metal/semiconductor interface was verified by BEEM imaging to be homogeneous, thus allowing the measurement of the more subtle contrast variations originating from spin-dependent scattering (see section 6.3).

Chapter 6

Spin-dependent transport and magnetic imaging

6.1 Introduction

In this chapter, spectroscopy and microscopy studies on magnetic BEEM samples are presented. In the first part, spin-dependent transport in magnetic multilayers is studied. Samples containing non-magnetic (Au and Cu) and magnetic (Co and Py) layers were measured. As outlined in section 2.4, the electron spin has to be considered when studying hot electron transport in magnetic materials. BEEM has been used as a local probe to study spin-dependent hot electron transport in Co and Py layers, in the energy range 1-2 eV above the Fermi level. BEEM spectroscopy measurements on single magnetic layer and spin-valve samples, allow the determination of the majority and minority hot electron attenuation length in the materials studied.

The main objective when developing a ballistic electron microscope was to perform magnetic imaging of thin films. In the second part of this chapter, high resolution imaging of magnetic domains and domain walls in Co/Cu/Py and Co/Cu/Co planar magnetization spin-valves is demonstrated. The case of 360° domain walls in Co films is presented in detail, and the magnetic contrast is compared to micromagnetic calculations. The effect of the applied field on the structure of the domain wall is studied and an upper bound of the resolution of BEEM magnetic imaging is discussed.

6.2 Spin-dependent hot electron transport

6.2.1 Basic framework

The main principle of the model used, is the asymmetry between the attenuation length (λ) of hot majority-spin and minority-spin electrons, in the ferromagnetic layer. The source of this asymmetry has been discussed in section 2.4. In the following, the attenuation lengths of hot majority-spin and minority-spin electrons are labeled λ_M,

and λ_m, respectively.

Transmission through single ferromagnetic layers

The simplest spin-dependent transport BEEM study, concerns the measurement of samples containing a single ferromagnetic (FM) layer. The full sample stack is Au(3)/-Cu(1.5)/FM(t)/Cu(1.5)/Au(7)/Si(111), where the numbers in brackets indicate the layer thickness in nm. Hot electron attenuation phenomena in the Au, Cu and FM layers, and at the Au/Cu, Cu/FM, and Au/Si interfaces all contribute to the transmission measured. Since hot electron transport in a FM layer is involved, the hot electron transmission through the metal/Si structure is given by equation 2.19

$$T(E) = T_0(E)\left[\frac{1}{2}\exp\left(-\frac{t}{\lambda_M(E)}\right) + \frac{1}{2}\exp\left(-\frac{t}{\lambda_m(E)}\right)\right] \tag{6.1}$$

where T_0 is the energy dependent transmission of the total of the Au and Cu layers, including the Au/Cu, Au/Si, and Co/Cu interfaces. The quantity in brackets describes the spin-dependent hot electron transport in the FM layer. The parameters λ_M and λ_m are material-dependent, while the thickness t is sample dependent. The hot electrons injected from the STM tip into the Au/Cu capping bilayer and then into the FM layer are not spin polarized, so that two initially equal spin populations are considered [*Heer et al.*, 2004]. As the quantity T_0 does not change from sample to sample, it is possible to distinguish and study the attenuation of hot electrons in the FM layer, by measuring samples with various FM layer thicknesses.

Transmission through spin-valves

More elaborate spin-dependent transport BEEM experiments, can be performed using samples containing spin-valves. As discussed in section 6.3, BEEM microscopy measurements of spin-valve samples, allow the imaging of magnetic structures. The full sample stack is the same as before, but instead of a single FM layer, a spin-valve is grown. The interest in this case, is to measure the sample transmission in the parallel (P) and anti-parallel (AP) magnetic configurations of the spin-valve.

The generalized case of a spin-valve containing two FM layers of different material and different thickness, is considered below. The FM layer A (λ_M^A and λ_m^A) of thickness t_A and the FM layer B (λ_M^B and λ_m^B) of thickness t_B, are considered. The transmission is calculated for two distinct cases depending on the relative magnetization orientation of the two FM layers. For P alignment, majority (minority) electrons in the first layer are majority (minority) electrons as well in the second layer. In this case the sample transmission is given by equation

$$T_P = T_0'\left[\frac{1}{2}\exp\left(-\frac{t_A}{\lambda_M^A}\right)\exp\left(-\frac{t_B}{\lambda_M^B}\right) + \frac{1}{2}\exp\left(-\frac{t_A}{\lambda_m^A}\right)\exp\left(-\frac{t_B}{\lambda_m^B}\right)\right]. \tag{6.2}$$

Equal attenuation lengths for each spin population are considered in the Cu spacer. Thus, the polarization of the hot electron beam after transport through the first FM

layer, will remains constant in the spacer. The attenuation due to the Cu spacer is included in T_0' [$T_0' = T_0 \exp(-t_{Cu}/\lambda_{Cu})$].

For AP alignment, the majority (minority) electrons in the first layer are minority (majority) electrons in the second layer, so that the transmission of the sample is

$$T_{AP} = T_0' \left[\frac{1}{2} \exp\left(-\frac{t_A}{\lambda_M^A}\right) \exp\left(-\frac{t_B}{\lambda_m^B}\right) + \frac{1}{2} \exp\left(-\frac{t_A}{\lambda_m^A}\right) \exp\left(-\frac{t_B}{\lambda_M^B}\right) \right]. \qquad (6.3)$$

The meaning of relations 6.2 and 6.3 is depicted in figures 6.1 and 6.2. The transmission of the majority and minority carriers is calculated and plotted in the case of P and AP alignment of the two FM layers. The hot electron current polarization is also shown in each case. The structure considered is the Co(1.8)/Cu(6)/Py(1.6) spin-valve studied in section 6.2.2. The λ_M and λ_m values used for transport in Co and Py, are those determined in section 6.2.4 for a 1.5 eV injection energy. The attenuation length in Au and Cu is considered to be equal for both spin populations, and it is the same for both materials (see section 4.6.1). The transmission of each Au/Cu interface is 70 % (see section 5.3). A 25 % transmission is considered at the FM/Cu interface before the metal/semiconductor interface (according to the discussion in section 6.2.3).

In figure 6.1 the case of P alignment of the two FM layers is shown. An initial transmission decrease occurs due to the transport through the Au/Cu capping layer. The hot electron beam is polarized during transport in the first FM layer (the Py layer in this case), as the two spin populations are attenuated at a different rate. Next,

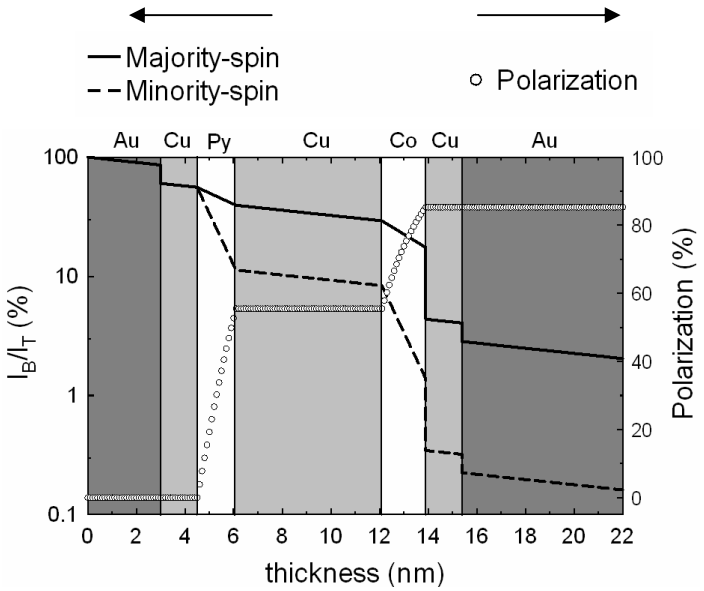

Figure 6.1: Spin-dependent hot electron transmission and hot electron polarization, for a P configuration of the spin-valve.

the polarization remains constant and the transmission is decreased during transport

through the Cu spacer. The polarized beam is analyzed in the second FM layer (the Co layer). For P alignment, the attenuation asymmetry results in an enhancement of the hot electron beam polarization. Finally, after significant transmission decrease at the FM/Cu interface, the hot electron current is further attenuated during transport through the remaining Cu/Au layers. The total transmission is equal to the sum of the majority and minority electron transmissions. It should be noted, that energy and momentum filtering at the metal/semiconductor interface are not considered here, resulting in higher transmission as compared to the measured value (see section 6.2.2). For the specific structure considered, a strongly (≈85 %) majority-spin polarized hot electron current exits the full stack.

The case of an AP alignment of the two FM layers is illustrated in figure 6.2. As in the previous case, the hot electron beam is first attenuated in the Au/Cu bilayer. After

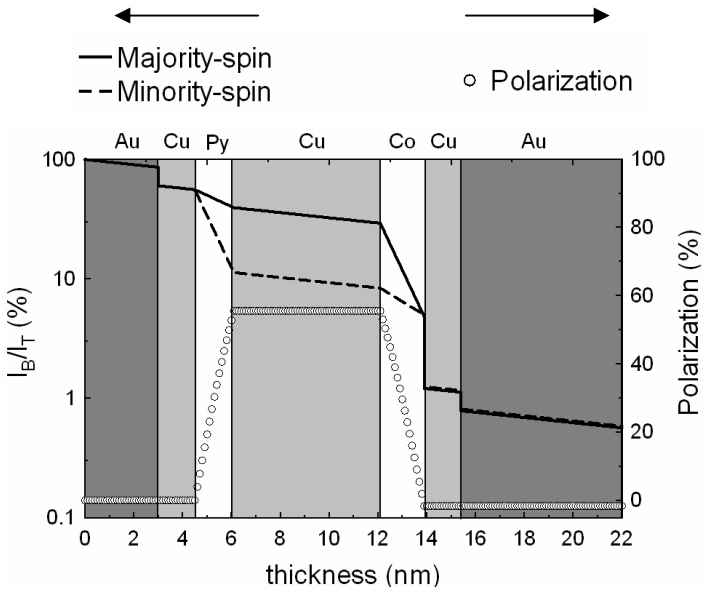

Figure 6.2: Spin-dependent hot electron transmission and hot electron polarization, for an AP configuration of the spin-valve.

transport through the Py layer, the electron beam becomes majority-spin polarized, with a magnitude identical to that of the P state. Additional attenuation occurs in the Cu spacer. During transport in the Co layer, in contrast to the previous case, the majority (minority) electrons in the first FM layer, are minority (majority) electrons in the second FM layer. The highly attenuated minority electron beam in the Py layer, will now suffer less attenuation. On the contrary, the initial majority electron beam, will now be highly attenuated. This process compensates the imbalance between the two spin populations, de-polarizing the hot electron beam. In fact, for the spin-valve studied, due to differences between the two layers in the thickness and λ_M, after transport through the Co layer, the hot electron beam is slightly (1.7 %) minority-

spin polarized. Moreover, the total hot electron transmission in this case is lower than before (note that the transmission axis is logarithmic).

The case described above corresponds to the most complex structure. In the simpler case where two FM layers of the same material and same thickness are used, equation 6.2 reduces to

$$T_P = T_0' \left[\frac{1}{2} \exp\left(-\frac{2t}{\lambda_M}\right) + \frac{1}{2} \exp\left(-\frac{2t}{\lambda_m}\right) \right]. \tag{6.4}$$

and equation 6.3 is reduced to

$$T_{AP} = T_0' \exp\left(-\frac{t}{\lambda_M}\right) \exp\left(-\frac{t}{\lambda_m}\right). \tag{6.5}$$

Optimization of the magnetic layer thicknesses

In this section, the optimum magnetic layer thicknesses of the spin valve samples for a BEEM experiment are calculated. The equations discussed in the previous section and the attenuation lengths determined in the experiments (section 6.2.4) at 1.5 eV (λ_M^{Co}= 3.24 nm, λ_m^{Co}= 1.00 nm, λ_M^{Py}= 5.78 nm, λ_m^{Py}= 1.00 nm) are used.

First, the relative thicknesses of the two layers at a given total magnetic layer thickness, are calculated for maximum magnetic contrast (as defined in equation 6.6). The cases of spin valves with two Co layers and with one Co and one Py layers are discussed. The variation of the contrast is shown in figure 6.3 for different total thicknesses.

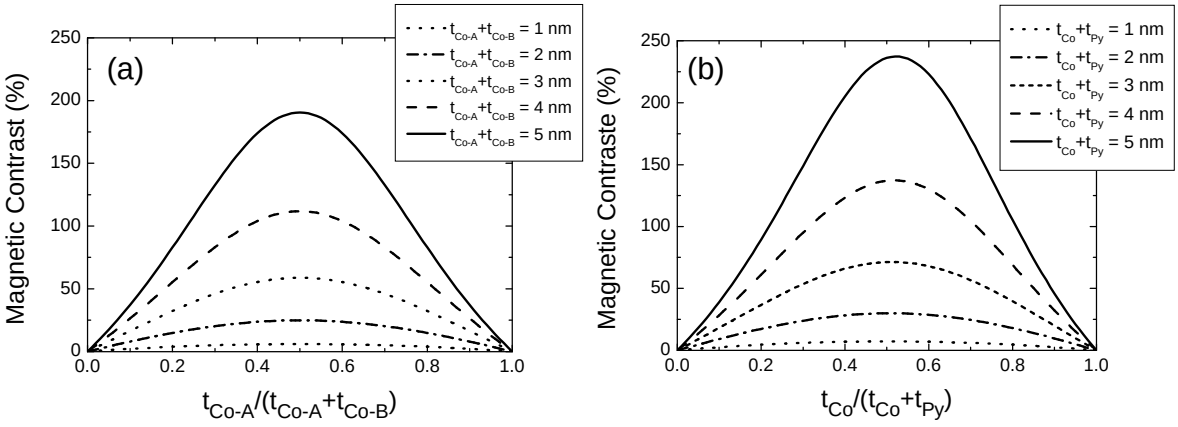

Figure 6.3: Variation of the magnetic contrast, as a function of the relative thicknesses of the two magnetic layers of the spin-valve, for a given total magnetic layer thickness. (a) Co/Cu/Co and (b) Co/Cu/Py spin-valves.

In the case of only one type of material, as a general result, it is obtained that the maximum contrast is reached for the same thickness of the two layers, whatever the total thickness. This result has already been observed in reference [*Rippard and Buhrman*, 2000]. In the case of a spin valve with two materials, the highest contrast

is reached with a slightly higher thickness in Py, which has the largest λ_M/λ_m ratio. However the difference between the two thicknesses is weak ($t_{Py}/(t_{Co}+t_{Py}) = 0.52$).

As a second step, considering the fixed thickness proportion determined before, the optimum total thickness for maximum parallel and antiparallel current difference is calculated. This is shown in figure 6.4.

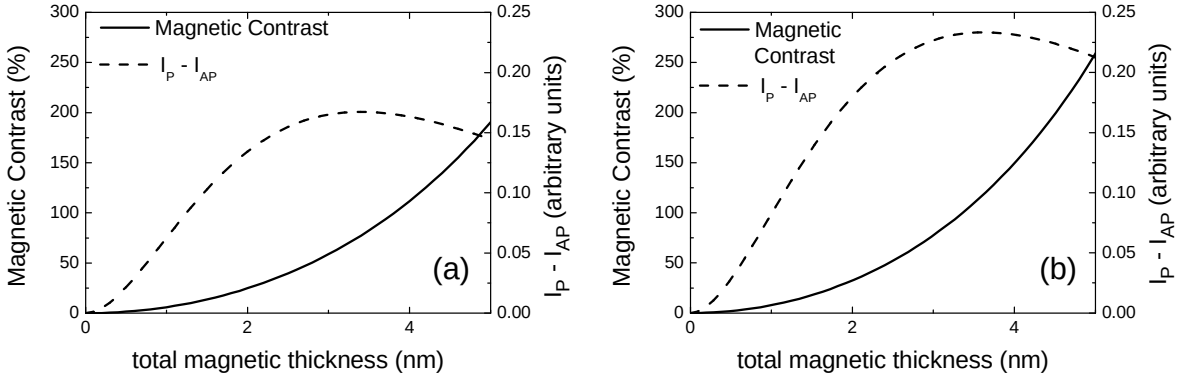

Figure 6.4: Optimization of the total magnetic layer thickness for maximum parallel and antiparallel current difference. (a) Co/Cu/Co and (b) Co/Cu/Py spin-valves.

The contrast always increases with the total thickness. Indeed, the thicker a layer is, the higher the polarization of the hot electron current at the exit of the layer. This gives rise to an infinite contrast for infinite thicknesses (note that this effect shows that the contrast in BEEM is scalable contrary to GMR; it explains the very high value of 600 % at room temperature [*Heer et al.*, 2004] that can be found in the literature). However for these high thicknesses, the total current decreases dramatically and may become undetectable. As a consequence we prefer to optimize the difference between the current in parallel and antiparallel states as shown in figure 6.4. This difference reaches a maximum around 3-4 nm, which represents the optimum total thickness for BEEM imaging. Following this, the optimum sample for BEEM images contains two 1.8 nm thick layers of Co or Py.

6.2.2 Spin-dependent hot electron attenuation lengths in Co and Py

Majority electron attenuation length

As shown in this section, it is possible to determine the majority electron attenuation length by studying the transmission through stacks containing a single FM layer. Samples with Co or Py single FM layers with various thicknesses were measured. Figure 6.5 shows the corresponding spectroscopy curves. More than 100 spectra taken at points within several 0.5×0.5 μm^2 scanning areas were averaged in each case. It is clear that, in both cases, transmission is decreasing with increasing FM layer thickness. As

the rest of the sample stack is always the same, the source of this effect necessarily originates from the FM layer (section 6.2.1).

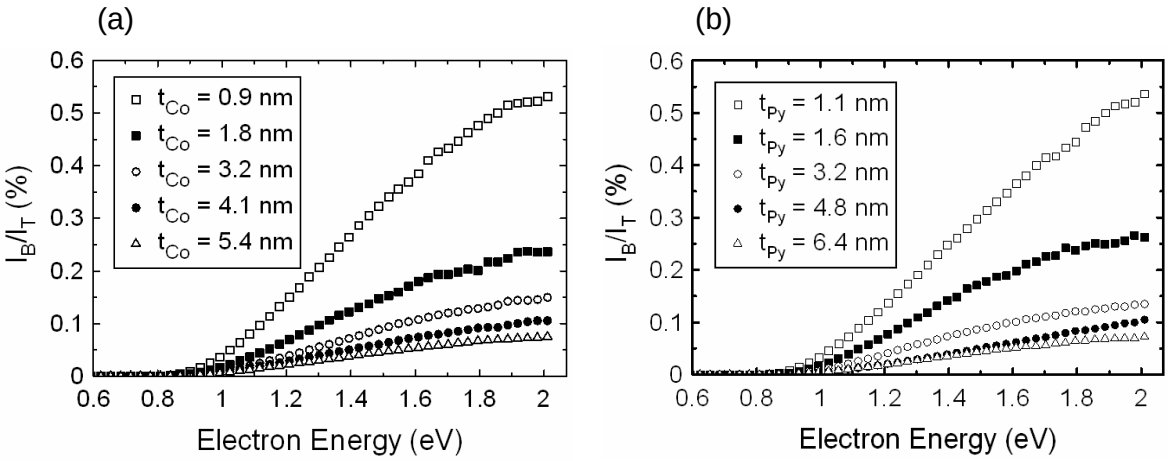

Figure 6.5: Hot electron transmission ($T = I_B/I_T$) versus electron energy for single Co (a) and Py (b) layers with various thicknesses (t). Injection current I_T=50 nA. The error bars are have been removed for clarity.

In figure 6.6 the logarithm of the transmission at 1.5 eV for the FM single layer samples is plotted as a function of the FM layer thickness (similar graphs were obtained in the whole 1 - 2 eV range). As a function of the thickness, two regimes are observed with different slopes: in the low FM layer thickness regime the transmission is decreasing faster than in the higher thickness regime.

As the minority electron attenuation length is much shorter than the majority one (≈1 nm for both Co [*Rippard and Buhrman*, 2000] and Py [*van Dijken et al.*, 2002]), after transport through a distance equal to a few minority attenuation lengths, minority electrons have been almost totally scattered and the ballistic current contains almost only majority electrons[1]. Then, for $t > 3$ nm, the second exponential decay (corresponding to the minority electrons) can be neglected in equation 6.1, whereas the complete equation has to be used in order to fit all experimental data. A linear fit to the data of figure 6.6 for the high FM layer thickness regime gives the value of the majority hot electron attenuation length (3.3 nm for Co and 4.7 nm for Py at 1.5 eV, see figures 6.9 and 6.10). In principle, the whole thickness range could be fitted according to equation 6.1 in order to directly determine both λ_{maj} and λ_{min}. However, the lack of experimental data in the low thickness regime, makes this fitting process unreliable for the determination of λ_{min}.

Minority electron attenuation length

In order to determine λ_{min}, the hot electron transmission through spin-valve samples was measured as a function of the relative magnetization orientation of the two FM

[1]This *spin-filter* effect has been discussed in section 2.4.2 (see also figure 2.16)

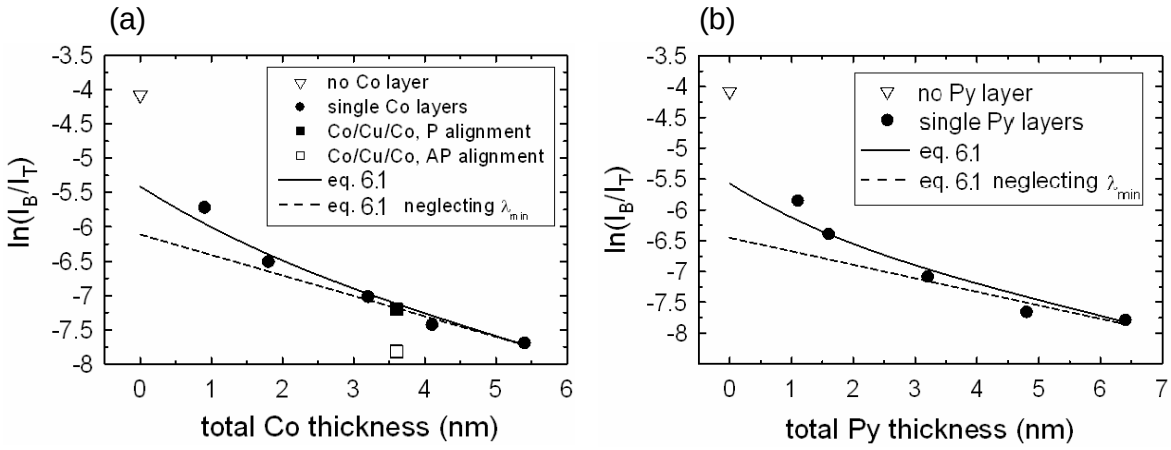

Figure 6.6: Logarithm of the transmission versus total FM thickness for samples with Co (a) and Py (b) single layers (discs) at 1.5 eV. The transmission of a reference sample with no FM layer is indicated by a down triangle. In (a), the transmission of a Co/Cu/Co spin-valve sample is indicated for parallel (P: full square) and anti-parallel (AP: open square) alignment of the two Co layers. The dashed line is a linear fit to the data for FM thicknesses higher than 3 nm. The continuous lines corresponds to equation 6.1 using the λ_{maj} and λ_{min} values determined in the following.

layers. The sample stack is the same as before, but instead of a single FM layer, a Co(1.8)/Cu(6)/Co(1.8) or a Co(1.8)/Cu(6)/Py(1.6) spin-valve is grown.

By making use of the imaging capabilities of BEEM, the P and AP aligned zones of the spin-valve can be distinguished in zero field thanks to the presence of domains in both layers (see section 6.3). Figure 6.7 shows the BEEM spectra taken on the Co/Cu/Co (a) and the Co/Cu/Py (b) spin-valves. Each curve is an average of more than 100 spectra taken within several 0.5 $\times$0.5 μm^2 scanning areas. The sample transmission in the P state is systematically higher than the transmission in the AP state. The error bars correspond to the standard deviation of the measurement, and they mainly indicate the local variations of transmission because of the surface structure (see chapter 5).

By analogy to equation 2.20, the magnetic contrast (MC) is defined as

$$\mathrm{MC} = \frac{T_P - T_{AP}}{T_{AP}}. \tag{6.6}$$

and is found to decrease with electron energy, in accordance with previous studies [*Haq et al.*, 2006]. In the case of Co/Cu/Co, the MC is decreasing from more than 200% just below 1.0 eV, to 50% at 2.0 eV. The MC is lower in the case of Co/Cu/Py, and it decreases from 150% just below 1.0 eV, to 50% at 2.0 eV. This difference in MC between the two samples is expected, since the lower thickness of the Py layer (polarizer) results in a lower polarization of the transmitted electron beam. Although the MC is decreasing, the absolute difference in transmission between the P and AP

states is increasing with energy, providing a higher MC signal to noise (s/n) ratio. However, for high injection energy the surface corrugation leads to overlapping error bars, decreasing the s/n ratio. The optimum injection energy lies roughly in the 1.4-1.6 eV range.

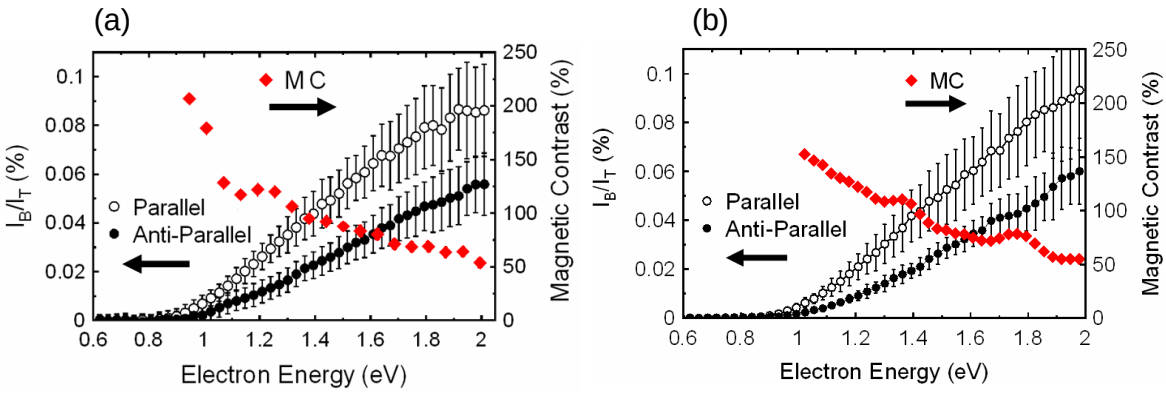

Figure 6.7: Hot electron transmission (I_B/I_T) versus injection energy for the Co/Cu/Co (a) and Co/Cu/Py (b) spin-valves measured for parallel (P) and anti-parallel (AP) alignment of the two FM layers. Injection current I_T=50 nA.

Note that although the sample transmission is due to the metal layers and metal/semiconductor interface, the magnetic contrast is only determined by the spin-dependent scattering occurring in the two FM layers. The MC value can be calculated by the transmission of the spin-valve in the P and AP configurations. In the case of the Co/Cu/Py spin-valve, the sample transmission in the P and AP configurations is given respectively by equations 6.2 and 6.3. In the case of the Co/Cu/Co spin-valve, where the two Co layers have equal thickness, the sample transmission in the P and AP configurations is given respectively by equations 6.4 and 6.5. Thus, taking into account the λ_M value determined from the single FM layer samples, λ_m can be deduced from the magnetic contrast. The fact that the MC value is decreasing with energy, indicates that there is a significant energy dependence of λ_M and λ_m.

6.2.3 Hot electron scattering at the magnetic/nonmagnetic interfaces

In the model described in section 6.2.1, spin-dependent scattering is considered only in the volume of the magnetic films. Although the origin of the giant magnetoresistance effect for Fermi level electron transport was found to arise mainly from spin-dependent scattering at the magnetic/nonmagnetic interfaces [*Parkin*, 1993], this is not the case for hot electron transport. Experiments performed using MTT devices containing spin-valves with Au or Cu spacers, have shown that the hot electron magnetocurrent was the same whether Au/FM or Cu/FM interfaces were present [*van Dijken et al.*, 2003]. Some weak spin-dependent interface scattering cannot be excluded, as was shown by a

SVT study using devices containing Co/Au/Py spin-valves [*Vlutters et al.*, 2002], but it is not considered here.

Although spin-dependent scattering is not assumed to occur at the FM/Cu interfaces, a significant contribution is added to the overall scattering. The linear fit to the data for high layer thicknesses (figure 6.6), is used to determine T_0. The intercept of the regression line with the y-axis is equal to $\mathrm{Ln}(T_0/2)$, since in this thickness regime only majority electron transport is considered. The T_0 value is compared to the transmission T_{REF} of a reference sample with no FM layer, and thus no FM/Cu interfaces (down triangle in figure 6.6). As shown in figure 6.8, T_0 is found to be in both cases $\approx$4 times smaller than the transmission of the reference sample. This indicates strong scattering at the FM/Cu interfaces. Somewhat higher scattering is found at the Py/Cu interface than at the Co/Cu interface. Since Py is an alloy, a more disordered interface and higher attenuation are anticipated. The T_0 value was determined in the whole energy range studied. Figure 6.8 shows the variation of the ratio T_0/T_{REF} with the electron energy. Within the determination error ($\approx$10 %), no energy dependence of the FM/Cu interface attenuation is observed.

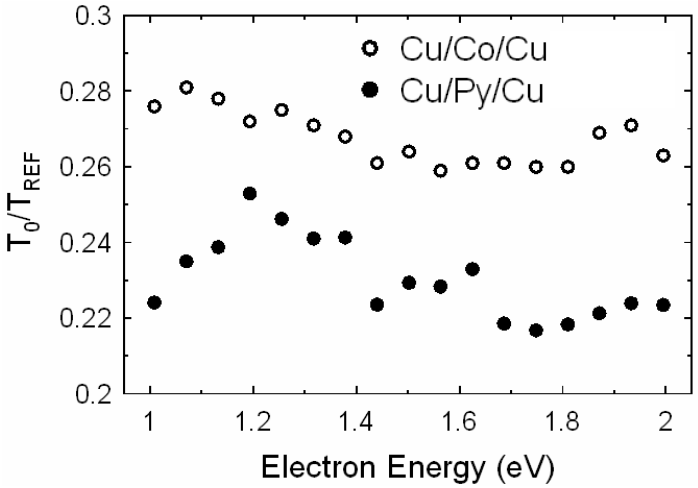

Figure 6.8: Variation of the ratio T_0/T_{REF} with electron energy for the Cu/Co/Cu and Cu/Py/Cu samples.

Figure 6.6a, includes transmission data of a Co/Cu/Co spin valve sample (see also figure 6.7a). The total Co layer thickness is considered, while the transmission for parallel (P) and anti-parallel (AP) alignment of the two Co layers is indicated. The attenuation effect of the extra Cu spacer was calculated using an attenuation length in Cu comparable to that of Au, (20 nm in this case, see section 5.3), and subtracted from the experimental data. The value for P alignment is in agreement with the single layer samples, only considering two interfaces as already reported [*Rippard and Buhrman*, 2000].

The origin of this interface scattering is not clearly understood. Since no energy

dependence was found, elastic scattering due to defects and roughness at the interface appears more likely than a pure band structure effect. As proposed in reference [*Rippard and Buhrman*, 2000], the absence of any effect of the second pair of Co/Cu interfaces, may arise from a momentum filtering effect at the first Cu/Co interface. The presence of additional interfaces has little effect on the ballistic electrons whose momentum distribution has been filtered by the first interface.

Another explanation may arise from the Si diffusion issue described in section 4.6. A possible Si atom diffusion through the Au/Cu bilayer up to the Co layer, would lead to the formation of a non-magnetic Co-silicide layer. In section 4.6, a nominally 4 monolayer thick Cu encapsulated Co layer was shown to exhibit ferromagnetic behavior. Thus, this Co-silicide layer, if present, is not expected to be thicker than a few monolayers. However, it may add a significant contribution to hot electron scattering. The 75 % attenuation can even be solely attributed to this layer, while total transmission would then considered for the Co/Cu interfaces.

6.2.4 Energy dependence of the attenuation lengths

Hot electron attenuation lengths in Co

Figure 6.9a shows the values determined for the majority and minority hot electron attenuation lengths in the energy range 1.0 to 2.0 eV above the Fermi level. There is indeed an important energy dependence. λ_M is decreasing from 5.2 to 3.3 nm in the range 1.0 to 1.5 eV and then remains relatively constant. On the contrary, λ_m is increasing from 0.9 to 1.2 nm throughout the whole energy range. The ratio of the two values (figure 6.9b) is decreasing continuously from 6 to 3 in the 1.0-2.0 eV, explaining the decrease in MC measured for the spin-valve sample (figure 6.7a).

The variation of λ_M with energy determined here, differs from these reported before. BEEM measurements performed at room temperature [*Rippard and Buhrman*, 2000], and at 150 K [*Jansen et al.*, 2007] are now discussed. In the first case, λ_M was found to remain relatively constant ($\approx$2.2 nm) in the 1.0-1.3 eV energy range, and then to decrease slowly down to 2 nm in the 1.3-2.0 eV range. In the second case, a constant value ($\approx$3.5 nm) was found in the 1.0-1.5 eV. The higher value of λ_M in reference [*Jansen et al.*, 2007] with respect to reference [*Rippard and Buhrman*, 2000], is probably due to reduced phonon scattering. Although this process is quasi-elastic, it affects the momentum distribution which is important for BEEM experiments (see section 2.3.2).

It should be noted, that in reference [*Jansen et al.*, 2007] the λ_M is also determined by MTT experiments. Although that as well almost no variation with energy is observed in the 1.0-1.4 eV range, the value measured is considerably higher ($\approx$6.8 nm). This is explained on the basis of a more isotropic tunnel momentum distribution for the Al_2O_3 barrier used. Then, elastic scattering in the Co base has little further effect and does not contribute to the attenuation (see section 2.3.2 and equation 2.10).

The energy dependence of λ_m shown in figure 6.9 is quite similar to the variation

found in reference [*Rippard and Buhrman*, 2000]. In both cases the value is increasing throughout the 1.0-2.0 eV energy range. Again, the values determined here (0.9 nm to 1.2 nm) are somewhat higher than in reference [*Rippard and Buhrman*, 2000] (0.7 nm to 0.9 nm).

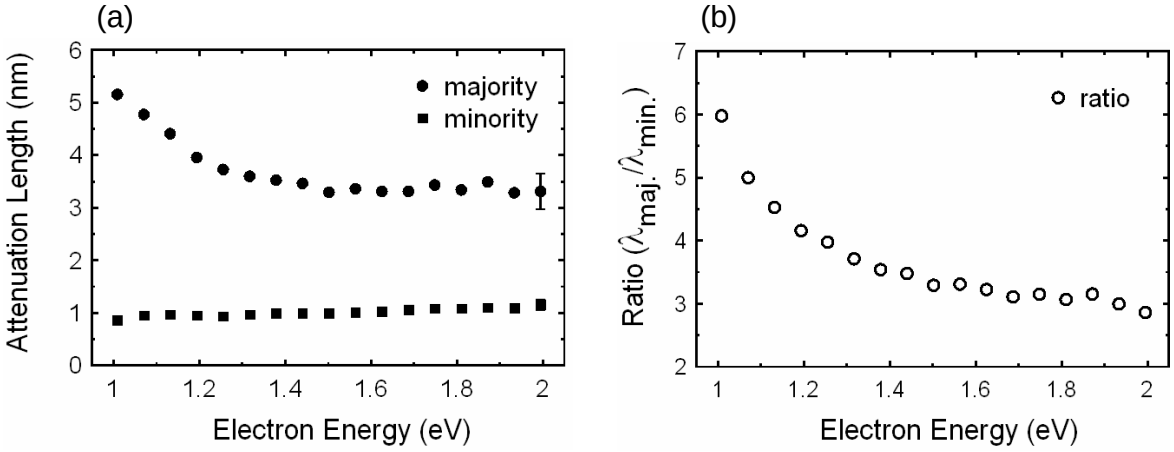

Figure 6.9: (a) Hot electron attenuation length for majority and minority electrons in Co at room temperature, as a function of electron energy. The error on the determination of the attenuation length is ≈10 % as indicated at the last point. (b) λ_M/λ_m ratio.

Hot electron attenuation lengths in Py

Figure 6.10a shows the values determined for the majority and minority hot electron attenuation lengths in the energy range 1.0 to 2.0 eV above the Fermi level. The variation of λ_M with energy is quite different than in the case of Co. While there is a minor decrease from 4.8 to 4.2 nm in the 1.0-1.2 eV range, the value for higher energies increases up to 5.1 nm at 2.0 eV. The variation of λ_m with energy is similar to that found in the case of Co. The λ_m value is increasing from 0.8 nm to 1.2 nm in the 1.0-2.0 eV energy range. Similarly to the Co case, the ratio of the two values is decreasing continuously from 6 to 4 in the 1.0-2.0 eV range, in agreement with the MC value decrease (figure 6.7b).

The λ_M variation versus energy, is in contradiction with results obtained from MTT experiments. In the latter case, a clear decrease of the λ_M value was found from 8.0 to 6.0 nm in the 1.0-1.8 eV range [*van Dijken et al.*, 2002]. The λ_M value measured is much higher than shown in figure 6.10a. However, since BEEM and MTT experiments are compared, the effect of the tunnel barrier discussed before should be considered, since in the case of reference [*van Dijken et al.*, 2002] a Al_2O_3 barrier is used.

λ_M in Py has been also measured from SVT experiments [*Vlutters et al.*, 2002]. The value 4.3 nm found at 0.9 eV injection energy, is closer to the values determined here. In this case, it can be assumed that the Schottky barrier used injects a more

forward focus hot electron beam than the Al_2O_3 tunnel barrier. Thus, both elastic and inelastic effects contribute to the attenuation.

In reference [*van Dijken et al.*, 2002], the λ_m value was found to be constant in the energy range studied, in contrast to the dependence shown in figure 6.10a. However, the values determined in both case are similar (≈1 nm), and in agreement with the value determined in reference [*Vlutters et al.*, 2002].

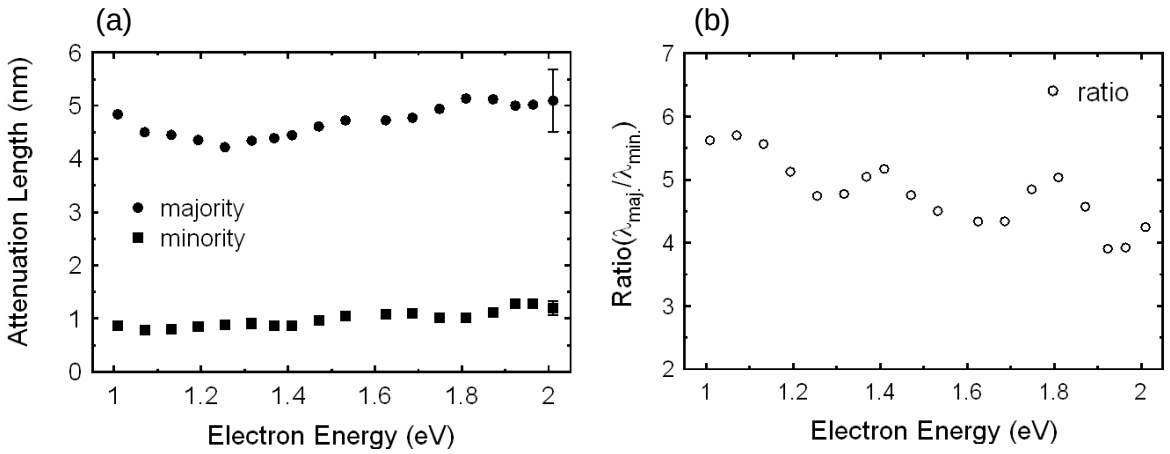

Figure 6.10: (a) Hot electron attenuation length for majority and minority electrons in Py at room temperature, as a function of electron energy. The error on the determination of the attenuation length is ≈13 % as indicated at the last point. (b) λ_M/λ_m ratio.

Discussion

As discussed in chapter 2, the main mechanism of hot electron energy loss, is electron-electron scattering. Here, the interaction between the hot electron and an electron below the Fermi level is considered as the only contribution to the inelastic hot electron attenuation length (λ_i=λ_{e-e}). The interaction with defects is an elastic scattering process, giving rise to the elastic hot electron attenuation length (λ_e=λ_{e-def}). The two scattering mechanisms combine as indicated in equation 2.10: $1/\lambda = 1/\lambda_{e-e}+1/\lambda_{e-def}$. The length λ_{e-e} is intrinsic to the material band structure, and thus can be attained from first principles calculations [*Chulkov et al.*, 2006; *Zhukov et al.*, 2004; *Zhukov et al.*, 2006]. On the other hand, λ_{e-def} depends on the quality of the material and since it is an elastic interaction, it is not expected to vary with energy [*Chulkov et al.*, 2006]. If λ_{e-e} is longer than λ_{e-def}, then defects dominate λ, which becomes essentially constant. The above, could explain why the attenuation length and its energy dependence can change from a source of samples to another.

In the case of Co, the clear λ_M variation with energy, potentially indicates that λ_{e-def} is longer than λ_{e-e}. The obtained data are explained in the frame of the phase-space model (section 2.3.2). Majority electrons above the Fermi level propagate mainly

in the high velocity s band (see the Co band structure in figure 2.15). Thus, the variation of electron velocity with energy is considered to be characteristic of free electrons ($v \propto E^{1/2}$). The λ_{e-e} variation with energy can be described by equation 2.8. The model of equation 2.10 can adequately describe the λ_M variation in the 1-1.5 eV range. Figure 6.11 shows a fit to the data according to this model. As in reference [*van Dijken et al.*, 2002], it is essential to consider the additional effect of defects to obtain a good agreement. The value λ_{e-def} is determined from the fitting process to be 9 nm. However, there is a disagreement between the model and the experimental data for energies higher than 1.5 eV. Although an experimental artifact could be at the origin of this difference, this could be as well due to a deviation from the free electron model. Accurate calculations including the true Co band structure would then be needed as in reference [*Zhukov et al.*, 2006]. A fit without taking into account the effect of defect scattering is also shown. Obviously, the relation considering only the effect of electron-electron scattering does not properly account for the experimental data.

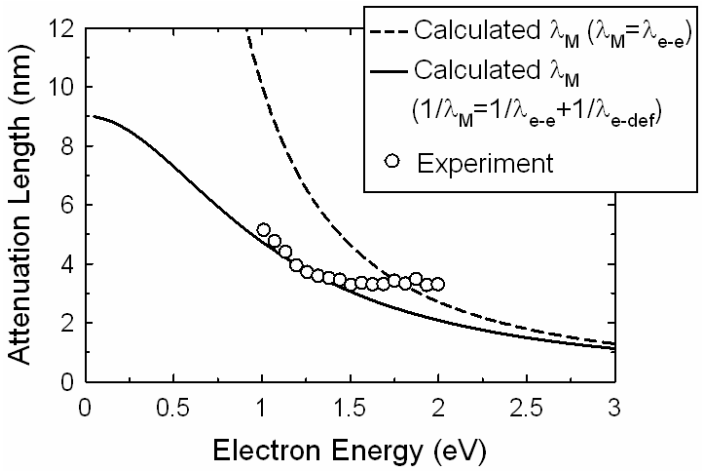

Figure 6.11: The variation of λ_M with energy is fitted with the $1/\lambda_M = 1/\lambda_{e-e} + 1/\lambda_{e-def}$ and $\lambda_M = \lambda_{e-e}$ models.

The increase of λ_m in Co can be also explained considering the phase-space model and the Co band structure. As λ_m is much shorter than λ_M, electron-electron scattering dominates as well in this case the value of the attenuation length. At 1 eV above the Fermi level, there are already plenty of available states for a hot electron to relax. This implies a strongly reduced lifetime. However, for energies higher than 1 eV, the increase of the available minority electron states with energy is much lower than in the 0-1 eV range (see figure 2.15). This is causing a small further decrease with energy of the minority electron lifetime. Moreover, for energies higher than 1.5 eV, minority electrons propagate in the high velocity s band and not in the lower velocity d band. In the range 1.5-2 eV electron velocity is constantly increasing with energy as for the free electrons. Thus, in this case the overall increase of velocity dominates the λ_m value,

explaining the observation.

In the case of Py, although a global minimum is observed for λ_M, the value remains relatively unchanged with energy. This indicates a low λ_{e-def} length that dominates the measured value. The increase of λ_m with energy can be explained taking into account the Ni band structure (since Py is a $Ni_{80}Fe_{20}$ alloy). From *ab-initio* calculations it was found that the electron velocity is constantly increasing for both spin populations in the 0.5-3 eV range [*Zhukov et al.*, 2006], in agreement with the observed behaviour.

6.3 Ballistic electron magnetic imaging

6.3.1 Magnetic imaging of Co/Cu/Py spin-valves

Magnetic domains in one of the two layers can be imaged if the other layer is saturated along a specified direction. This way, any variation of the BEEM magnetic signal can be attributed to the magnetic structure of the film studied. For this purpose a Co/-Cu/Py trilayer is used, which was shown to exhibit a distinct switching of the two magnetic layers (see section 4.6.2).

Magnetometry measurements

Figure 6.12a shows a MOKE hysteresis cycle taken on a Co(1.8 nm)/Cu(6 nm)/-Py(1.6 nm) spin-valve. The curve is dominated by the gradual magnetization reversal of the Co layer, which is found to occur over a wide field range (see section 4.6.2). Two slope changes are apparent at $\approx \pm 5$ Oe, splitting each magnetization reversal curve in two segments. The segment from minimum to maximum field is discussed. The signal decrease in the -40 to 0 Oe range is supposed to originate from the magnetization reversal process of the Co layer. The Py layer magnetization reversal process, presumably occurs in the 0-5 Oe field range, causing a faster signal decrease. In the field range ≈5-10 Oe, the signal decreases slower since the Py layer is almost fully reversed. Finally, the Co layer magnetization reversal is completed in the field range 10-40 Oe.

Figure 6.12b shows a GMR hysteresis cycle taken on a Co(1.4 nm)/Cu(6 nm)/-Py(1.6 nm) spin-valve. As before, the Co layer magnetization is not reversed abruptly, resulting in a gradual change of the GMR signal. Starting from minimum field, the MR increase up to zero field is due to the magnetization reversal of the Co layer. The abrupt signal change in the 0-5 Oe range, is presumed to originate from the Py layer magnetization reversal. For both branches, a plateau is observed at the maximum MR value, which is ≈0.50 %, in the range 4 Oe to 8 Oe for increasing field, and in the range -6 Oe to -10 Oe for decreasing field. This plateau occurs when the magnetization reversal process of the Py layer is almost completed. At this point, probably due to the different magnetization reversal processes of the two layers, the magnetization reversal of the last fractions of the Py layer is compensated by the magnetization reversal of the Co layer. The signal decrease observed for higher fields, is due to the gradual alignment

of the Co layer magnetization to the reversed Py layer magnetization. Finally, the saturation of the spin-valve is reached at 50 Oe.

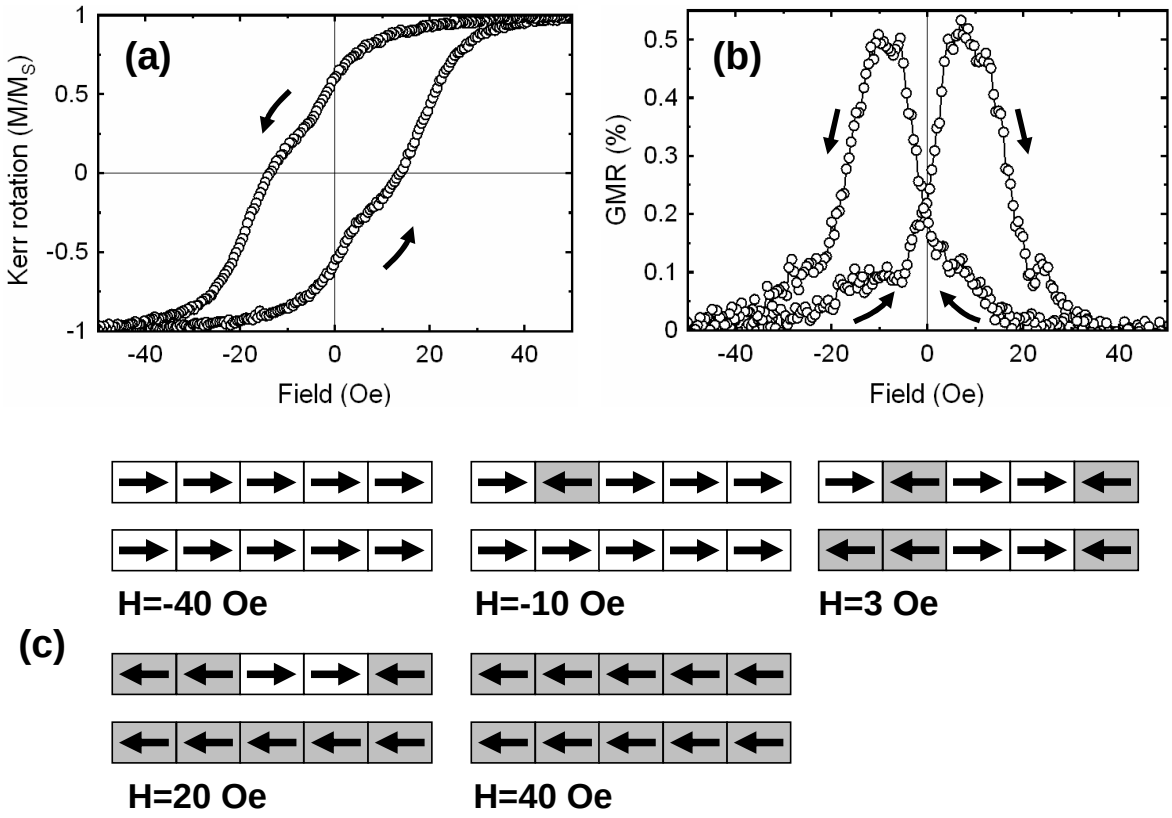

Figure 6.12: (a) MOKE and (b) GMR hysteresis cycles taken on Co/Cu/Py spin-valves showing the distinct switching of the two magnetic layers. (c) Schematic representation of the magnetization reversal process (upper layer:Co, lower layer:Py).

From the above magnetometry measurements, a magnetization reversal scheme for the two layers can be inferred, and it is shown in figure 6.12c. The Py layer magnetization reversal occurs within a narrow field range, much lower than the coercive field of the Co layer. In this field range, reversed magnetization domains are nucleated and grow in the Py layer, while the Co layer magnetization is only partially reversed. Since BEEM is a local technique probing a few μm^2, it is possible to image areas where the Co layer magnetization is not yet reversed, thus probing the magnetic structure of the Py layer. However, the magnetization reversal process of the two layers occurs simultaneously, and the resulting configuration is not always the desired one. Further sample fabrication development is needed, from the materials point of view, in order to fabricate spin-valves where the two layers have magnetization reversal processes well separated.

Transmission dependence as a function of applied field

BEEM imaging was performed on a Co(1.8)/Cu(6)/Py(1.6) spin-valve. As it is clear from the topographic image (figure 6.13a), there are significant STM tip instabilities during scanning. Every few scanning lines the scanning zone is shifted resulting in the observed topographic signal. This effect is also apparent in the BEEM image (figure 6.13b), since considerable transmission variations are often observed from scanning line to scanning line.

An important transmission depression is observed in the middle part. This feature cannot be correlated to the surface topography or attributed to tip instabilities. As it is shown in the average line profile (figure 6.13c), the signal decrease is much bigger than the ones caused from instabilities of the injection current. However, it can be directly correlated with the direction and intensity of the applied field. The scan direction is from bottom to top. First the spin-valve is imaged in the saturated state in a field of +80 Oe, resulting in high transmission. After several scan lines the field is switched to -1 Oe. The Py layer magnetization has been saturated toward the applied field direction and the spin-valve is in the AP aligned configuration. Finally the field is increased at -4 Oe resulting as well in the saturation of the Co layer magnetization. Thus, this feature is of purely magnetic origin.

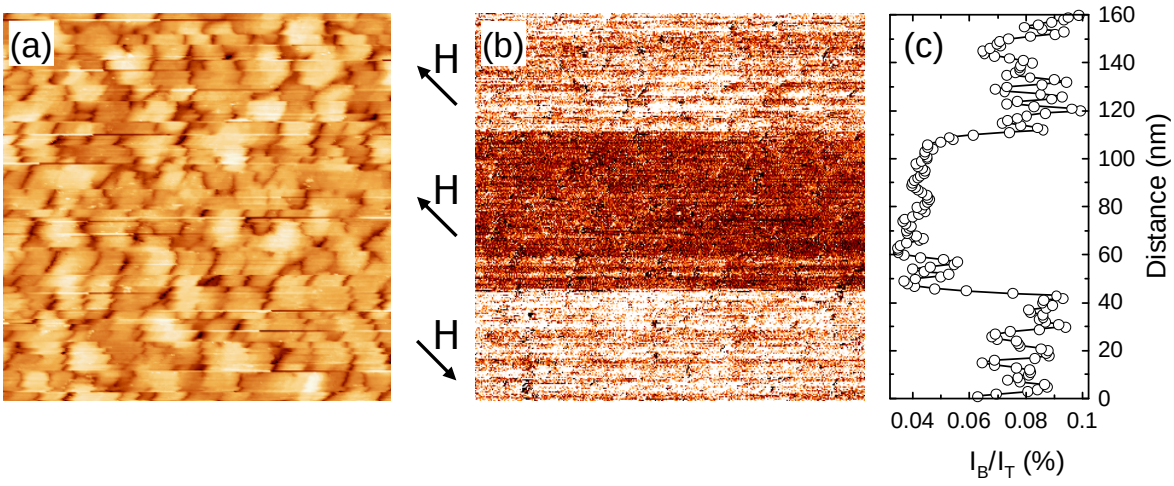

Figure 6.13: BEEM imaging of a Co(1.8)/Cu(6)/Py(1.6) spin-valve in various fields. (a) Topographic image. The color scale corresponds to height from 0.00 nm to 8.00 nm. (b) BEEM transmission signal. The color scale corresponds to transmission from 0.01 % to 0.09 %. (c) Average line profile of image (b). The scanning direction is from bottom to top. The fields applied successively are 80 Oe, -1 Oe and -4 Oe. Scan size 160×160 nm^2, V_T=2 V, I_T=50 nA.

The average transmission in the P and AP states is measured to be 0.083 % and 0.045 % respectively, determining a magnetic contrast ≈80 % at 2 eV injection energy.

Taking into account the considerable noise of the signal, the above values are in reasonable agreement with BEEM spectroscopy measurements (figure 6.7). The transmission in the P and AP states were then measured to be 0.093 % and 0.060 %, respectively, and the magnetic contrast ≈55 % at 2 eV.

For both magnetic layers the coercive field is found to be lower than determined by macroscopic magnetometry measurements (see figure 6.12). The local character of BEEM explains this disagreement, since in the sub-micrometric scale variations of the magnetic properties are expected. A BEEM study performed on epitaxial spin-valves concerning the coercive field distribution of the magnetic layers, shows the switching fields to deviate by more than 40 % [*Heindl et al.*, 2007b]. In this case, MOKE magnetometry hysterisis cycles show an abrupt switching of the magnetization of the two layers. For the polycrystalline films used in this study, the magnetization reversal of the spin-valve has been found to be gradual, and even higher switching field deviations could be expected.

Magnetic domain and domain wall imaging

Magnetic domain imaging during the magnetization reversal process of the Py layer is shown in figure 6.14. A series of BEEM images was taken in various fields (figure 6.14a-d). All images were taken roughly at the same position, as verified by the topographic signal (figure 6.14a'-d'). Various topographic features are apparent, and can be tracked from image to image. The position of the bright spot marked in the circle is measured taking as a reference the bottom right corner of each image. From a' to d', the distance of the spot from the right and bottom edge is (in nm): (480,180), (492,150), (505,145) and (502,140). For the whole series of images, the total shift of the scanning zone is not bigger than a few tens of nm. This displacement is negligible with respect to the μm-scale scanning size.

In figure 6.14a, both magnetic layers are saturated in a field of -40 Oe and the signal is almost homogeneously bright. At zero field, a reversed magnetic domain is nucleated (b) most probably in the Py layer, since it is the one with the lower coercive field. By increasing the field in the opposite direction, first at 2 Oe (c) and then at 4 Oe (d), the domain is observed to grow by domain wall propagation. From the corresponding topographic images, it is evident that the observed BEEM signal is not related to the surface structure. The argument that the reversal occurs in the Py layer is supported by the fact that only one single domain is observed to nucleate and grow. The reversal process of the Co film occurs by nucleation of multiple domains; besides, the field is much lower than the Co coercivity (see section 4.6.2).

The average transmission in the P and AP states is 0.087 % and 0.049 %, respectively. The small scale fluctuations of signal originate from the sample surface roughness and granular texture of the film (see section 5.2.1), resulting in a non-magnetic contrast that is superimposed onto the magnetic contrast during BEEM imaging. A similar effect is observed in Lorentz microscopy. In this case, electrons in the keV energy range are diffracted in the metal film and collected. The amount of scattering

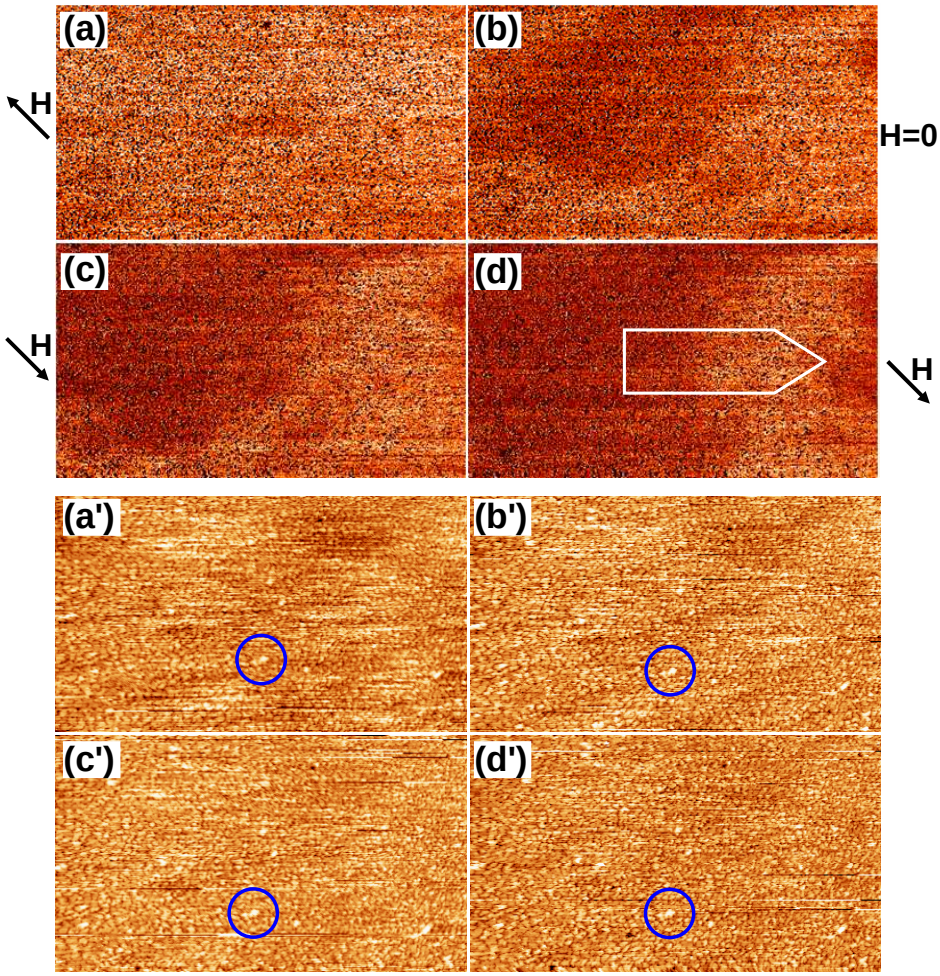

Figure 6.14: A series of BEEM magnetic images taken on the same position of a Co/-Cu/Py spin-valve. BEEM transmission signal in applied field: (a) -40 Oe (b) 0 Oe (c) 2 Oe (d) 4 Oe. The color scale corresponds to transmission from 0.01 % to 0.15 %. Corresponding topographic signal (a'-d'). The color scale corresponds to height from 0.00 nm to 5.27 nm. The RMS surface roughness is 1.29 nm. Scan size 2×1.2 μm^2, V_T=2 V, I_T=50 nA.

of the electron beam due to differently oriented crystallites varies considerably and gives rise to strong crystalline contrast in the magnetic images [*McVitie and Chapman*, 1990].

The images in figure 6.14 allow for a measurement of the domain wall width. Domain walls of the Néel type (in-plane magnetization rotation) are expected for such very thin magnetic films, while their width should be several tens of nm for soft magnetic materials like Py [*Hubert and Schäfer*, 1998]. The two-level BEEM signal indicates a fully P or a AP configuration so that 180° domain walls are imaged.

Figure 6.15 shows the average of line profiles taken in the box shown in figure 6.14d.

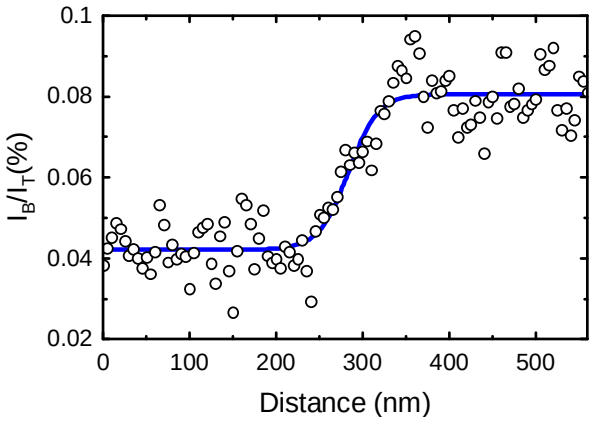

Figure 6.15: Average of line profiles taken on the box indicated in figure 6.14d. The solid line correspond to a hyperbolic tangent fit to the data.

A hyperbolic tangent function is used to fit this stepped profile,

$$T = C_T + \Delta T \ \tanh \frac{x - C_x}{W_0} \tag{6.7}$$

where C_T, ΔT, C_x, and W_0 are constants defined in section 5.6. The variable x refers to the distance along the transition, and T is the transmission (I_B/I_T) of the sample. The position of the domain wall center corresponds to $C_T = 0.061 \pm 0.001$ % and $C_x = 284 \pm 8$ nm, while $\Delta T = 0.019 \pm 0.001$ %.

The transition zone width, W, is equal to $W = 2.24 \times W_0$, as defined in section 5.6 (the distance where the transmission is increasing from 10 % to 90 % of the maximum value). This transition corresponds to the domain wall. The value $W_0 = 35 \pm 14$ nm is inferred from the fitting process, determining the domain wall width to be $W = 78 \pm 31$ nm, for the 1.6 nm thick Py film studied. In a Lorentz microscopy study of 180° Néel walls in thin Py films [*McVitie and Chapman*, 1990], the domain wall width was measured to be $W = 28$ nm and $W = 49$ nm for film thicknesses 60 nm and 20 nm respectively. However, a direct comparison of the two measurements would not lead to trustworthy results. The domain wall width is strongly dependent on the Py film quality, an extrinsic parameter that can significantly vary from experiment to experiment. Moreover, the magnetostatic effects between the Co and Py layers should be considered in our case, leading to further complications.

6.3.2 Magnetic imaging of Co/Cu/Co spin-valves

In this section, the ability of BEEM to image and quantify the extent of AP alignment of a spin-valve is discussed, and BEEM magnetic imaging is compared to GMR measurements. As shown in section 4.6, a symmetric Co/Cu/Co spin-valve does not exhibit a distinct switching of the Co layers magnetization, making it less appropriate

for a BEEM study. However, it is shown in the following that important information concerning the magnetic configuration of the sample can be inferred from BEEM experiments.

Magnetometry measurements

MOKE and GMR magnetometry measurements were performed on the same Co(1.8 nm)/-Cu(6 nm)/Co(1.8 nm) sample. Figure 6.16a shows a MOKE hysteresis cycle. It is immediately evident, that there is a complete absence of any features indicating a separate magnetization reversal of the two Co layers. The coercive field of the spin-valve is ≈23 Oe. This value indicates the zero magnetization state, where equal amount of reversed and non-reversed magnetic domains exists in each film. The coercive field roughly coincides with the field value where the maximum MR is observed. The spin-valve is saturated in a field higher than 120 Oe.

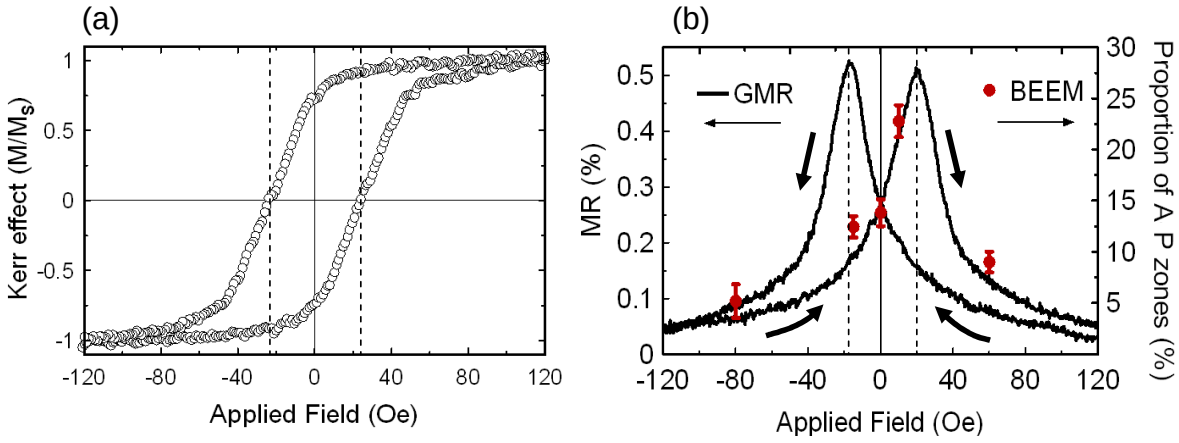

Figure 6.16: (a) MOKE hysteresis cycle taken on a Co/Cu/Co spin-valve. (b) GMR hysteresis cycle taken at room temperature on the same sample. The filled circles indicate the proportion of the AP aligned zones in the corresponding BEEM images (figure 6.17).

Figure 6.16b shows a current-in-plane GMR hysteresis cycle, taken at room temperature. The magnetization reversal of both Co layers occurs simultaneously over a wide field range, causing the gradual signal change. In this case, the saturation of the spin valve is only reached at ±200 Oe. This difference between the MOKE and GMR measurements, is probably because of the higher sensitivity of MR to the magnetic configuration of the spin-valve. The maximum MR value is ≈0.53 %, and for each branch, is observed in a revese field ≈20 Oe. In contrast to the GMR curve of the Co/Cu/Py spin-valve (figure 6.12), no signal plateau is observed in this case, since the magnetization reversal of the two Co layers is completely symmetric. The maximum MR value is observed at the zero magnetization state of the Co layers, as determined

from the MOKE measurement. At this point, there is equal amount of domains towards both directions in each Co layer, overlapping arbitrarily and resulting in the maximum extent of AP alignment

Comparison between BEEM and GMR measurements

There is a direct analogy between the BEEM magnetic contrast and GMR measurements, since in both cases the signal is a measure of the extent of AP alignment of the spin-valve. The GMR and BEEM measurements performed on two separate but identical Co(1.8 nm)/Cu(6 nm)/Co(1.8 nm) spin-valves deposited simultaneously side by side, are compared and discussed.

Figure 6.17 shows a series of BEEM magnetic images taken in various magnetic fields applied in the film plane. In (a) the topographic signal that corresponds to (b) is shown. The RMS surface roughness is measured to be 1.20 nm. By comparing the topographic signal of each BEEM image to the one of (b), it was found that the overall displacement is a few tens of nm, and thus negligible to the scan size. It is evident, that due to the surface roughness, a non-magnetic component is added to the BEEM contrast.

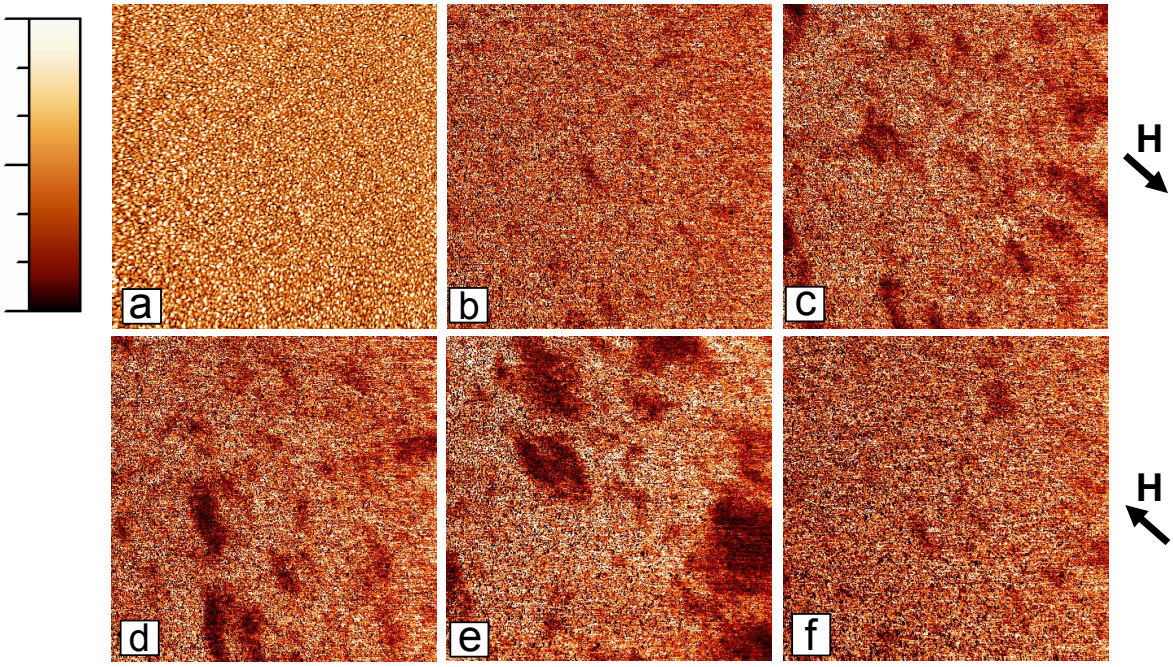

Figure 6.17: A series of BEEM magnetic images taken on the same position of a Co/Cu/Co spin-valve. (a) Topographic signal. The color scale corresponds to height from 0.00 nm to 5.79 nm. BEEM images taken in a field (b) -80 Oe, (c) -10 Oe, (d) 0 Oe, (e) +15 Oe, and (f) +60 Oe. The color scale corresponds to transmission from 0.02 % to 0.08 %. Scan size 2.6×2.6 μm^2. V_t=1.6 V, I_t=50 nA.

In (b) the spin-valve is almost saturated in a -80 Oe field. The BEEM signal is homogeneously bright, except some dark zones indicating non-parallel orientation. This is caused by local deviations of magnetization in one of the two layers. It is evident from the topographic signal that the BEEM contrast is not related to the film structure. As the applied field is decreased to -10 Oe (c), the extent of AP alignment has increased (see also figure 6.16). However, this increase corresponds mainly to the appearance of several new reversed magnetic domains, rather than the growth of the initial ones. The extent of AP alignment increases even further at 0 Oe (d), and at +15 Oe (e). The AP aligned zones become wider, probably because of coalescence of smaller inversed domains. Finally, at +60 Oe (f) the signal is almost homogeneously bright corresponding again to P alignment.

The average transmission measured at the P aligned zones in figure 6.17 is 0.051 %, while at the AP aligned zones is 0.023 %. The magnetic contrast calculated from these values is 96 % (at electron energy 1.8 eV). The transmission determined from BEEM spectroscopy measurements (figure 6.7), is in both cases higher, and equal to 0.079 % and 0.047 % respectively, at the same energy. The magnetic contrast in this case is 68 %. The main difference in the results between the two measurements is an overall transmission decrease. This could be attributed to a tip artefact that affects the injection geometry and results in lower transmission.

As it has been discussed before, during the magnetization reversal process of a Co/-Cu/Co spin-valve, inversed domains are nucleated in both films and overlap arbitrarily, creating AP aligned zones. Usually the magnetic configuration of the spin-valve is complicated, and it is not straightforward to attribute the observed BEEM contrast to the magnetic structure of one of the two layers. However, the images of figure 6.17 show a magnetization reversal process, where several AP aligned zones appear to form and coalesce. This fact strongly indicates that the magnetization reversal of the Co layers mainly occurs through the nucleation of inversed domains. The size of the domains should be similar to the size of the AP aligned zones, which is up to a few hundred of nm. The magnetization reversal process of the Co/Cu/Co spin-valve is found to be different than the one of the Co/Cu/Py spin-valve, where reversed domains nucleate in the Py layer and grow up to the micron scale (see section 6.3.1).

The filled circles on the GMR graph (fig. 6.16b) indicate the proportion of AP aligned zones as determined from the BEEM images. The two scales have been adjusted so that the GMR and BEEM points coincide at zero field. There is a rather good quantitative agreement between the two measurements, especially keeping in mind that the area probed by GMR (a few hundreds of μm^2) is much larger than for BEEM imaging ($\approx 7\ \mu m^2$). It would require the acquisition and averaging of several series of BEEM images to achieve a better quantitative agreement between the two types of measurement.

It is interesting to notice that at +15 Oe although the GMR signal corresponds to $\approx 80\%$ of its maximum value, BEEM shows an AP configuration of the spin-valve of less than 25%. This means that the GMR maximum does not correspond to an ideal AP alignement and that a GMR signal more than 4 times higher could be achieved

if the two magnetic layers were fully AP aligned. It is of technological importance to fabricate spin-valves with well defined P and AP configurations, in order to achieve the maximum response of a spin-valve component to an applied field.

6.3.3 360° domain walls in Co films

In the following, BEEM imaging of a special type of magnetic structures, known as 360° domain walls, is discussed. As in section 6.3.2, the symmetric Co/Cu/Co spin-valve is used. Although the presence of such magnetic structures is testified, it is not possible to locate them in one of the two Co layers. First, the effect of the applied field on the width and structure of the domain walls is discussed. Micromagnetic calculations support the experimental measurements, and provide the means to set an upper bound to the resolution of BEEM magnetic imaging.

360° domain walls

In very thin films, propagating Néel domain walls can get caught by structural defects, particularly by non-magnetic gaps in the film ("pinholes"). The pinning of the domain wall can lead to the formation of a peculiar wall type named *360°* domain wall [*Hubert and Schäfer*, 1998]. Such a structure is formed by the interaction of two 180° Néel walls. The type of the interaction depends on the wall rotation sense. Néel walls of opposite rotation sense attract each other because they generate opposite charges in their edges (figure 6.18a). If they are not pinned, they can annihilate. Néel walls of equal rotation sense repel each other (figure 6.18b). If they are pressed together by an external field disfavoring the region between them, they form 360° domain walls. This metastable wall type is not found in thicker films. In very thin films it can only be eliminated in much higher fields than needed for moving regular 180° walls.

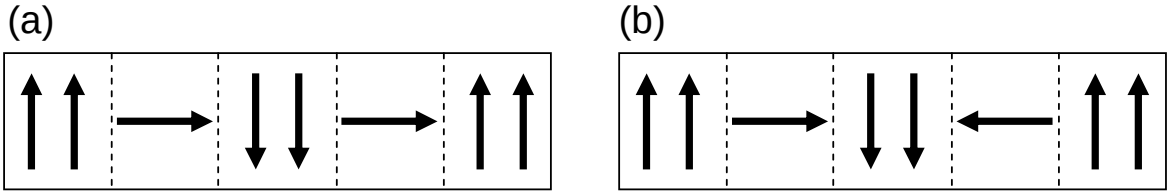

Figure 6.18: Schematic representation (top view) of two adjacent 180° domain walls, with opposite (a) and equal (b) rotation sense.

Figure 6.19 shows the formation of such structures observed by MOKE imaging of a 10 nm thick sputtered Py film [*Hubert and Schäfer*, 1998]. In (a) a single 180° Néel wall is pinned by two structural defects. As the field increases in (b) and (c) the pinning leads to the formation of two 360° walls. The wall axis is close to be vertical to the applied field ("vertical" wall). Sequence (d-f) shows a more complicated case. In (d) two 180° walls have either opposite, or equal rotation sense. The former are

annihilated under the influence of the applied field (e). The latter form 360° walls (e-f), both vertical and "horizontal" with the wall axis parallel to the applied field.

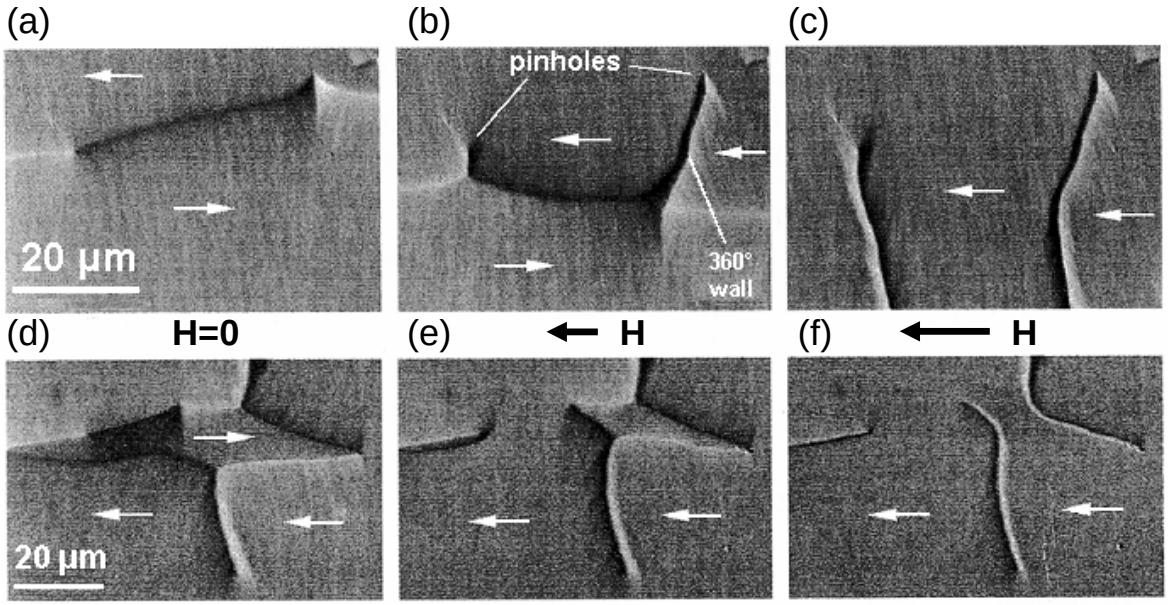

Figure 6.19: The formation of 360° domain walls observed by MOKE imaging of a 10 nm thick sputtered Py film. Sequence (a-c) shows the formation of two "vertical" 360° walls. Sequence (d-f) shows the formation of "vertical" and "horizontal" 360° walls, as well as the annihilation of 180° walls of opposite rotation sense. Taken from [*Hubert and Schäfer*, 1998]

There is a technological interest in studying this type of structures. The presence of 360° walls in the free layer of giant/tunnel magneto-resistance (XMR) sensors deteriorates their performance, because of the high magnetic fields needed to eliminate such magnetic structures. Since all XMR devices need very thin magnetic layers, the risk of immobile 360° walls has to be taken into account. This issue has already been treated in some studies. The formation of 360° walls in multilayer films showing GMR, was first observed using Lorentz microscopy [*Heyderman et al.*, 1994a]. The presence of 360° walls was found to affect the magnetization reversal process of microfabricated magnetic tunnel junction elements, in a Lorentz microscopy study [*Portier and Petford-Long*, 2000]. Finally, micron-sized, ellipse-shaped magnetic tunnel junctions were studied by the x-ray photoemission electron microscopy technique [*Hehn et al.*, 2008], and the local magnetic anisotropies existing at each extremity of the elements were found to influence the creation of 360° walls.

BEEM imaging

BEEM imaging of 360° domain walls in a Co(1.8 nm)/Cu(6 nm)/Co(1.8 nm) spin-valve is discussed. Figure 6.20a shows an image taken in a field of +100 Oe applied in the film plane. Before the acquisition several field cycles were applied in the range 200 to 100 Oe. The spin-valve is mainly saturated, while the topography-related contribution to the signal is always present. The dark feature apparent at the left is attributed to the presence of a 360° wall in one of the two Co layers [*Haq*, 2005]. The defect pinning the domain wall is out of the scanning field. Although that there are no reports for the annihilation field in the case of thin Co films, values as high as 20 times the coercive field have been reported for (Co/NiFe/Co)/Cu multilayers [*Heyderman et al.*, 1994b]. For the Co layers studied, a coercive field ≈15 Oe is measured by MOKE magnetometry (see section 4.6.2), and thus the 100 Oe applied field is assumed to be much smaller than the annihilation field.

The domain wall in figure 6.20a consists of three segments, labeled (I), (II) and (III) on the figure, probably because of pinning at structural defects. The abrupt change in signal on the top of segment (III) does not correspond to an actual magnetic structure. Since the acquisition time of each image is several minutes, and the scanning direction is from bottom to top, we can suppose that at this point the domain wall has been displaced under the influence of the applied field and temperature due to thermal activation.

Immediately after, an image is taken at the same fixed position, as verified by the topographic signal, in an applied field of +20 Oe, (figure 6.20b). Dark signal patches have appeared indicating the nucleation of small reversed domains. The dark feature at the lower-right part corresponds to the 360° domain wall that has been indeed displaced (in that case, only one segment is observed and is labeled (IV)).

It could be argued that the features observed in figure 6.20 result from the overlapping of domains in each magnetic layer. Figure 6.21 shows schematically the case where two 180° walls, one in each magnetic layer, are in neighboring positions resulting in the partial overlapping of domains with opposite magnetizations. A configuration like that would result to the successive imaging of two 180° walls, resembling a 360° wall. However, it should be noted that in a field of 100 Oe both Co layers are almost saturated, as it has been shown before by MOKE and GMR magnetometry measurements (see section 6.3.2). Thus, large domains with reversed magnetization do not exist in this case, and the features in figure 6.20 can be explained only as the presence of a 360° domain wall in one of the two layers.

Micromagnetic modeling

In order to go beyond a simple description, a micromagnetic calculation of the structure of the 360° domain walls has been performed.

In principle, the defects that make these domain walls exist should be taken into account (as in reference [*Schrefl et al.*, 2000] for example). However, the BEEM images shown above are too small to reveal their position, and the defects' nature is not known.

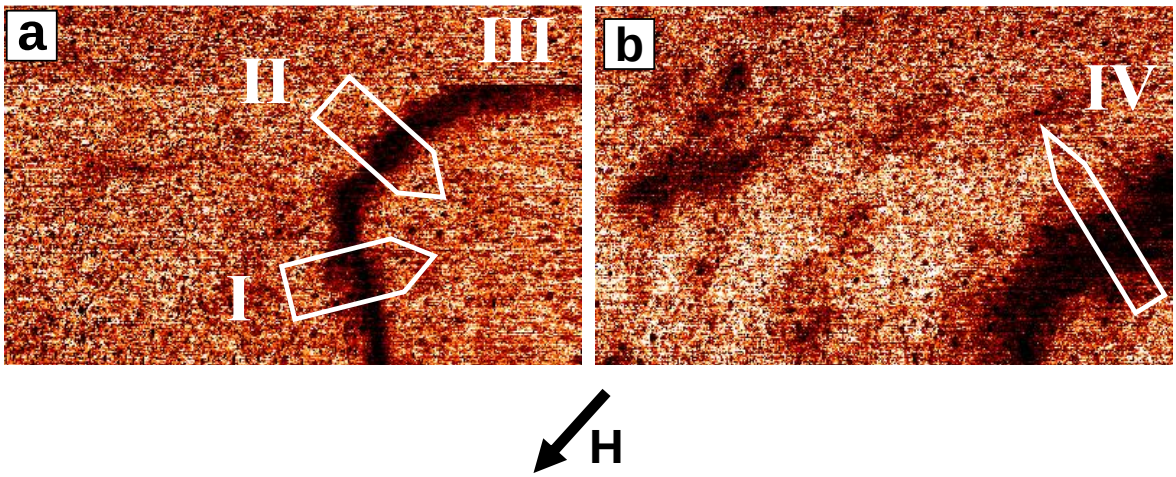

Figure 6.20: BEEM imaging of a Co/Cu/Co spin-valve. Images taken in a magnetic field of (a) +100 Oe and (b) +20 Oe. The applied field direction in both images is indicated by the arrow. The boxes indicate the area and direction of the line profiles averaging. Scan size 2.4×1.5 μm^2. V_t = 1.8 V, I_t=50 nA. The color scale corresponds to transmission from 0.02 % to 0.08 %.

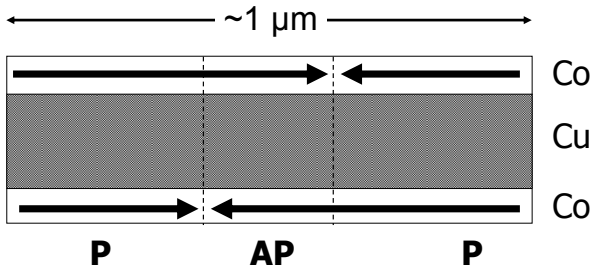

Figure 6.21: Schematic representation of the spin-valve magnetic configuration which would result in a signal resembling a 360° domain wall. This configuration is not possible in 100 Oe field since in this case both layers are saturated.

Thus, as a first step, simple 2D calculations in which the 360° domain wall is stabilized (compressed) by an applied field were performed. The wall was supposed to be infinitely long, and the calculation described the sample cross-section perpendicular to the wall extension direction (figure 6.22). The calculations were performed using the 2D version of the OOMMF code[2] [*Donahue and Porter*, 1999], with the magnetostatic calculation scheme that corresponds to an infinitely long sample.

The micromagnetic parameters were those of bulk Cobalt, namely M_s = 1400 kA/m, A = 30 pJ/m and K = 0 J/m^3. The zero anisotropy was established by MOKE measurements, and corresponds to the polycrystalline nature of the cobalt layer. No

[2]National Institute of Standards and Technology, http://math.nist.gov/oommf/

exchange coupling was introduced between the two cobalt layers, as the copper spacer is too thick for oscillatory magnetic coupling to exist [*Parkin et al.*, 1991]. A mesh size of 2 nm was taken, so that the sample described by the computation is in fact Co(2 nm)/Cu(6 nm)/Co (2 nm). The extension of the calculation region in the x direction (figure 6.22) was very large (10 μm). This way, magnetostatics can enforce that, at the left and right x boundaries, the moments are along the y axis, even for low fields.

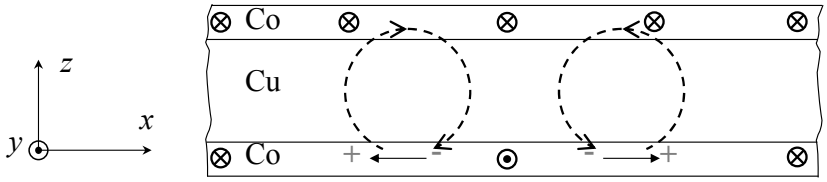

Figure 6.22: Cross section of a 360° domain wall structure in a two-layer sample, stabilized by a field aligned in the y direction. The magnetostatic charges in the domain wall layer are indicated. The dotted lines sketch the dipolar stray field from the lower layer.

A configuration containing the domain wall in one layer and a saturated state in the reference layer was generated, and relaxed under a y field. With no pinning applied, the wall is eventually forced to leave the calculation region. In order to avoid this, an arbitrary very large field $B_y = 1$T ($H_y = 10$ kOe) was applied to the central cell of the domain wall layer only, in order to fix the magnetic direction of that cell.

The converged configurations show that the domain wall (DW) layer influences the reference layer by magnetostatic coupling. Indeed, the magnetostatic charges present in the 360° domain wall structure produce an x field in the reference layer (figure 6.22), that tilts the magnetization toward the $\pm x$ direction (the so-called quasi-wall structure [*Hubert and Schäfer*, 1998]). Figure 6.23 displays the profiles of the m_y and m_x components of the magnetization unit vector $\vec{m}$ in both layers, at $B_y = -10$ mT ($H_y = 100$ Oe)(the m_z component is suppressed by the demagnetizing field in each layer, and is below 0.03). The magnitude of the BEEM signal is proportional to the cosine of the angle between the local magnetization direction in the two layers, a law that results directly from the two currents description with the assumption that the spins of electrons entering into a layer are measured (in the quantum-mechanical sense) along the local quantization axis. The normalized BEEM signal shown in figure 6.23b is calculated this way. The calculated FWHMs are 123.6 and 163.2 nm for the numerical m_y in the DW layer, and the numerical BEEM signal, respectively.

The magnetization deviation due to the magnetostatic interaction is clearly seen on the profiles of m_x (figure 6.23a): the reference layer has an m_x component with a sign opposite to that of the DW layer, and a smaller magnitude. This deviation is the main effect of the magnetostatic coupling between the two magnetic layers. Indeed, the magnetization profile in the DW layer is very close to that obtained when no

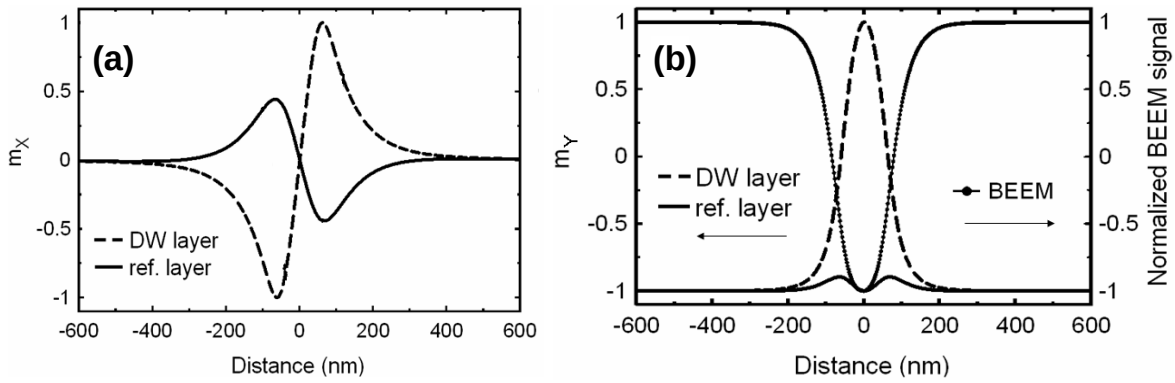

Figure 6.23: Profiles of the magnetization in both layers, for the longitudinal component m_x (a) and the axial component m_y (b), in the case of an axial applied field $B_y = -10$ mT. The calculated BEEM contrast is also superposed.

magnetostatic coupling between the two layers is considered (figure 6.24a). However, as displayed in figure 6.24b, this deviation affects significantly the profile of the BEEM signal across the domain wall. As the m_x are opposite in both layers, the BEEM profile is always significantly larger than the profile of the 360° domain wall itself.

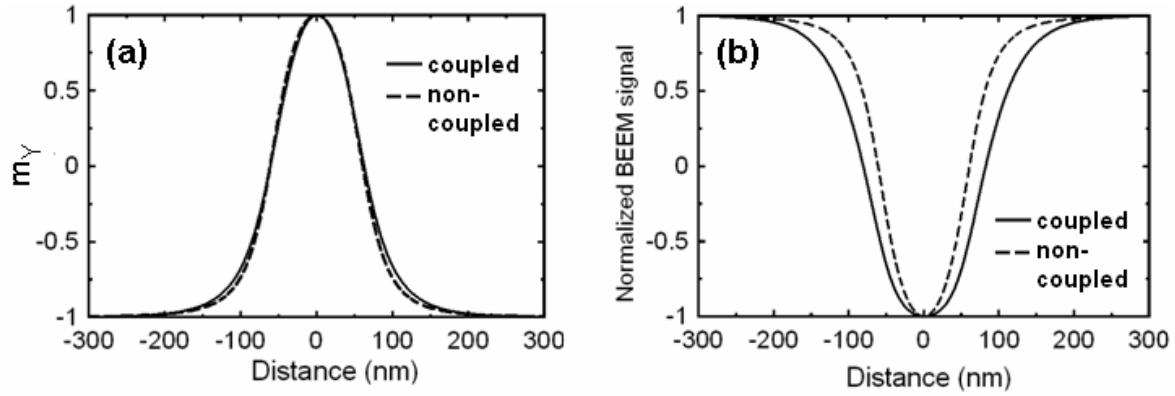

Figure 6.24: Magnified profiles of the magnetization in the DW layer for the longitudinal component m_y (a) and the calculated BEEM contrast (b), in the presence or not of magnetostatic coupling between the two Co layers.

Comparison between experiment and calculations

In order to compare experiments and calculations, line profiles were averaged along the indicated directions (figure 6.20). Since in fig. 6.20a the segment III is only partially imaged, we shall focus only on segments (I), (II) and (IV). For the segments (II) and

(IV), the applied field direction is P to the domain wall axis, and for the segment (I) the field direction is inclined at ≈55° with respect to the wall axis.

First the effect of the intensity of the applied field on the width of the domain wall is discussed. Considering the fact that the experimental images are of the same size, it is clear that the 360° domain wall is much larger at 20 Oe than at 100 Oe. In fig. 6.25a the measured profile of segment (II) is compared to the calculated profile of a 360° wall in a field of 100 Oe applied parallel to the wall axis. The FWHM of the wall is measured to be 160 nm, in good agreement with the calculated value which is 163.2 nm (figure 6.24), and the wall structure is symmetric. In fig 6.25b the measured profile of the wall (IV) in a field of 20 Oe (fig. 6.20b) is compared to the corresponding calculated profile and shows also a good agreement. In this case the wall has become wider (The FWHM is 400 nm and 408 nm for the experimental and calculated profiles, respectively) under the influence of a lower field. The increase of the wall width as the field decreases is in qualitative agreement with the results of a finite element micromagnetic simulation study [*Schrefl et al.*, 2000], where the width of a 360° domain wall in a 1 nm thick Co film was found to be ≈13 nm in a 2 kOe field.

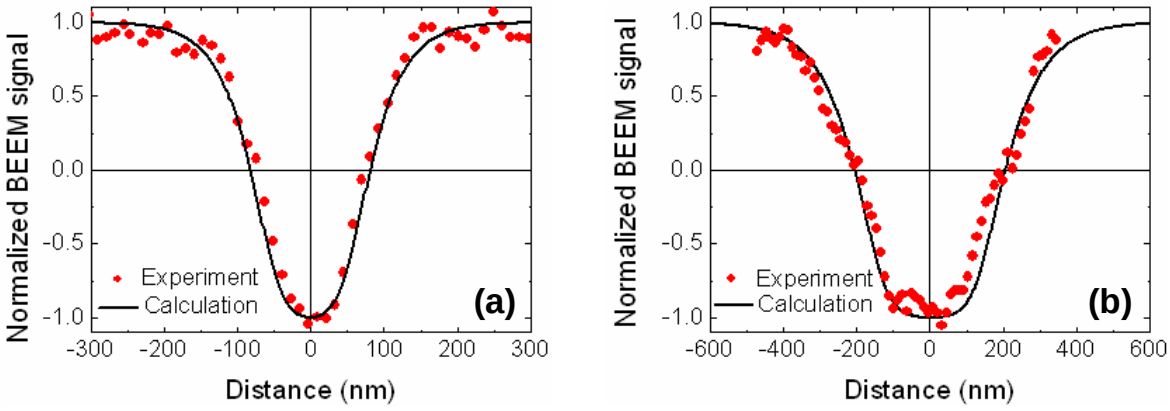

Figure 6.25: (a) Experimental and calculated domain wall profiles in a 100 Oe field applied parallel to the wall axis (fig. 6.20a, segment II). (b) Experimental and calculated domain wall profiles in a 20 Oe field applied parallel to the wall axis (fig. 6.20b). The experimental profiles were averaged over several lines as indicated by the boxes in fig 6.20.

The structure of the wall is also affected by the applied field direction as can be observed in figure 6.20. For segment (I) the field is inclined by 55° from the domain wall direction. It is noticeable that the transition region on the left side of the wall is wider than the one on the right side as further shows the averaged profile in figure 6.26. In the calculation, the effect of an additional x field was investigated in order to reproduce the misalignment between the domain wall and the external field. As can be seen from figure 6.22, the x field tends to favor one side of the wall at the expense of the other side. Thus, an asymmetric domain wall profile is created, and the symmetry

that kept the domain wall at the center disappears (hence the localized pinning field in the calculation). The profiles corresponding to the field applied in the experiment are superposed to the data in figure 6.26. This good match between images and micromagnetic calculations may even appear astonishing considering the noise present in the images. The conclusion is again that this noise has not a magnetic origin but, as pointed out before, is due to some fine structural defects.

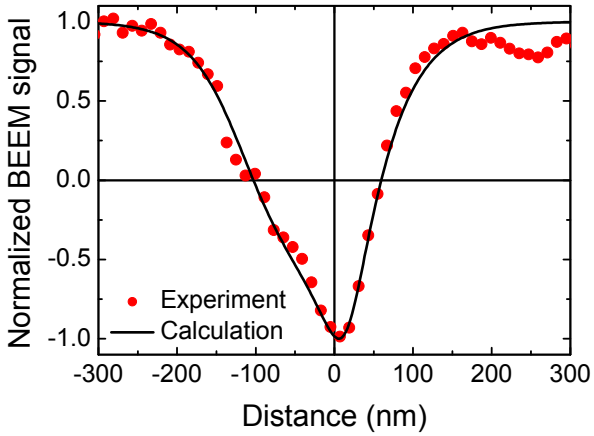

Figure 6.26: Experimental and calculated domain wall profiles in an applied field of 100 Oe, with the direction of the field being inclined at 55° with respect to the domain wall axis. The experimental profile was averaged over several lines as indicated by the box in fig 6.20.

BEEM magnetic resolution

The ultimate magnetic resolution of BEEM has never been estimated although theoretical arguments and non magnetic BEEM measurements let us expect a magnetic resolution close to one nanometer [*Prietsch*, 1995; *Sirringhaus et al.*, 1995] for injection energies close to the threshold. BEEM resolution in the case of figure 6.20, can be estimated by calculating the critical angle using equation 2.11 (section 2.3.2). For injection energy 1.8 eV above the Fermi level (1 eV above threshold), the critical angle is 10.5°. Since the source of scattering is in one of the Co layers, the layer thickness up to this level should be considered (see section 5.6). If the magnetic structure is in the upper Co layer, the important thickness is 4.5 nm (3 nm of Au and 1.5 nm of Cu). In this case resolution is 1.6 nm. If the magnetic structure is in the lower Co layer, the important thickness is 12.5 nm (the same as before, plus 2 nm of Co and 6 nm of Cu). In this case resolution is 4.5 nm.

In reference [*Haq*, 2005], the resolution of the images was estimated from 360° domain walls, calculating the transition region width as the distance between the points where 20% and 80% of the maximum signal are reached. Then, the authors have demonstrated a 28 nm resolution. The profile shown in figure 6.25a has a width on

the order of a few tens of nanometer, which leads to a 80 nm resolution following the definition from reference [*Haq*, 2005]. Since we have a very good agreement between experiments and calculations, we claim that this size corresponds to the actual magnetic structure size, and that it does not stem from a convolution effect due to the microscope resolution.

To go beyond and fix an upper bound to the resolution of the microscope, we consider the asymmetric calculated profile, and we calculate the convolution effect of a Gaussian on the profile shape for various values of the variance σ. Those convoluted profiles are compared to the experimental asymmetric one (figure 6.27). A good agreement is kept up to $\sigma = 20$ nm. For higher σ, the asymmetric profile is distorted in such extent that it would be difficult to distinguish between the symmetric and the asymmetric segments of the domain wall and we do not obtain a good agreement. In this case, a convenient BEEM resolution definition, would be the full-width at half maximum of the Gaussian distribution, which is $2\sqrt{2\ln 2}\sigma$. Then, according to this definition, the BEEM ability to resolve magnetic structures is better than ≈50 nm. However, this value is much bigger than the one estimated before (1.6 nm or 4.5 nm). Therefore, it is considered that the dimensions of the magnetic structures imaged, are too large to determine the maximum BEEM resolution. BEEM spin-valve samples are needed where smaller magnetic structures are created.

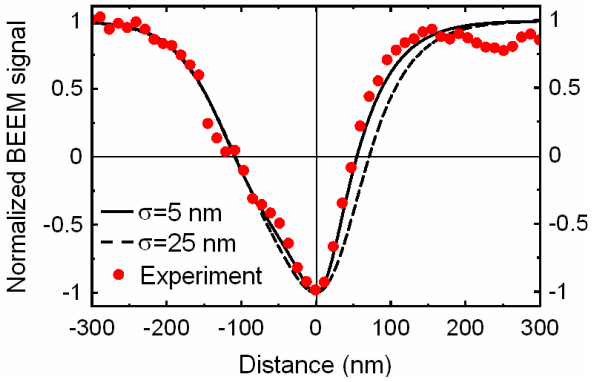

Figure 6.27: Same experimental profile as in figure 6.26. The solid and dashed lines correspond to the calculated profile shown in figure 6.26, convoluted with a gaussian of variance σ.

6.4 Conclusion

In this chapter, BEEM spectroscopy measurements on single magnetic layers and spin-valves, were discussed. The analysis of the measurements yields the variation of the spin-dependent attenuation length in Co and Py in the energy range 1-2 eV above the Fermi level. In both cases, the minority electrons were found to be attenuated stronger

than the majority ones. Although that similar studies have been already performed, the obtained results are different than the ones reported in the literature.

This difference in the attenuation intensity between the two spin-populations, was combined with the imaging capability of BEEM, in order to perform magnetic microscopy on spin-valves. The samples measured were Co/Cu/Py and Co/Cu/Co trilayers. High resolution imaging of the magnetic domains created during the magnetization reversal of the Py layer, was performed. A series of magnetic images obtained on the Co/Cu/Co spin-valve during a field cycle, was compared to GMR measurements on an identical structure. The close relation between the underlying principles of the two types of measurements, is clearly demonstrated.

Finally, a quantitative study of the BEEM magnetic contrast was presented for the first time. High resolution magnetic imaging has been performed on 360° domain walls in very thin Co films. The obtained contrast was compared with micromagnetic calculations, and a good agreement was found. The effect of the applied field on the domain wall width and structure was discussed. The results allows us to discuss the limits of the microscope resolution. This was shown to be better than 50 nm. It is believed that the actual value is considerably smaller, since in our case we are limited by the size of the magnetic structure imaged. Magnetic structures with smaller sizes should be imaged, in order to obtain the actual microscope resolution.

Chapter 7

Conclusions and perspectives

7.1 Conclusions

Spin-dependent hot electron transport studies and nanometer-scale magnetic imaging have been achieved using Ballistic Electron Emission Microscopy (BEEM). Since the initial demonstration of the technique [*Kaiser and Bell*, 1988], BEEM has been proved to be an excellent method for performing local hot electron transport studies and imaging [*Prietsch*, 1995; *Smoliner et al.*, 2004]. The first objective of this thesis, was to advance an existing BEEM setup to a state where hot electron transport through metallic multilayer/Si structures could be studied in a reproducible manner. However, the main objective was to perform high resolution imaging of magnetic structures, using the spin-dependence of hot electron transmission through multilayers containing spin-valves. Both objectives have been accomplished, as it is shown in chapters 5 and 6.

BEEM measurements necessitate a quite particular sample structure, that allows for the realization of a three terminal configuration that involves the detection of current signals in the pA range. In this framework, significant effort has been dedicated to the conception and development of an efficient sample fabrication method (chapter 4). A method for reproducibly fabricating atomically flat H-Si(111) substrates with ohmic back-contact has been developed, that constitutes a key element to the subsequent achievement of this project's objectives. Thereafter, Au films were grown onto these substrates, forming high quality Au/Si Schottky contacts (barrier height superior to 0.8 eV, ideality factor less than 1.1). Structural characterization of the Au films has been performed, and they were found to be polycrystalline and extremely uniform. Next, this Au/Si structure has been used as a substrate for the growth of multilayers containing single magnetic layers or spin-valves. Ultra-thin Co and Permalloy layers (thicknesses in the 1-6 nm range) encapsulated in Cu, have been used for this purpose. The magnetic layers were characterized using magnetometry measurements, and were found to have in-plane magnetization. The sample fabrication method developed, allowed us to perform BEEM measurements and to obtain results similar to those of the literature.

Besides reproducing existent studies, new results have also been obtained (see

chapter 5). The Cu/Si(111)(n-type) interface has been studied for the first time using BEEM, providing the ability of locally measuring the respective Schottky barrier height. BEEM measurements on samples containing magnetic metals (Co or Py) in sub-monolayer coverages have been also performed. The sample transmission has been found to vastly decrease in the presence of magnetic material. Although more or less similar studies exist [*Rippard and Buhrman*, 2000], the results obtained in this work are different and not fully understood, creating the need of performing further experiments. However, as the observed structures provide an intense contrast, they were used to determine the microscope spatial resolution, which was found to be less than 1 nm.

The main objective of this work was to perform spin-dependent ballistic electron transport and imaging measurements. BEEM samples containing single Co or Py magnetic layers and spin-valves have been elaborated and measured. Ballistic electron transmission through such samples was measured as a function of electron energy, in the range 1-2 eV above the Fermi level. The subsequent data analysis yielded the spin-dependent electron mean-free path in Co and Py. In both cases, the majority electron mean-free path was found to be much higher than the minority one, throughout the whole energy range studied. The results were compared to the literature and in the case of Co a more clear variation with energy was found, probably indicating less defect scattering. We remark that at the moment there are not many BEEM measurements of the spin-dependent mean-free path in metals.

Magnetic imaging was performed on the spin-valve samples. The nucleation and growth of magnetic domains during the magnetization reversal of a Py layer, was imaged with high spatial resolution. BEEM magnetic imaging and GMR measurements on a Co/Cu/Co spin-valve were compared, and the relation between the two types of measurements was demonstrated. Finally, imaging of 360° domain walls in Co layers has been performed, and the contrast was analyzed quantitatively. The magnetic structure of the domain walls has been unraveled by comparing the experimental signal to micromagnetic calculations. The insight gained this way, allows the discussion about the source of contrast during BEEM magnetic imaging. Moreover, BEEM magnetic resolution was shown to be better than 50 nm. It is believed that the actual value is considerably smaller, since in our case we are limited by the size of the magnetic structure imaged.

7.2 Perspectives

The measurements presented above have demonstrated the ability of our instrument to perform spin-dependent ballistic transport and imaging experiments. The execution of more elaborate experiments can be conceived, either with the microscope in its current status, or after modifications.

First of all, the study of samples containing Co and Py in sub-monolayer coverages raised considerable ambiguity. The presence of the buried clusters should be as well ver-

ified by different kind of measurements. One possibility would be to perform Electron Energy Loss Spectroscopy using a Scanning Transmission Electron Microscope. The chemical selectivity of the technique in combination with its high spatial resolution, could reveal the presence of buried magnetic material clusters. Similar samples could be also prepared containing different materials, like Cr and Mn (anti-ferromagnetic $3d$ metal) or Zn. This would clarify whether or not the observed results are due to the presence of a magnetic material.

The capability of performing BEEM measurements on Cu/Si(111) samples, allows a systematic study of transmission versus layer thickness to be performed. By this way, the electron mean-free path in Cu can be measured up to energies a few eV above the Fermi level. The method used for determining the spin-dependent mean-free path in Co and Py, can be extended to other magnetic metals like pure Fe and Ni or CoFe. Besides the interest from the materials science point of view, the comparison of the experimental results with *ab-initio* calculations [*Zhukov et al.*, 2006] can reveal the underlying physics of hot electron transport in ferromagnets.

From the applications point of view, the capability of performing hot electron transport and imaging can be utilized to optimize the performance of hot electron magnetoelectronic devices. A systematic study with respect to the materials and processes used, can result in structures with increased magnetic contrast and spatially homogeneous hot electron transmission.

Besides transport measurements, high resolution magnetic microscopy measurements can be also performed. A first option would be to search for the actual microscope resolution. For this purpose, 360° domain walls might be appropriate. As it has been shown in section 6.3.3, the wall width decreases as the applied magnetic field increases. In this case, imaging of 360° domain walls in higher fields ($\approx$1 kOe) could lead to structures with sufficiently reduced dimensions. For this, a modification of the coils that provide the magnetic field would be necessary, since at the moment such high fields are not accessible.

The high resolution of the microscope allows the imaging of magnetic nanostructures, as shown before [*Rippard et al.*, 2000]. In this case however, a considerable effort should be made in order to develop an efficient sample fabrication method. All the stringent consideration of a BEEM sample should be taken into account. The field induced magnetization reversal process of nanostructures could be imaged. The modification of the instrument by adding two more electrical contacts to the sample holder, could allow the study of the current induced magnetization reversal process in magnetic nanowires.

In conclusion, the demonstrated capability of our instrument to perform local spin-dependent electron transport studies and high resolution magnetic imaging, allows the further exploitation of both possibilities.

Communications related to this work

Publications in peer-reviewed journals

"Hot electron transport and a quantitative study of ballistic electron magnetic imaging on Co/Cu multilayers"
A. Kaidatzis, S. Rohart, A. Thiaville and J. Miltat
Phys. Rev. B 78, 174426 2008

Communications in international conferences

- The 23rd Nishinomiya-Yukawa Memorial International Workshop "Spin Transport in Condensed Matter " October 27 - November 28, 2008 Yukawa Institute for Theoretical Physics, Kyoto University (oral)

  A. Thiaville, *A. Kaidatzis*, S. Rohart, J. Miltat

  "Study of spin polarized hot electron transport by ballistic electron emission microscopy"

- 14th International Conference on Thin Films, Ghent, Belgium, November 17 - 20, 2008 (poster).

  A. Kaidatzis, S. Rohart, A. Thiaville and J. Miltat

  "Ballistic electron emission microscopy of Co and NiFe multilayers and clusters buried in Cu"

- 53rd Annual Conference on Magnetism and Magnetic Materials, Austin, Texas, November 10-14, 2008 (oral).

  S. Rohart, *A. Kaidatzis*, A. Thiaville and J. Miltat

  "Hot electron transport and quantitative study of ballistic electron magnetic imaging on Co/Cu multilayers"

- Joint European Magnetics Symposia, Dublin, Ireland, September 14 - 19, 2008 (oral).

  S. Rohart, *A. Kaidatzis*, A. Thiaville and J. Miltat

"Hot electron magnetic imaging on Co/Cu/Co and Co/Cu/FeNi spin valves"

- Workshop on high temporal and spatial resolution studies of magnetic nanostructures Augustow, Poland, June 27 - July 2, 2008 (oral)

  A. Thiaville, *A. Kaidatzis*, S. Rohart, J. Miltat

  "Magnetic Force Microscopy and Ballistic Electron Emission Microscopy"

- IEEE International Magnetics Conference, Madrid, Spain, May 4 - 8, 2008 (oral).

  A. Kaidatzis, S. Rohart, A. Thiaville and J. Miltat

  "Ballistic Electron Magnetic Microscopy on Co/Cu/NiFe spin valves"

Communications in national conferences

- 12th Louis Néel colloquium, La Grande Motte, France, September 30 - October 3, 2008 (oral).

  A. Kaidatzis, S. Rohart, A. Thiaville and J. Miltat

  "Hot electron transport and magnetic imaging on Co/Cu/Co and Co/Cu/FeNi spin valves" (in French)

- Workshop SOLEIL Microscopy Opportunities, Gif-sur-Yvette, France, January 15 and 16, 2008 (poster).

  S. Rohart, *A. Kaidatzis*, A. Thiaville and J. Miltat

  "Ballistic Electron Magnetic Microscopy" (in French)

- 11th Louis Néel colloquium, Lyon, France, March 14 - 16, 2007 (poster).

  A. Kaidatzis, F. Caud, C. Vouille, A. Thiaville and J. Miltat

  "Ballistic Electron Emission Microscopy" (in French)

- Veeco French AFM users meeting, Gif-sur-Yvette, France, November 9 and 10, 2006 (poster).

  A. Kaidatzis, A. Thiaville and J. Miltat

  "AFM study in air of the hydrogenated-Si(111) surface" (in French)

Acknowledgments

This work has finally finished, after three marvelous years in France, only because I had the pleasure to receive the generous and unselfish aid and support of many people. The least I can do in return is to express my gratitude.

This adventure became real due to the opportunities given by the European Community through the Marie Curie program. Thus, I would like first to thank Professor Michel Héritier for welcoming me at the LPS Marie Curie training site.

I would like to thank Ron Jansen and Bertrand Kierren for kindly accepting to referee this thesis. I would also like to thank Bernard Dieny, Yves Lassailly and Dimitris Niarchos for accepting to participate in the jury for my thesis defense.

I'm grateful to my thesis supervisor André Thiaville, as well to Jacques Miltat and Stanislas Rohart. It was a privilege and joy working with such brilliant scientists and exceptional people. Their scientific excellence resulted in the quality of this work, and, maybe more important, their personal qualities resulted in three outstanding years of everyday life. Besides the evident, improving my skills, André, Jacques and Stanislas have also improved me as a person. Thank you!

This work has finished in three years only because the foundations were already laid. Thus, I would like to thank Francois Caud and Carole Vouille for their crucial contribution to the BEEM project. The mechanical shadow-mask approach utilized for the whole of my thesis is just an improvement of the method that Francois developed.

I am indebt to Marco Aprili for offering his deposition setup and to Jacques Ferré for magneto-optical characterization. Both contributions were essential to this project and resulted in the achievement of our main objectives. Thank you both!

I had the opportunity to receive the aid of two researchers from the STEM group of our lab. I thank Alexandre Glotter for DOS calculations and Nathalie Brun for TEM measurements of our samples. Both contributions were valuable for unraveling the secrets of our structures.

The sample holders (and other pieces) I used for this work became a reality because of the Craftsmanship of the mechanical workshop people. I thank Gilles Guillier, Jean-Louis Signoret, Brahim Kasmi and Fabrice Quenault for providing me those pieces of Art, always quickly and as they were supposed to be, however the difficulty of the design. Vraiment des grands mécaniciens!

During this work, I had the pleasure to receive the engineering support of Vincent Klein and Sambath Saranga. I thank you both for all the electronic instruments you have fabricated. The various LabView virtual instruments that Vincent programmed

were necessary for performing deposition or measurement experiments.

I would like to thank Pascale Senzier and Raphaël Weil for their aid with HV thermal evaporation and Zhizhong Li for x-ray diffraction experiments. Besides their crucial contribution to this work, I deeply appreciate their willingness to help in any way without hesitation.

A very important, but not always evident, part of every big project is the logistic support. Thus, I would like to thank Nadine Mehl, Sylvie Falcinelli, Veronique Thiuelart, Sadrine Richard, Martine Delor and especially Mrs Marie-France Cozic for all the orders she efficiently made for me.

I would like to thank my fellow students Benoit Montigny, Jen-Yves Chauleau, Jean-Paul Adam, Mathieu Cormier and Nicolas Bergeard for chatting, for occasional help and for working in harmony in the same research group. I would also like to thank Amandine Bellec for sharing an office during my last couple of months at the LPS, and I wish the best for her postdoctoral work with BEEM.

I was fortunate to make several new friends in Paris, so I would like to thank Andreas, Peter, Alexandros, Sascha, Johan, Allesandro, Pierre... for all the coffees and beers we had together!

I would like to thank my other half Evi for supporting me all these years and for successfully dealing with a long-distance relationship with a difficult character like me! Finally, I would like to thank my parents simply because I owe them everything.

Abstract

Spin dependent hot electron transport and nanoscale imaging of metal/silicon structures

In this work, we experimentally study spin-dependent hot electron transport through metallic multilayers (ML), containing single magnetic layers or "spin-valve" (SV) trilayers. For this purpose, we have set up a ballistic electron emission microscope (BEEM), a three terminal extension of scanning tunnelling microscopy on metal/semiconductor structures. The implementation of the BEEM requirements into the sample fabrication is described in detail. Using BEEM, the hot electron transmission through the ML's was systematically measured in the energy range 1-2 eV above the Fermi level. By varying the magnetic layer thickness, the spin-dependent hot electron attenuation lengths were deduced. For the materials studied (Co and NiFe), they were compared to calculations and other determinations in the literature. For sub-monolayer thickness, a non uniform morphology was observed, with large transmission variations over subnanometric distances. This effect is not yet fully understood. In the imaging mode, the magnetic configurations of SV's were studied under field, focussing on 360° domain walls in Co layers. The effects of the applied field intensity and direction on the DW structure were studied. The results were compared quantitatively to micromagnetic calculations, with an excellent agreement. From this, it can be shown that the BEEM magnetic resolution is better than 50 nm.

Keyword(s): magnetic multilayers - metal/semiconductor structures - spin-dependent transport - hot electrons - STM-BEEM - magnetic microscopy - micromagnetic calculations

Resumé

Transport dépendant du spin d'électrons chauds et imagerie magnétique à l'échelle nanométrique de structures métal/silicium

Nous étudions expérimentalement le transport dépendant du spin d'électrons chauds dans des multicouches (MC) magnétiques, qui contiennent des couches uniques magnétiques, ou des tricouches de type "vannes de spin" (VS). Pour cela, nous avons mis en oeuvre la microscopie á émission d'électrons balistiques (BEEM), une extension á trois contacts de la microscopie á effet tunnel sur des structures métal/semiconducteur. La méthode mise au point pour satisfaire les nombreuses contraintes imposées par le BEEM sur les échantillons est décrite en détail. La transmission des électrons chauds dans des MC a été systématiquement mesurée dans la gamme d'énergie 1-2 eV au dessus du niveau de Fermi. De l'étude en fonction des épaisseurs des couches magnétiques nous avons déduit les longueurs d'atténuation des électrons chauds en fonction du spin et de l'énergie. Ces mesures, sur le cobalt et l'alliage doux NiFe, sont comparées à des calculs et résultats expérimentaux de la littérature. Pour des épaisseurs inférieures à la monocouche atomique, une organisation spatialement hétérogène a été observée, avec un effet très important sur la transmission BEEM, variant sur une échelle sub-nanométrique. En mode imagerie, nous avons étudié les configurations magnétiques de VS, en particulier des parois à 360° dans des couches de cobalt. Les effets de l'intensité et la direction du champ appliqué sur la structure de ces parois ont été observés. Ces résultats ont été comparés quantitativement à des calculs micromagnétiques, avec un accord excellent. Ceci a permis de montrer que la résolution magnétique du BEEM est meilleure que 50 nm.

Mot(s)-Clé(s): multichouches magnétiques - structures métal/semiconducteur - transport dépendant du spin - électrons chauds - STM-BEEM - microscopie magnétique - calculs micromagnétiques

Bibliography

Aeschlimann, M., Bauer, M., Pawlik, S., Weber, W., Burgermeister, R., Oberli, D. and Siegmann, H.C. *Ultrafast spin dependent electron dynamics in fcc Co* Phys. Rev. Lett. **79** 5158 (1997)

Anil-Kumar, P.S., Jansen, R., van't Erve, O.M.J., Vlutters, R., de Haan, P. and Lodder, J.C. *Low-field magnetocurrent above 200% in a spin-valve transistor at room temperature* J. Magn. Magn. Mat. **214** L1 (2000)

Baibich, M.N., Broto, J.M., Fert, A., Dau, F.N.V., Petroff, E., Eitenne, P., Creuzet, G., Friederich, A. and Chazelas, J. *Giant magnetoresistance of (001)Fe/(001)Cr magnetic superlattices* Phys. Rev. Lett. **61** 2472 (1988)

Banerjee, T., Haq, E., Siekman, M.H., Lodder, J.C. and Jansen, R. *Ballistic Hole Emission Microscopy on metal/semiconductor interfaces* IEEE Trans. Magn. **41** 2642 (2005a)

Banerjee, T., Haq, E., Siekman, M.H., Lodder, J.C. and Jansen, R. *Spin filtering of hot holes in a metallic ferromagnet* Phys. Rev. Lett. **94** 027204 (2005b)

Banerjee, T., Lodder, J.C. and Jansen, R. *Origin of the spin-asymmetry of hot-electron transmission in Fe* Phys. Rev. B **76** 140407 (2007)

Bannani, A., Bobisch, C. and Moller, R. *Ballistic electron microscopy of individual molecules* Science **315** 1824 (2007)

Banninger, U., Busch, G., Campagna, M. and Siegmann, H.C. *Photoelectron spin polarization and ferromagnetism of crystalline and amorphous nickel* Phys. Rev. Lett. **25** 585 (1970)

Bauer, A., Cuberes, M.T., Prietsch, M. and Kaindl, G. *Quantitative study of electron transport in ballistic electron emission microscopy* Phys. Rev. Lett. **71** 149 (1993)

Beaurepaire, E., Bulou, H., Scheurer, F. and Kappler, J.P. *Magnetism: A synchrotron radiation approach* (Springer, Berlin, 2006)

Bell, L.D. *Evidence of momentum conservation at a nonepitaxial metal/semiconductor interface using ballistic electron emission microscopy* Phys. Rev. Lett. **77** 3893 (1996)

Bell, L.D., Hecht, M.H., Kaiser, W.J. and Davis, L.C. *Direct spectroscopy of electron and hole scattering* Phys. Rev. Lett. **64** 2679 (1990)

Bell, L.D. and Kaiser, W.J. *Observation of interface band Structure by ballistic electron emission microscopy* Phys. Rev. Lett. **61** 2368 (1988)

Bell, L.D., Kaiser, W.J., Hecht, M.H. and Davis, L.C. *New electron and hole spectroscopies based on ballistic electron emission microscopy* J. Vac. Sci. Technol. B **9** 594 (1991)

Berger, H.H. *Contact resistance and contact resistivity* J. Electrochem. Soc. **119** 507 (1972)

Binnig, G. and Rohrer, H. *Scanning tunneling microscopy* IBM J. Res. Develop. **30** 355 (1986)

Binnig, G., Rohrer, H., Gerber, C. and Weibel, E. *Surface studies by scanning tunneling microscopy* Phys. Rev. Lett. **49** 57 (1982)

Bode, M. *Spin-polarized scanning tunnelling microscopy* Rep. Prog. Phys. **66** 523 (2003)

Brillson, L.J. *The structure and properties of metal-semiconductor interfaces* Surf. Sci. Rep. **2** 123 (1982)

Busch, G., Campagna, M., Cotti, P. and Siegmann, H.C. *Observation of electron polarization in photoemission* Phys. Rev. Lett. **22** 597 (1969)

Caud, F. *Microscopie tunnel à électrons balistiques: vers le magnétisme* Ph.D. thesis Université Paris-sud (2006)

Chopra, K.L. *Thin film phenomena* (McGraw Hill, 1969)

Chulkov, E.V., Borisov, A.G., Gauyacq, J.P., Sánchez-Portal, D., Silkin, V.M., Zhukov, V.P. and Echenique, P.M. *Electronic excitations in metals and at metal surfaces* Chem. Rev. **106** 4160 (2006)

Cohen, S.S. *Contact resistance and methods for its determination* Thin Solid Films **104** 361 (1983)

Colis, S., Gieres, G., Bar, L. and Wecker, J. *Low tunnel magnetoresistance dependence versus bias voltage in double barrier magnetic tunnel junction* Appl. Phys. Lett. **83** 948 (2003)

Crowell, C.R., Spitzer, W.G., Howarth, L.E. and LaBate, E.E. *Attenuation length measurements of hot electrons in metal films* Phys. Rev. **127** 2006 (1962)

Crowell, C.R. and Sze, S.M. *Hot electron transport and electron tunneling in thin film structures* 325, dans *Physics of thin films* (Academic Press, New York, 1967)

Donahue, M.J. and Porter, D.G. *OOMMF user's guide, version 1.0* (National Institute of Standards and Technology, Gaithersburg, 1999)

Dumas, P., Chabal, Y.J. and Jakob, P. *Morphology of hydrogen terminated Si(111) and Si(100) surfaces upon etching in HF and buffered-HF solutions* Surf. Sci. **269/270** 867 (1992)

Freeman, M.R. and Choi, B.C. *Advances in magnetic microscopy* Science **294** 1484 (2001)

Gadbois, J., Zhu, J.G., Vavra, W. and Hurst, A. *The effect of end and edge shape on the performance of pseudo spin-valve memories* IEEE Trans. Mag. **34** 1066 (1998)

Gheber, L.A., Hershfinkel, M., Gorodetsky, G. and Volterra, V. *Investigation of the composition and electrical properties of gold/H-terminated silicon(111) interface* Thin Solid Films **320** 228 (1998)

Gonzalez, L., Miranda, R., Salmerón, M., Vergés, J.A. and Ynduráin, F. *Experimental and theoretical study of Co adsorbed at the surface of Cu: Reconstructions, charge-density waves, surface magnetism, and oxygen adsorption* Phys. Rev. B **24** 3245 (1981)

Gräf, D., Grundner, M., Schulz, R. and Mühlhoff, L. *Oxidation of HF treated Si wafer surfaces in air* J. Appl. Phys. **68** 5155 (1990)

Gröbli, J.C., Oberli, D. and Meier, F. *Crucial tests of spin filtering* Phys. Rev. B **52** R13095 (1995)

Grünberg, P., Schreiber, R. and Pang, Y. *Layered magnetic structures: Evidence for antiferromagnetic coupling of Fe layers across Cr interlayers* Phys. Rev. Lett. **57** 2442 (1986)

Grupp, C. and Taleb-Ibrahimi, A. *Au/H-Si(111)-(1×1) interface versus Au/Si(111)-(7×7)* Phys. Rev. B **57** 6258 (1998)

Haq, E. *Nanoscale spin dependent transport of electrons and holes in Si/ferromagnet structures* Ph.D. thesis University of Twente (2005)

Haq, E., Banerjee, T., Siekman, M.H., Lodder, J.C. and Jansen, R. *Ballistic hole magnetic microscopy* Appl. Phys. Lett. **86** 082502 (2005)

Haq, E., Banerjee, T., Siekman, M.H., Lodder, J.C. and Jansen, R. *Excitation and spin-transport of hot holes in ballistic hole magnetic microscopy* Appl. Phys. Lett. **88** 242501 (2006)

Harris, N.S. *Modern vacuum practice* (N. S. Harris, Glasgow, 2005)

Hecht, M.H., Bell, L.D., Kaiser, W.J. and Davis, L.C. *Ballistic-hole spectroscopy of interfaces* Phys. Rev. B **42** 7663 (1990)

Heer, R., Eder, C., Smoliner, J. and Gornik, E. *Floating electrometer for scanning tunneling microscope applications in the femtoampere range* Rev. Sci. Instrum. **68** 4488 (1997)

Heer, R., Smoliner, J., Bornemeier, J. and Bruckl, H. *Ballistic electron emission microscopy on spin valve structures* Appl. Phys. Lett. **85** 4388 (2004)

Hehn, M., Lacour, D., Montaigne, F., Briones, J., Belkhou, R., El-Moussaoui, S., Maccherozzi, F. and Rougemaille, N. *360° domain wall generation in the soft layer of magnetic tunnel junctions* Appl. Phys. Lett. **92** 072501 (2008)

Heiblum, M. and Fischetti, M.V. *Ballistic hot electron transistors* IBM J. Res. Develop. **34** 530 (1990)

Heiblum, M., Thomas, D.C., Knoedler, C.M. and Nathan, M.I. *Tunneling hot electron transfer aplifier:A hot electron GaAs device with current gain* Appl. Phys. Lett. **47** 1105 (1985)

Heindl, E., Vancea, J. and Back, C.H. *Ballistic electron magnetic microscopy on epitaxial spin valves* Phys. Rev. B **75** 073307 (2007a)

Heindl, E., Vancea, J., Woltersdorf, G. and Back, C.H. *Hot electron transport and magnetic anisotropy in epitaxial spin valves* Phys. Rev. B **76** 104435 (2007b)

Hersam, M.C., Guisinger, N.P., Lyding, J.W., Thompson, D.S. and Moore, J.S. *Atomic level study of the robustness of the Si(100)-2×1:H surface following exposure to ambient conditions* Appl. Phys. Lett. **78** 886 (2001)

Heyderman, L.J., Chapman, J.N. and Parkin, S.S.P. *Investigation of the magnetic structures in giant magnetoresistive multilayer films by electron microscopy* J. Appl. Phys. **76** 6613 (1994a)

Heyderman, L.J., Chapman, J.N. and Parkin, S.S.P. *TEM investigation of the magnetization processes in exchange coupled multilayer films* J. Magn. Magn. Mat. **138** 344 (1994b)

Higashi, G.S., Becker, R.S., Chabal, Y.J. and Becker, A.J. *Comparison of Si(111) surfaces prepared using aqueous solutions of NH_4F versus HF* Appl. Phys. Lett. **58** 1656 (1991)

Higashi, G.S., Chabal, Y.J., Trucks, G.W. and Raghavachari, K. *Ideal hydrogen termination of the Si(111) surface* Appl. Phys. Lett. **56** 656 (1990)

Hofmann, M., Regenfus, G., Scharpf, O. and Kennedy, P.J. *Measurement of the polarization of field emitted electrons from polycrystalline gadolinium* Phys. Lett. A **25** 270 (1967)

Hopster, H. and Oepen, H.P. *Magnetic microscopy of nanostructures* (Springer-Verlag, Berlin, 2005)

Hubert, A. and Schäfer, R. *Magnetic domains* (Springer, Berlin, 1998)

Jakob, P. and Chabal, Y.J. *Chemical etching of vicinal Si(111): Dependence of the surface structure and the hydrogen termination on the pH of the etching solutions* J. Chem. Phys. **95** 2897 (1991)

Jansen, R. *The spin-valve transistor: A review and outlook* J. Phys. D: Appl. Phys. **36** R289 (2003)

Jansen, R., Banerjee, T., Park, B.G. and Lodder, J.C. *Probing momentum distributions in magnetic tunnel junctions via hot-electron decay* Appl. Phys. Lett. **90** 192503 (2007)

Kaiser, W.J. and Bell, L.D. *Direct investigation of subsurface interface electronic structure by ballistic-electron-emission microscopy* Phys. Rev. Lett. **60** 1406 (1988)

Kanak, J., Stobiecki, T., Wisniowski, P., Gadyszewski, G., Maass, W. and Szymanski, B. *XRD study of the structure of NiFe/Au and NiFe/Cu superlattices* J. Magn. Magn. Mat. **239** 329 (2002)

Kinno, T., Tanaka, K. and Mizushima, K. *Ballistic electron emission spectroscopy on an Fe/Au/Fe multilayer* Phys. Rev. B **56** R4391 (1997)

Kittel, C. *Introduction to Solid State Physics* (John Wiley & sons, New York, 1976)

Kovsarian, A. and Shannon, J.M. *Amorphous chromium silicide formation in hydrogenated amorphous silicon* J. Electr. Mat. **27** 1268 (1998)

Lassailly, Y., Drouhin, H.J., van der Sluijs, A.J., Lampel, G. and Marliere, C. *Spin-dependent transmission of low-energy electrons through ultrathin magnetic layers* Phys. Rev. B **50** 13054 (1994)

LeLay, G., Quentel, G., Faurie, J.P. and Masson, A. *Epitaxy of noble metals and (111) surface superstructures of silicon and germanium. Part I: Study at room temperature* Thin Solid Films **35** 273 (1976)

Ludeke, R., Bauer, A. and Cartier, E. *Hot electron transport in SiO_2 probed with a scanning tunnel microscope* Appl. Phys. Lett. **66** 730 (1995)

Ludeke, R. and Prietsch, M. *Ballistic electron emission spectroscopy of noble metal-GaP(110) interfaces* J. Vac. Sci. Technol. A **9** 885 (1991)

McVitie, S. and Chapman, J.N. *Measurement of domain wall widths in permalloy using differential phase contrast imaging in stem* J. Magn. Magn. Mat. **83** 97 (1990)

Mead, C.A. *Operation of tunnel emission devices* J. Appl. Phys. **32** 646 (1961)

Mead, C.A. *Transport of hot electrons in thin gold films* Phys. Rev. Lett. **8** 56 (1962)

Milliken, A.M., Manion, S.J., Kaiser, W.J., Bell, L.D. and Hecht, M.H. *Probing hot-carrier transport and elastic scattering using ballistic electron emission microscopy* Phys. Rev. B **46** 12826 (1992)

Mizushima, K., Kinno, T., Tanaka, K. and Yamauchi, T. *Strong increase of the effective polarization of the tunnel current in $Fe/AlO_x/Al$ junctions with decreasing Fe layer thickness* Phys. Rev. B **58** 4660 (1998)

Monsma, D.J., Lodder, J.C., Popma, T.J.A. and Dieny, B. *Perpendicular hot electron spin-valve effect in a new magnetic field sensor: the spin-valve transistor* Phys. Rev. Lett. **74** 5260 (1995)

Moodera, J.S., Kinder, L.R., Wong, T.M. and Meservey, R. *Large magnetoresistance at room temperature in ferromagnetic thin film tunnel junctions* Phys. Rev. Lett. **74** 3273 (1995)

Narayanamurti, V. and Kozhevnikov, M. *BEEM imaging and spectroscopy of buried structures in semiconductors* Phys. Rep. **349** 447 (2001)

Niedermann, P., Quattropani, L., Solt, K., Maggio-Aprile, I. and Fischer, O. *Hot-carrier scattering in a metal: A ballistic-electron-emission microscopy investigation on PtSi* Phys. Rev. B **48** 8833 (1993)

Ohring, M. *Materials science of thin films* (Academic Press, San Diego, 2002)

Ozcan, S., Smoliner, J., Andrews, M., Strasser, G., Dienel, T., Franke, R. and Fritz, T. *Ballistic electron transport through titanylphthalocyanine films* Appl. Phys. Lett. **90** 092107 (2007)

Pappas, D.P., Kamper, K.P., Miller, B.P., Hopster, H., Fowler, D.E., Brundle, C.R., Luntz, A.C. and Shen, A.X. *Spin dependent electron attenuation by transmission through thin ferromagnetic films* Phys. Rev. Lett. **66** 504 (1991)

Parkin, S.S.P. *Origin of enhanced magnetoresistance of magnetic multilayers: Spin-dependent scattering from magnetic interface states* Phys. Rev. Lett. **71** 1641 (1993)

Parkin, S.S.P., Bhadra, R. and Roche, K.P. *Oscillatory magnetic exchange coupling through thin copper layers* Phys. Rev. Lett. **66** 2152 (1991)

Penn, D.R., Apell, S.P. and Girvin, S.M. *Theory of spin polarized secondary electrons in transition metals* Phys. Rev. Lett. **55** 518 (1985)

Portier, X. and Petford-Long, A.K. *The formation of 360° domain walls in magnetic tunnel junction elements* Appl. Phys. Lett. **76** 754 (2000)

Prietsch, M. *Ballistic electron emission microscopy (BEEM): studies of metal/semiconductor interfaces with nanometer resolution* Phys. Rep. **253** 163 (1995)

Prietsch, M. and Ludeke, R. *Ballistic electron emission microscopy and spectroscopy of GaP(110)/metal interfaces* Phys. Rev. Lett. **66** 2511 (1991)

Prinz, G.A. *Magnetoelectronics* Science **282** 1660 (1998)

Quinn, J.J. *Range of excited electron in metals* Phys. Rev. **126** 1453 (1962)

Rippard, W.H. and Buhrman, R.A. *Ballistic electron magnetic microscopy: Imaging magnetic domains with nanometer resolution* Appl. Phys. Lett. **75** 1001 (1999)

Rippard, W.H. and Buhrman, R.A. *Spin dependent hot electron transport in Co/Cu thin films* Phys. Rev. Lett. **84** 971 (2000)

Rippard, W.H., Perrella, A.C., Chalsani, P., Albert, F.J., Katine, J.A. and Buhrman, R.A. *Observation of magnetization reversal of thin film permalloy nanostructures using ballistic electron magnetic microscopy* Appl. Phys. Lett. **77** 1357 (2000)

Rohart, S. *Croissance et magnétisme de nanostructures organisées sur surfaces cristallines* Ph.D. thesis Université Paris VII (2005)

Schonhense, G. and Siegmann, H.C. *Transmission of electrons through ferromagnetic material and applications to detection of electron spin polarization* Ann. Physik **2** 465 (1993)

Schrefl, T., Fidler, J. and Zehetmayer, M. *Micromagnetic simulation of 360° domain walls in thin Co films* J. Appl. Phys. **87** 5517 (2000)

Simmons, J.G. *Generalized thermal J-V characteristic for the electric tunnel effect* J. Appl. Phys. **35** 2655 (1964)

Sirringhaus, H., Lee, E.Y. and von Kanel, H. *Atomic scale variations of the tunneling distribution in a scanning tunneling microscope observed by ballistic electron emission microscopy* Phys. Rev. Lett. **74** 3999 (1995)

Smoliner, J., Rakoczy, D. and Kast, M. *Hot electron spectroscopy and microscopy* Rep. Prog. Phys. **67** 1863 (2004)

Sze, S.M. *Physics of semiconductor devices* (Wiley-Interscience Publication, New York, 1981)

Thiaville, A., Caud, F., Vouille, C. and Miltat, J. *BEEM spectra of various Au-Si samples and their analysis* Eur. Phys. J. B **55** 29 (2007)

Thiaville, A., Miltat, J. and Garcia, J.M. *Magnetic Force Microscopy: Images of nanostructures and contrast modeling* 225, in *Magnetic microscopy of nanostructures* (Springer-Verlag, Berlin, 2005)

Tivarus, C., Pelz, J.P., Hudait, M.K. and Ringel, S.A. *Spatial resolution of ballistic electron emission on metal/quantum-well Schottky contacts* Appl. Phys. Lett. **87** 182105 (2005)

Trucks, G.W., Raghavachari, K., Higashi, G.S. and Chabal, Y.J. *Mechanism of HF etching of silicon surfaces: a theoretical understanding of hydrogen passivation* Phys. Rev. Lett. **65** 504 (1990)

Unguris, J., Celotta, R.J. and Pierce, D.T. *Observation of two different oscillation periods in the exchange coupling of Fe/Cr/Fe(100)* Phys. Rev. Lett. **67** 140 (1991)

van Dijken, S., Jiang, X. and Parkin, S.S.P. *Spin-dependent hot electron transport in $Ni_{81}Fe_{19}$ and $Co_{84}Fe_{16}$ films on GaAs(001)* Phys. Rev. B **66** 094417 (2002)

van Dijken, S., Jiang, X. and Parkin, S.S.P. *Comparison of magnetocurrent and transfer ratio in magnetic tunnel transistors with spin-valve bases containing Cu and Au spacer layers* Appl. Phys. Lett. **82** 775 (2003)

Ventrice, C.A., LaBella, V.P., Ramaswamy, G., Yu, H.P. and Schowalter, L.J. *Measurement of hot-electron scattering processes at Au/Si(100) Schottky interfaces by temperature-dependent ballistic electron emission microscopy* Phys. Rev. B **53** 3952 (1996)

Viyannalage, L.T., Vasilic, R. and Dimitrov, N. *Epitaxial growth of Cu on Au(111) and Ag(111) by surface limited redox replacement-An electrochemical and STM study* J. Phys. Chem. C **111** 4036 (2007)

Vlutters, R., vant Erve, O.M.J., Kim, S.D., Jansen, R. and Lodder, J.C. *Interface, Volume, and Thermal Attenuation of Hot-Electron Spins in $Ni_{80}Fe_{20}$ and Co* Phys. Rev. Lett. **88** 027202 (2002)

Wade, C.P. and Chidsey, C.E.D. *Etch pit initiation by dissolved oxygen on terraces of H-Si(111)* Appl. Phys. Lett. **71** 1679 (1997)

Weilmeier, M.K., Rippard, W.H. and Buhrman, R.A. *Ballistic electron transport through Au(111)/Si(111) and Au(111)/Si(100) interfaces* Phys. Rev. B **59** R2521 (1999)

Weilmeier, M.K., Rippard, W.H. and Buhrman, R.A. *Ballistic-electron-emission microscopy of conduction-electron surface states* Phys. Rev. B **61** 7161 (2000)

Wolf, S.A., Awschalom, D.D., Buhrman, R.A., Daughton, J.M., von Molnar, S., Roukes, M.L., Chtchelkanova, A.Y. and Treger, D.M. *Spintronics: A spin-based electronics vision for the future* Phys. Rev. B **61** 7161 (2000)

Wulfhekel, W., Beckmann, I., Rosenfeld, G., Poelsema, B. and Comsa, G. *Growth and morphology of Ni films on Cu(111)* Surf. Sci. **395** 168 (1999)

Yeh, J.J., Hwang, J., Bertness, K., Friedman, D.J., Cao, R. and Lindau, I. *Growth of the room temperature Au/Si(111)-(7×7) interface* Phys. Rev. Lett. **70** 3768 (1993)

Zhukov, V.P., Chulkov, E.V. and Echenique, P.M. *Lifetimes of excited electrons in Fe and Ni: First-principles GW and the T-matrix theory* Phys. Rev. Lett. **93** 096401 (2004)

Zhukov, V.P., Chulkov, E.V. and Echenique, P.M. *Lifetimes and inelastic mean free path of low-energy excited electrons in Fe, Ni, Pt, and Au: Ab initio GW+T calculations* Phys. Rev. B **73** 125105 (2006)